Torque Characterization of Permanent Magnet and Synchronous Reluctance Machines

Chirag Desai

A Thesis

In the Department

of

Electrical and Computer Engineering

Presented in Partial Fulfillment of the Requirements

For the Degree of

Doctor of Philosophy (Electrical and Computer Engineering) at

Concordia University

Montreal, Quebec, Canada

January 2019

CONCORDIA UNIVERSITY

SCHOOL OF GRADUATE STUDIES

This is to certify that the thesis prepared

By: Chirag Desai

Entitled: Torque Characterization of Permanent Magnet and Synchronous Reluctance Machines

and submitted in partial fulfillment of the requirements for the degree of

Doctor Of Philosophy (Electrical and Computer Engineering)

complies with the regulations of the University and meets the accepted standards with respect to originality and quality.

Signed by the final examining committee:

_____ Chair
Dr. Adam Krzyzak

_____ External Examiner
Dr. David A. Lowther

_____ External to Program
Dr. Sivakumar Narayanswamy

_____ Examiner
Dr. Ahmed A. Kishk

_____ Examiner
Dr. Luiz A.C. Lopes

_____ Thesis Supervisor
Dr. Pragasen Pillay

Approved by _____
Dr. Mustafa K. Mehmet Ali, Graduate Program Director

March 11, 2019

_____
Dr. Amir Asif, Dean
Gina Cody School of Engineering & Computer Science

ABSTRACT

Torque Characterization of Permanent Magnet and Synchronous Reluctance Machines

Chirag Desai, Ph.D.

Concordia University, 2019

The characterization of an electric machine can be evaluated using different available machine design and analysis softwares prior to manufacturing. These machine design softwares are either Finite Element Analysis (FEA) based or analytical model based. Each design software formulates and solves the machine design problem differently. Therefore, there is always a discrepancy in the results obtained from each of these softwares. The expertise of the user also affects the outcome of the analysis. Moreover, the desired performance of a machine is highly influenced by the manufacturing and assembly process of its various components. Hence, it is extremely important to characterize the design and performance of a special machine in different machine design softwares before and after fabrication. To validate the design methodologies, the accuracy of FEA softwares, machine models, as well as the manufacturing and assembly process, a comparative analysis should be performed between the results obtained from the software and experimental characterizations.

In this thesis, the characterization of a variable-flux permanent magnet machine, synchronous reluctance machines (SynRMs), and a novel interior permanent magnet synchronous machine (PMSM) with improved torque utilization, is presented. Three different machine design softwares, namely MotorSolve, MagNet, and MagneForce are used to characterize the machines.

This thesis initially presents the characterization of a 7.5 hp variable-flux permanent magnet machine. The back emf, magnet flux linkage, torque-angle, and core loss characterization is carried out for this machine. An error band is introduced for the experimental torque-angle curves. This error band contains the tolerance and resolution of the torque transducer and conditioner. Additionally, an analytical model is implemented to estimate the core losses in the prototyped variable-flux PM machine. The results obtained from software and experimental characterizations show an acceptable agreement. A comprehensive manufacturing and assembly process of the SynRMs for rapid prototyping is also presented in this thesis. The application of nonconventional photochemical machining

process to produce the SynRM laminations is described. In addition, various stages of manufacturing, stator and rotor assembly techniques, rotor balancing procedure as well as specialized components used at various stages of the process are also presented. To validate the accuracy of the design and fabrication, the characterization of three SynRMs is then performed. This consists of static torque-angle characterization, inductance characterization, and dynamic characterization. An error band is also included for the experimental torque-angle curves. A regenerative dynamometer test system is developed to perform various static and dynamic characterizations. This test setup is equipped with a real-time supervisory controller as well as measurement and monitoring instruments.

Finally, a novel interior PMSM topology with improved torque utilization to reduce magnet volume is characterized. The no-load back emf and static torque-angle are simulated and measured. A search coil based advance instrumentation system to monitor the machine's parameters is discussed. The design, manufacturing, and implementation of the search coils to measure flux density in the stator of the novel interior PMSM are also discussed.

For every characterization, a comparative analysis is performed to validate the design methodologies, accuracy of FEA softwares, machine models, manufacturing, and assembly process.

ACKNOWLEDGEMENTS

I would like to express my most sincere gratitude to my supervisor, Prof. Pragasen Pillay, for his patience, invaluable guidance, advice, and friendship throughout the Ph.D. program. Also, the author deeply appreciates the financial support from his supervisor.

This research work is done as part of Natural Sciences and Engineering Research Council of Canada (NSERC)/Hydro-Québec Senior Industrial Research Chair entitled "Design and Performance of Special Electrical Machines" held by Prof. P. Pillay at Concordia University. It is also done as part of the InnovÉÉ/NSERC Collaborative Research and Development project entitled "Emulation and Design of Electric and Hybrid Electric Vehicle Motor Drive Systems". This project is also supported by OPAL-RT Technologies, Hydro-Québec, and Mentor Infolytica, a Siemens Business. The authors acknowledge the support of the Natural Sciences and Engineering Research Council of Canada and Concordia University.

Sincere vote of appreciation to Rajendra and Sara for their help with the experimental measurements. Special thanks to Amitkumar for his advice in replying to the reviewers' comments and thesis writing. I would also like thank Mr. Hetal Mehta of Happy Engineering for his friendship and valuable consultation in machine fabrication. I am also thankful to Kang Chang and John Wanjiku for their technical support related to MotorSolve and MagNet.

I would like to thank other distinguished professors and colleagues in the Power Electronics and Energy Research (PEER) group. Appreciation goes to my PEER group family for the valuable discussions both technical and non- technical. I would also like to thank my friends and colleagues, specially, Nazanin, Dr. Mathews Boby, Gabriel, Gayathri, Zaid, Mahmood, Dr. Sudharshan, Jemimah, and Nazli for the discussion over the lunch, coffee, and fruit breaks.

I would like to dedicate this work to my mother, Mrs. Rekha Desai, father, Mr. Dililpkumar Desai, brother, Nirav Desai, sister in-law, Manali Natali Desai, and little bundle of joy Advait Desai. I would also like to thank Ajit, Simran, Ekroop, Bani, Tavinderjit Singh Sandhu, and Karamjit Kaur Sandhu for their constant motivation. Last, but not least, I would like to thank all my close friends for their steady support and encouragement.

In memory of

Jolly Sandhu Desai

TABLE OF CONTENTS

LIST OF FIGURES

LIST OF TABLES

LIST OF ABBREVIATIONS

AC	Alternating current
ALA	Axially laminated anisotropic
AlNiCo	Aluminum nickel cobalt
AWG	American wire gauge
CRGO	Cold-rolled grain-oriented
CRNGO	Cold-rolled nongrain-oriented
DC	Direct current
DE	Drive end
EMF	Electromotive force
EV	Electric vehicle
FEA	Finite element analysis
FFT	Fast Fourier transform
GO	Grain oriented
HEV	Hybrid electric vehicle
hp	Horse power
I.D	Inner diameter
IEC	International electrotechnical commission
IM	Induction motor
IPMSM	Interior permanent magnet synchronous machine
kW	Kilo watt
MTPA	Maximum torque per ampere
NDE	Nondrive end
NEMA	National electrical manufacturers association
NO	Nonoriented

O.D	Outer diameter
PCM	Photochemical machining
PEEK	Polyether ether ketone
PF	Power factor
PM	Permanent magnet
PMSM	Permanent magnet synchronous machine
PWM	Pulse width modulation
SmCo	Samarium–cobalt
SynRM	Synchronous reluctance machine
SPWM	Sinusoidal pulse width modulation
SWG	Standard wire gauge
TLA	Transversally laminated anisotropic
UV	Ultraviolet
VA	Volt ampere
VFD	Variable frequency drive
VFPM	Variable-flux permanent magnet
VSI	Voltage source inverter

LIST OF SYMBOLS

B	Magnetic flux density
B_r	Remnant magnet flux density of the magnet
B_{rad}	Radial component of the magnetic flux density
B_x, B_y	Orthogonal components of the flux density
B_θ	Tangential component of the magnetic flux density
f	Supply frequency
H	Magnetic field intensity of the permanent magnet at the operating point
I_L	Line current
i_d	*d*-axis current
i_q	*q*-axis current
$\widehat{I_s}$	Peak phase current
L_d	*d*-axis inductance
L_q	*q*-axis inductance
P	Number of poles
P_e	Eddy current loss
P_t	Specific total core loss
Q	Reactive power
R_s	Phase winding resistance
T_e	Electromagnetic torque
T_m	Permanent magnet torque
T_{rel}	Reluctance torque
T_L	Load torque
V	Phase voltage

v_d	*d*-axis voltage
v_q	*q*-axis voltage
W_h	Hysteresis energy loss
X	Phase reactance
$\lambda_a, \lambda_b, \lambda_c$	Phase A, B, and C flux linkage
λ_d	*d*-axis flux linkage
λ_m	Flux linkage due to the permanent magnet
λ_q	*q*-axis flux linkage
μ_0	Magnetic permeability of the free space
μ_r	Relative magnetic permeability
ω_r	Rotor speed (rad/s)
α	Rotor slot pitch angle
β	Stator slot pitch angle
θ_b	Barrier angle
θ_p	Pole arc angle
δ	Current angle
ζ	Saliency ratio
ρ	Mass density
σ	Electrical conductivity
ϕ	Magnetic flux
ω	Electrical speed (rad/s)

Chapter 1 Introduction

1.1 Characterization of Electric Machines

Permanent magnet synchronous machines (PMSMs) and induction machines (IMs) are extensively used in electric vehicles (EVs) and hybrid electric vehicles (HEVs); because of their specific advantages, viz., high torque density (PMSMs) and high performance (IMs) [1, 2]. However, the price of rare-earth magnets is fluctuating, and supply and resources are insufficient. In addition, PMSMs have limited flux weakening capabilities. These limitations pertaining to PMSMs have caused a shift towards a new generation of high performance machine technologies which either do not depend on rare-earth permanent magnets; variable-flux permanent-magnet (VFPM) or do not have permanent magnets; synchronous reluctance machine (SynRM). In addition, these special machines possess, high torque density, high power density, high efficiency, better flux-weakening capability, and are economically viable [3]. In conventional interior permanent magnet synchronous machines (IPMSMs), the magnet and reluctance torque components have their maximum values at different torque angles, so the total torque of the machine cannot completely utilize the reluctance torque and the magnet torque at any operating point. For the IPMSMs, intensive research is ongoing to reduce the quantity of rare-earth magnets. This is being achieved through better utilization of the magnet and reluctance torque components using various design optimization methods. These machines can provide high torque density and superior field weakening performance as they can utilize both the magnet and reluctance torque components.

The desired performance of a machine is greatly influenced by the manufacturing and assembly process of its various components. In addition, in traction applications, these machines are operated over a wide speed, and torque envelope by variable frequency drives (VFDs) and hence are exposed to several frequencies and flux densities. Operation of these machines under various conditions also causes a large variation in the parameters of the machine, specifically, the core losses. Therefore, during the design of these machines, it is essential to analyze the core losses over a wide frequency and flux density range. In order for a machine designer to estimate the core losses at the design stage, a core loss model that can accurately predict core losses at different operating points and conditions is required. In addition, in mission-critical transportation applications, an unanticipated fault or failure of the

machine could lead to very high maintenance or replacement price, or even total system failure. Therefore, for an electric machine, the measurement of its magnetic and electric quantities is essential. In the prototyping stage, measurement results are useful to verify the design calculations, material properties, and fabrication methods.

The design, characterization, and performance of a machine can be determined using different available machines design software prior to manufacturing. Some of these machine design softwares are finite element analysis (FEA) based and some are analytical model based. Each of these design softwares formulates and solve the machine design problem differently. Therefore, there is always a discrepancy in the results obtained from different softwares. The expertise of the user may also affect the outcome of the analysis.

It is therefore extremely important to characterize the design and performance of a special machine like variable-flux PMs, SynRMs, and IPMSMs in different machine design software before and after fabrication. To validate the design methodologies, accuracy of FEA software, machine models, manufacturing, and assembly process, a comparative analysis can then be performed between the results obtained from software and experimental characterization. Moreover, the machine can be fabricated with robust instrumentation for parameter monitoring and measurement. Continuous parameter monitoring can enhance machine performance and also help schedule periodic maintenance to circumvent machine failure.

An advanced test facility is required to allow characterization, parameter measurement, efficiency measurement, and validation of the design of prototyped electrical machines. Furthermore, machine parameters extracted from various static and dynamic simulations and measurements can be further used in the developed machine models, efficiency estimation, and drive emulation. Fig. 1-1 presents a general layout of an electric machine characterization.

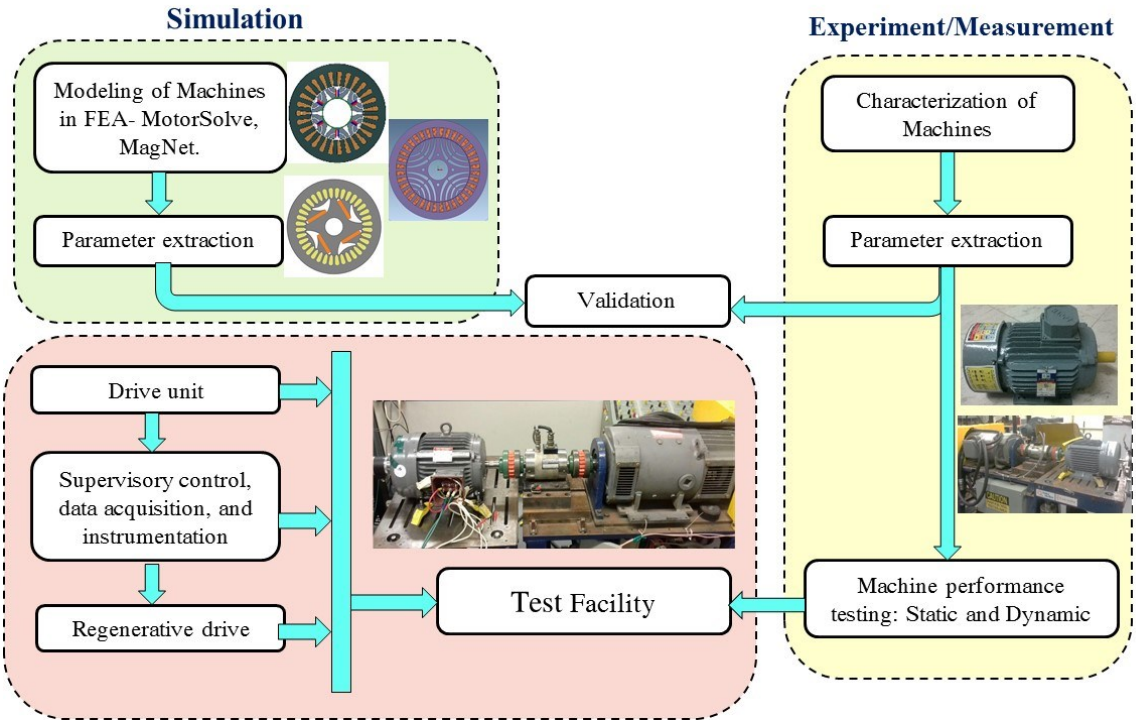

Fig. 1-1. General layout of an electric machine characterization process.

1.2 Objectives

This research work is part of an NSERC/CRD project entitled "Emulation and design of electric and hybrid electric vehicle motor drive systems." The main objective of this work is to characterize a variable-flux PM machine, SynRMs, and a novel interior PMSM with improved torque utilization, to validate the design methodologies, accuracy of FEA software, machine models, manufacturing, and assembly process.

Other objectives of this work include;

- Implementation of an analytical model to predict the core losses in the prototype a variable-flux PM machine.
- Development of an experimental setup with the machine in order to perform various static and dynamic characterizations.
- Design and implementation of a search coil based advanced instrumentation system to monitor the machine's parameters.

1.3 Contributions

The research contributions of the work can be summarized as:

Chapter 2

- The no-load back electromotive force (emf), magnet flux linkage, torque-angle curves, and no-load core losses are characterized for a 7.5 hp variable-flux PM machine for three different magnetization levels. Simulations are performed in three different machine design softwares. The no-load core losses are also obtained using an analytical finite section method. A comparative analysis of the results obtained from the FEA software and experimental characterizations are achieved to support the accuracy of the design, modeling, FEA software, and testing.

  An accurate back emf estimation can provide a more precise value of the magnet flux linkage, which is necessary for the magnetization state control and braking of the variable-flux PM machine. The static torque-angle characterization gives the magnitude of peak torque and the current angles for maximum torque per ampere control. Moreover, it also provides information about the safe operating regions of the machine where the AlNiCo magnets do not demagnetize or magnetize by the stator currents. This information is very helpful for drives engineers during the development of control algorithms. Core loss estimation at various operating conditions gives a better efficiency estimate. Moreover, the analytical model serves as an additional tool along with the FEA for core loss estimation, through which the machine designers can enhance their design for better performance.

Chapter 3

- A detailed manufacturing and assembly process of SynRMs is presented. One stator is manufactured, and two types transversally laminated anisotropic (TLA) as well as one TLA segmented SynRM rotors are fabricated. The application of nonconventional photo chemical machining (PCM) to produce machine laminations is presented. Different stages of manufacturing, stator and rotor assembly techniques, rotor balancing procedure, as well as specialized components used at various stages of the process are described. This work presents a simple and economical way of machine fabrication during the initial development phase, which indeed enables a new alternative way of rapid prototyping with possible applicability for mass production.

Chapter 4

- Characterization of the three SynRMs discussed in Chapter 3 is presented in this chapter. The static torque-angle, inductance, and dynamic characterization of the prototyped SynRMs are presented. The SynRM designs are also analyzed in the design software. A special regenerative dynamometer test setup is developed in order to perform dynamics tests. For the prototyped SynRMs, the torque-speed envelope, power factor, efficiency, and steady state torque are measured by using the test setup. The static torque-angle characterization gives the magnitude of peak torque and current angles for maximum torque per ampere control. The inductance characterization provides inductance variations under different loading conditions. This information benefits a drive designer to decide on the drive controller's parameters and perform an accurate dynamic characterization. The developed test setup is equipped with a real-time supervisory controller as well as measurement and monitoring apparatus. This facilitates static and dynamic testing of various kinds of machines, real-time parameter measurements, and control.

Chapter 5

- In this chapter, the back emf and static torque-angle characterization of a novel interior PMSM is carried out. The interior PMSM is designed to align the reluctance and magnet torques. This improves the total torque of the machine and also reduces the magnet volume. Moreover, this machine has a larger torque in one direction and smaller in another. Thus, the variation of machine parameters is not the same for positive and negative currents. Since this machine is a new topology, it is worthwhile to characterize the machine performance for its applications. Moreover, a search coil based advance instrumentation system to measure the flux density in the different part of the machine and monitor machine's parameters is discussed.

This research work has led to the following technical publications:

Journal papers:

[1] **C. Desai** and P. Pillay, "Back emf, Torque-angle, and Core Loss Characterization of a Variable-flux Permanent-Magnet Machine," *IEEE Transactions on Transportation Electrification*. (Under review)

[2] **C. Desai,** H. Mehta, and P. Pillay, "Fabrication and Assembly Method for Synchronous Reluctance Machines," *IEEE Transactions on Industry Applications*, vol. 54, no. 5, pp. 4227-4235, Sept./Oct. 2018.

[3] P. Pillay, M. Al-Badri, P. Angers, and **C. Desai**, "A New Stray-Load Loss Formula for Small and Medium-Sized Induction Motors," *IEEE Transactions on Energy Conversion*, vol. 31, no. 3, pp. 1221-1227, Sept. 2016.

Conference papers:

[1] **C. Desai,** H. Mehta, and P. Pillay, "A Novel Fabrication and Assembly Method for Synchronous Reluctance Machines," in Proc. *IEEE Energy Conversion Congress & Expo.*, Cincinnati, OH, Oct.2017.

[2] **C. Desai** and P. Pillay, "Torque-Angle Characterization of a Synchronous Reluctance Machine," in Proc. *IEEE International Conference on Power Electronics, Drives, and Energy Systems*, Trivandrum, Kerala, India, Dec. 2016.

[3] **C. Desai** and P. Pillay, "Torque and Core Loss Characterization of a Variable-Flux Permanent-Magnet Machine," in Proc. *IEEE Energy Conversion Congress & Expo.*, Milwaukee, WI, Sept. 2016.

1.4 Thesis outline

This thesis is organized as follows:

Chapter 2 presents the back emf, magnet flux linkage, torque-angle, and core loss characterization of a variable-flux permanent magnet machine. No-load back emf, torque-angle curves, and no-load core losses are measured and simulated for a 7.5 hp variable-flux machine for three different magnetization levels. A comparative analysis is performed between the results obtained from software and experimental characterizations.

In **Chapter 3** a comprehensive manufacturing and assembly process of synchronous reluctance machines (SynRMs) is presented. The application of nonconventional photo chemical machining (PCM) to produce machine laminations is presented. Different stages of manufacturing, stator and rotor assembly techniques, rotor balancing procedure, as well as specialized components used at various stages of the process are described.

Chapter 4 describes the characterization of three SynRM designs discussed in Chapter 3. The static torque-angle, inductance, and various dynamic characterizations of the prototyped SynRMs are presented. A comparative analysis is performed for the results obtained from software and experimental characterizations.

In **Chapter 5**, the no-load back emf and static torque-angle characterization of a novel interior PMSM that can improve the utilization of the machine's torque components are presented. Moreover, a method based on the search coil sensor to measure the flux density in the different part of the stator is discussed.

Chapter 6 concludes the work completed and provides recommendations for future work.

Chapter 2 Back emf, Torque-angle, and Core Loss Characterization of a Variable-flux Permanent-Magnet Machine

In this chapter, the back emf, magnet flux linkage, torque-angle, and core loss characterization of a 7.5 hp variable-flux permanent-magnet machine is presented. The properties of AlNiCo 9 magnet and the process of magnetization and demagnetization are also described. Moreover, for validation purposes, the measured back emf, magnet flux linkage, and torque-angle curves are compared with the simulation results obtained from three different machine design softwares, namely MotorSolve, MagNet, and MagneForce. The characterizations are carried for three different magnetization levels. The static torque-angle curves are obtained by varying the current advance angle and the rotor position. The core losses are also obtained using an analytical method, which is first utilized to calculate the core losses in M19G29 laminations and then implemented to estimate the core losses of the prototyped variable-flux machine.

2.1 Introduction to Variable-flux Machines

Rare-earth permanent magnet synchronous motors (PMSMs) are being used increasingly in electric and hybrid electric vehicles as well as in a wide range of industrial drives and servo applications. This is mainly due to their superior power density, high torque-to-inertia ratio, and efficiency. However, higher losses and lower efficiency during high speed operation, limited flux weakening capability, fluctuating price and limited resources of rare-earth permanent magnets (PMs) have forced transportation and other rotating machine industries to develop alternatives to rare-earth machine technologies.

Ferrite magnets are inexpensive and widely used in low cost appliances. Due to low remnant flux density, it is difficult to manufacture a ferrite PMSM that matches the performance of rare-earth PMSMs [4, 5]. On the other hand, AlNiCo magnets can operate at high temperatures and at flux densities close to rare-earth PMs, they are rarely used in present machines, as the magnets can be easily demagnetized by the stator field. If PMSMs with AlNiCo are designed with controllable demagnetization, they can provide efficiencies and torque densities as good as rare-earth PMSMs [6]. Moreover, the low coercivity of AlNiCo

can be used to increase machine performance at high speeds, as the magnet magnetization level can be controlled by *d*-axis armature current pulses. In [7], a theory of the variable-flux memory machine was proposed to attain high efficiency in the extended speed region. Several variations of variable flux machines have been investigated in [8], [9], and [10]. A novel design of a tangentially magnetized variable-flux machine with AlNiCo magnets was proposed in [11] to achieve high torque density and efficiency without exposing the magnets to demagnetization by the armature field. In [12], a design optimization method and an analytical criterion to select magnet dimensions were presented to reduce torque ripple of a spoke-type variable flux machine proposed in [11] using the same stator and slot per pole per phase combination. Moreover, [13] presents the operating envelopes of the variable-flux machine that was presented in [11].

Advancement in power electronics and machine design have allowed variable-flux machines to be used in various traction and industrial drive applications. These motors are controlled from a power electronic converter. The torque to ampere ratio and the torque angle are very important parameters in evaluating the machine performance. It is quite challenging to obtain the optimum magnitude of current vectors for maximum torque at different operating scenarios and motor parameter variations, when the motor is under operation. However, it is possible to obtain the offline trajectories of reference currents to implement the maximum torque per ampere condition [14]. An appropriate torque-angle characterization can reduce the size of the converter and enhance the performance of the machine.

One essential component in the design and optimization of rotating electrical machines and drives is the core loss, as it constitutes a large portion of the total losses ranging from 15-25% for four-pole medium horse-power (10hp-200hp) machines operating with sinusoidal supplies [15]. Due to distinct geometries and operation under time varying non-sinusoidal magnetic fields, the core losses are higher for PMSMs. Moreover, high speed operation of PMSMs requires continuous flux weakening current, which causes a significant increase in the machine copper and core losses. Also, at high frequencies, the eddy current loss in the laminations increases rapidly, as it is proportional to the square of the rate of change of flux. The core losses tend to increase further with variable frequency drives (VFDs) due to the harmonics introduced.

In PMSMs with rare-earth magnets, the magnets should maintain their fully magnetized state during all operating conditions. During high speed operation, the core loss of the machine increases significantly, which reduces the efficiency of the machine. However, in variable-flux machines with AlNiCo magnets, the magnet magnetization level can be adjusted at high speeds using the demagnetizing *d*-axis current pulses [11]. This can reduce the eddy current loss, and hence the total core loss of the machine. Thus, it is extremely important to analyze the core losses of variable-flux machines at different magnetization levels. Therefore, variable-flux machines with low coercivity magnets can provide higher efficiency in the field weakening region than conventional PMSMs. In order to regain the high torque capability at low speeds, the magnets can be re-magnetized by applying magnetizing *d*-axis current pulses.

2.2 Design and Specification of a Variable flux Permanent Magnet Machine

A novel design of a tangentially magnetized variable-flux machine with AlNiCo magnets was proposed in [11] to achieve high torque density and efficiency without exposing the magnets to demagnetization by the armature field. In the proposed design, AlNiCo grade 9 magnets were used due to their high remnant flux density and low coercive field, as well as the ability to withstand temperatures of up to 500˚C. An analytical method was first used to obtain the initial machine design parameters. Then several modifications were applied to the stator and rotor designs through FEA in order to improve the machine efficiency and torque density.

The number of stator slots and winding pattern have a direct effect on the magnetization current and machine performance. In [11], the 6-pole machine with fully-pitched distributed windings is first simulated with 18 slots, 36 slots, and 54 slots, respectively. The simulation results are presented in Table 2-I. It is apparent from Table 2-I that a low number of slots per pole design can significantly minimize the magnetization current. However, the 18-slot machine has higher torque pulsations as compared to the 54-slot and 36-slot designs. Whereas, the 36-slot design requires 9.4 A additional magnetization current than the 18-slot design. Hence, the 6-pole machine is simulated with fractional windings with 9-slots and 27-slots. Although the 9-slot design has low magnetization current, it has high torque ripple. In addition, because of slotting effects, the variation of magnet flux density is more prominent in machines with lower slots per pole ratios. For the 9-slot fractional winding design, at full load, this variation is sufficient to cause irreversible magnet demagnetization, which in turn reduces the

machine output torque. When the magnet is aligned with a tooth, the effective number of stator teeth carrying the magnet flux is reduced, and hence the stator teeth saturate. This moves the magnet operating point below the demagnetization curve knee point, where the magnetization loss is irreversible. Consequently, the magnet operates at a lower flux density level when it moves to the next slot. On the other hand, the 27-slot design has the lowest torque ripple and the highest efficiency among all the simulated designs. In addition, the 27-slot design has a lower magnetization current than the 36-slot design. Therefore, the 6-pole and 27-slot fractional winding design is selected for analysis and prototyping. In order to improve the quality of the back emf, a variable air gap length is used to reduce back emf harmonics and to produce a more sinusoidal air gap flux density distribution. Flux barriers are also inserted in the rotor lamination to increase the saliency ratio and restrict the armature flux. The purpose of the flux barriers is to utilize both the reluctance and magnet torque components. The specifications of the designed machine are shown in Table 2-II.

Table 2-I FEA Simulation results for machines with different slot and winding configuration [6]

	Integral windings			Fractional windings	
	54 slots	36 slots	18 slots	9 slots	27 slots
Number of slots/pole	9	6	3	1.5	4.5
Torque ripple %	18.6	27	117	110.1	12.5
Efficiency %	94.7	94.7	94.6	93.8	94.8
Full magnetization current (A)	33.5	33.0	23.6	20.6	30.2

Table 2-II Machine specifications

Number of poles	6		Magnet material	AlNiCo 9
Number of slots	27		Steel material	M19G29
Stator outer diameter (mm)	200		DC bus voltage (V)	600
Axial length (mm)	120		Rated current (A rms)	10
Air gap length (mm)	0.4 - 0.75		Output torque (Nm)	36.8
Saliency ratio (L_d/L_q)	1.6		Base speed (rpm)	1200

In order to evaluate the machine performance, a prototype is manufactured with AlNiCo 9 magnets according to the specification listed in Table 5-II. Fig. 2-1(a) shows the rotor geometry of the tangentially magnetized variable-flux machine and the prototyped rotor 12 is shown in Fig. 2-1(b). The winding coil has 23 turns and is comprised of two strands of 21 AWG and two strands of 22 AWG copper wires respectively. The machine is fabricated with class H insulation.

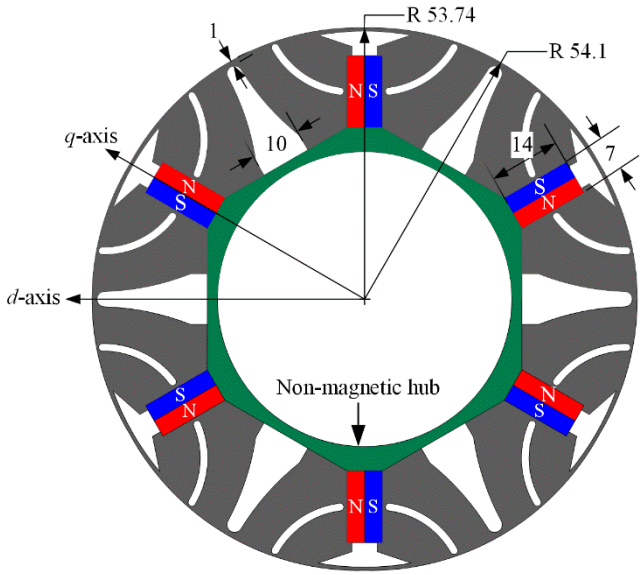

(a)

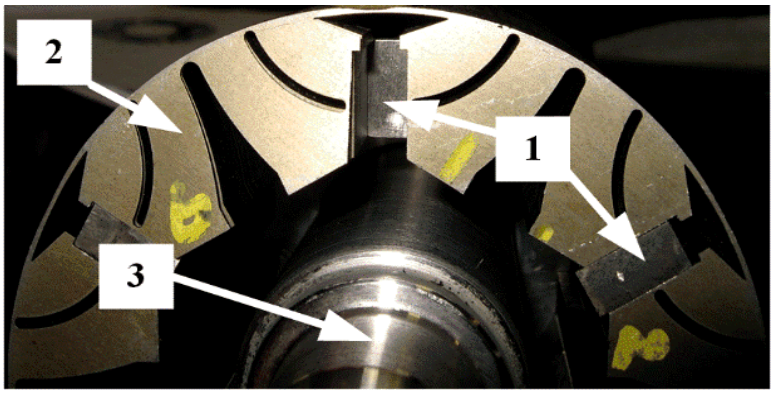

(b)

Fig. 2-1. (a) Rotor geometry. (b) Prototyped rotor. (1) AlNiCo 9 magnets. (2) Rotor lamination. (3) Motor shaft.

2.3 Back emf, magnet flux linkage and Torque –angle characterization

In this section, the back emf, magnet flux linkage, and torque-angle characterization is presented for the prototyped variable-flux permanent-magnet machine for three different magnetization levels. Moreover, the magnetic properties of the AlNiCo 9 magnet and a process of AlNiCo magnet magnetization and demagnetization are presented.

2.3.1 Properties of AlNiCo 9 Magnet

The demagnetization B–H curves of an AlNiCo 9 magnet for three different magnetization levels are presented in Fig. 2-2. At no-load, the prototyped variable-flux machine is designed to operate at Point A, at the intersection of the air gap line and the main demagnetization curve. In order to maintain the full magnet flux linkage during different loading conditions, the magnet operating point should be within the linear region of the demagnetization curve between point A and point B. During the operation of the motor above the base speed (constant power mode), the magnet flux is decreased by applying a demagnetizing magnetic field of Ha_2.This process moves the magnet operating point below the demagnetization curve knee to point C, where the demagnetization is irreversible. When this demagnetizing field is released, the magnet recoils along the 75% demagnetization curve and the operating point changes to point D. Similarly, during high speed operations, the magnet flux is further reduced by applying a demagnetizing magnetic field of Ha_3, which moves the magnet operating point to point E. When this demagnetizing field is released, the magnet recoils along the 50% demagnetization curve and the operating point changes to point F. In order to re-magnetize the magnets during low speed high torque operations (constant torque mode) below base speed, a magnetizing field is applied in such a way that the magnet operating point shifts in the first or third quadrant until the saturation region of the hysteresis loop is reached. When this field is released, the magnet would be fully magnetized, and it would recoil back to its initial operating point at the airgap line.

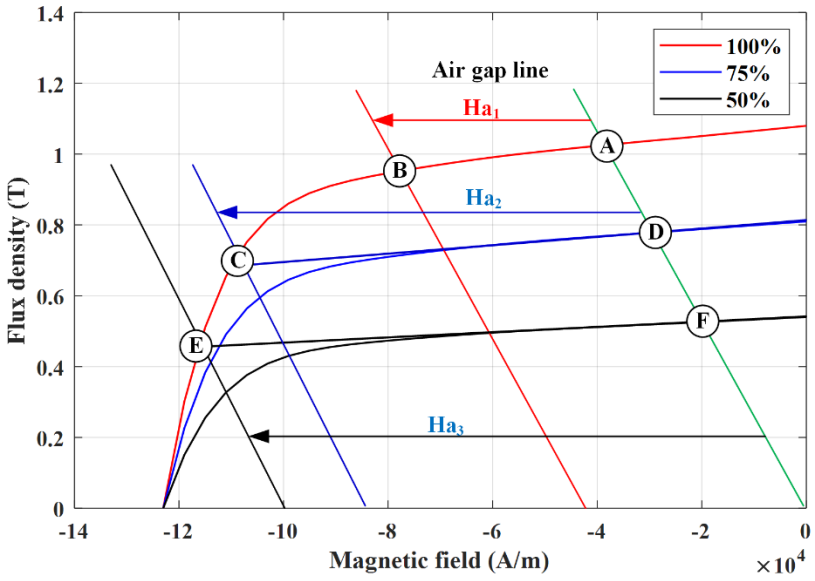

Fig. 2-2. Demagnetization characteristics of AlNiCo 9.

Complete hysteresis curves of the AlNiCo 9 magnet are shown in Fig. 2-3. The hysteresis curves are obtained from the FEA software which includes a major loop, two of the minor loops, and the initial magnetization curve. In FEA software, the flux density (B) of the AlNiCo magnet is obtained from the average reading of several flux density probes placed on the magnet. Similarly, the magnetic field intensity (H) is obtained. At the beginning of the process, the AlNiCo magnets are completely demagnetized. Positive current pulses of increasing magnitudes are then applied in steps of 5 A until saturation is reached. In order to obtain the initial magnetization curve, at each current pulse, the generated H and the resultant B are recorded. The flux density of the magnet is recorded after the last current pulse, which gives the recoiled remanent flux density (B_r). In order to obtain the major hysteresis loop of the AlNiCo 9 magnet, negative pulses of increasing magnitudes are then applied until saturation is reached. At each pulse, the flux density and the field intensity in the magnets are recorded. This process gives the major B-H curve in the second and third quadrants. The magnet flux density is also recorded after the last current pulse, which gives the negative recoiled remanent flux density ($-B_r$). Once again, the magnetization current pulses of increasing magnitudes are applied until saturation is reached and at each pulse, the flux density and the field intensity in the magnets are recorded. This process gives the major B-H curve in the fourth and first quadrants. In a similar manner, the selected inner loops are obtained with the caution not to reach saturation.

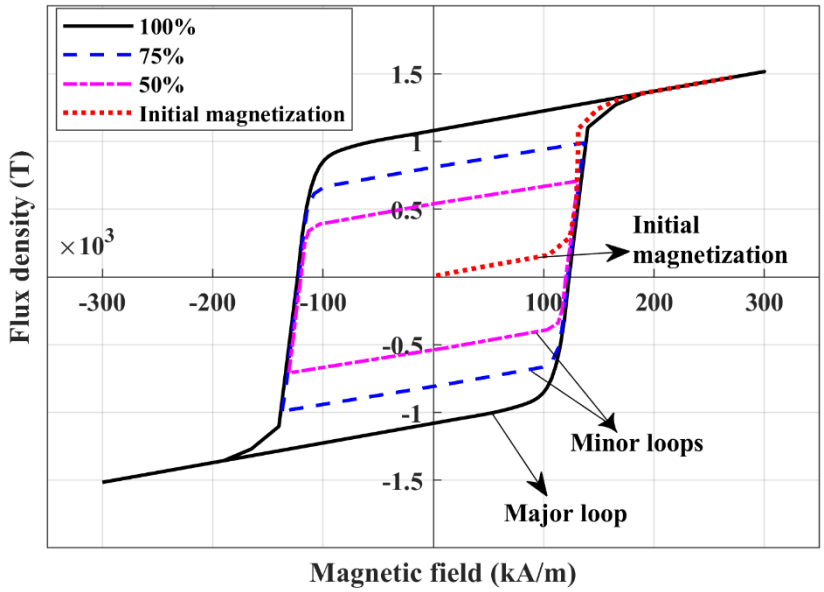

Fig. 2-3. Hysteresis curves of AlNiCo 9.

2.3.2 Back emf characterization

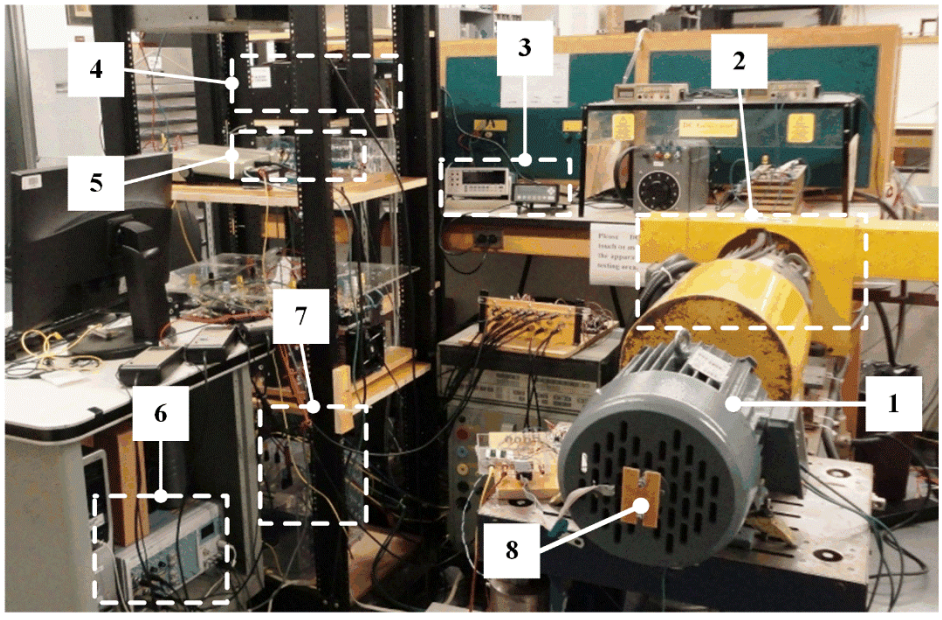

Fig. 2-4. Variable-flux machine test setup. (1) Variable-flux permanent-magnet machine. (2) Dynamometer. (3) Measuring instruments. (4) Real-time simulator. (5) Sensors. (6) Data acquisition. (7) Inverter. (8) Encoder.

In the prototyped variable-flux machine, the AlNiCo magnets are inserted in a demagnetized state. Magnetization and demagnetization tests are carried out on the test setup using the armature winding. The back emf is then measured in order to assess the magnet magnetization state. Fig. 2-4 shows the machine test setup. The test bench includes a direct

current (dc) dynamometer, a torque transducer, a voltage source inverter (VSI), a real-time controller, a position encoder, and a data acquisition unit. The variable-flux machine is coupled with a dc dynamometer through a torque transducer. To magnetize the magnets, the *d*-axis of the rotor is first aligned with the phase A-axis of the armature winding on the test setup. Using a VSI, magnets are then magnetized by applying the magnetizing *d*-axis current pulses of increasing magnitude up to 40 A. Each current pulse is applied for a duration of 10 *msec*. The back emf is measured after each pulse during the magnetization processes. Beyond 40 A of *d*-axis current pulses, there is no increment in the torque and the back emf observed, as the magnets are saturated and the magnet flux linkage reached approximately 100% at 0.515 V.sec.

Fig. 2-5 shows the magnitude of applied *d*-axis current and the resulting magnet flux linkage. To reduce the magnet flux linkage, demagnetization current pulses are applied, and back emf is measured after each demagnetizing current pulse. Fig. 2-6 shows the demagnetization current magnitude and the resulting magnet flux linkage.

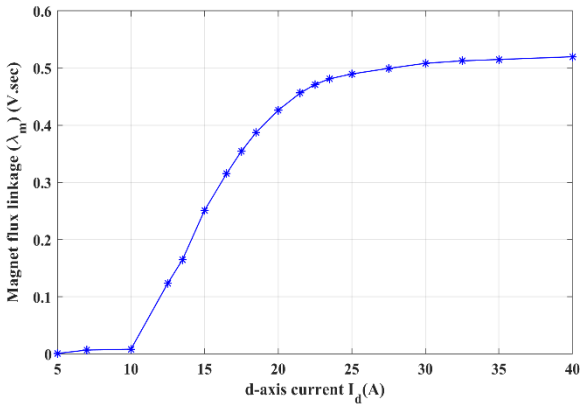

Fig. 2-5. Magnetization current magnitude vs. magnet flux linkage.

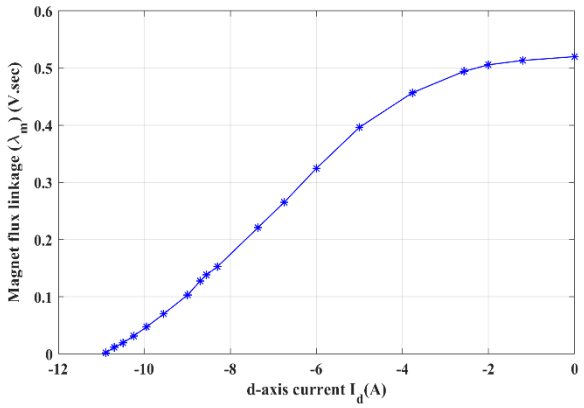

Fig. 2-6. Demagnetization current magnitude vs. magnet flux linkage.

In order to estimate the magnitude of the magnet flux linkage (λ_m), first, the prototyped variable-flux machine is run as a generator at the design speed of 1200 rpm using a dc dynamometer and the back emf is measured for 100% magnetization level. The magnet flux is then reduced to 75% and 50%, and the corresponding back emf is recorded. The back emf waveforms are also obtained from the design software for three different magnetization levels. Fig. 2-7 (a), (b), and (c) represent the back emf waveforms obtained from the design software and the measurements for 100%, 75%, and 50% magnetization level, respectively.

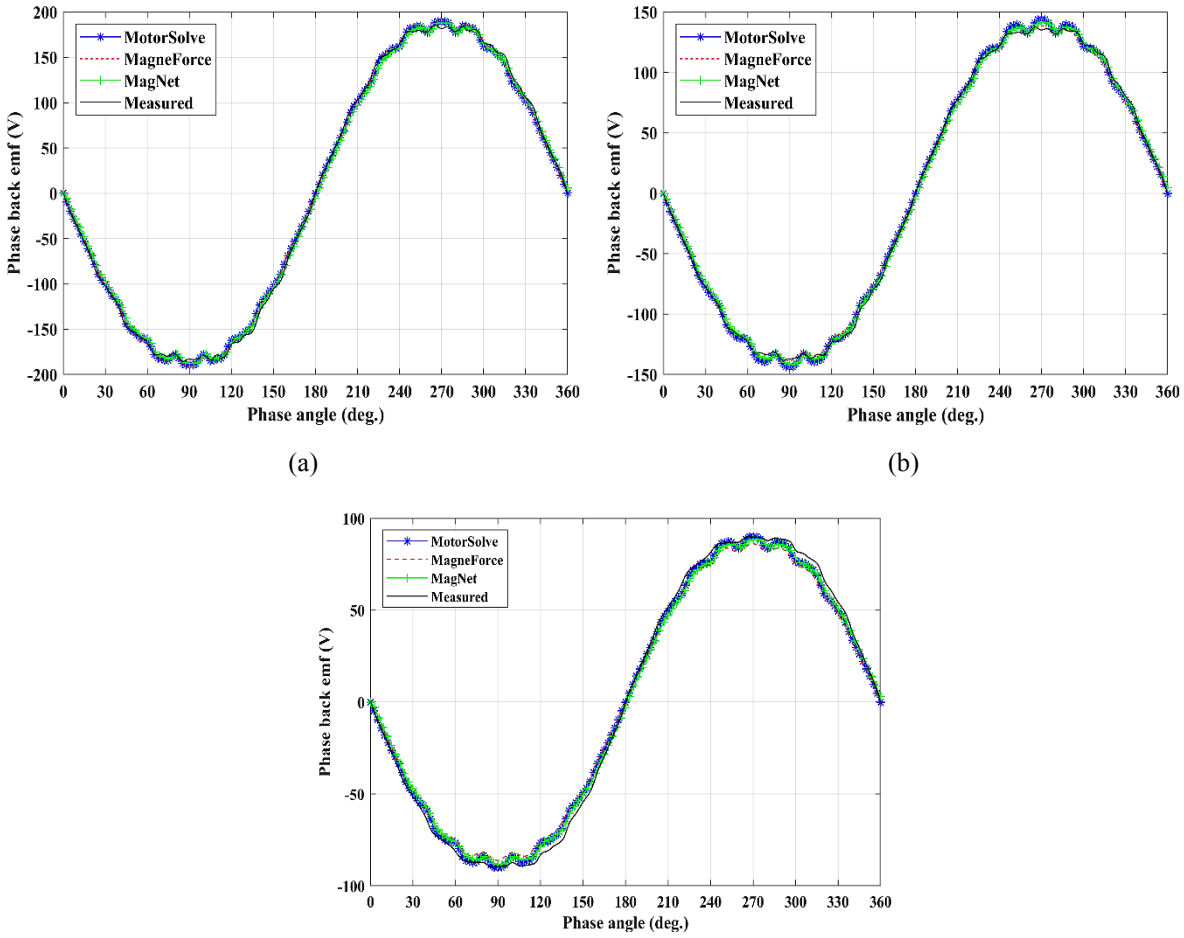

Fig. 2-7. Back emf comparison at 1200 rpm. (a) @100% magnetization. (b) @75% magnetization. (c) @50% magnetization.

The peak value of the fundamental component of the back emf waveform is required to estimate the magnet flux linkage. However, the back emf waveforms of Fig. 2-7 (a), (b), and (c) contain harmonics. Hence, the peak value of the fundamental component of the back emf is obtained using the fast Fourier transform (FFT). Fig. 2-8(a) presents the FFT plot of the back emf waveforms and the peak value of the fundamental components for 100% magnetization. The FFT spectra of the harmonics alone are presented in Fig. 2-8(b). It is observed from Fig. 2-8(b) that there is a mismatch between the 3rd harmonic obtained from the softwares and measurement. However, the 3rd harmonic is not present in the line voltage when the machine is under its normal operation. Hence, this mismatch is of a low importance. The peak magnitude obtained from the FFT is similar to the peak value obtained from the rms value of the back emf

waveform. To obtain the value of the magnet flux linkage, the peak value of the fundamental component is divided by the electrical speed (377 rad/sec) of the machine. Table 2-III compares the peak value of the fundamental component and the magnet flux linkage obtained from MotorSolve, MagneForce, MagNet, and the measurements for 100%, 75%, and 50% magnetization level, respectively.

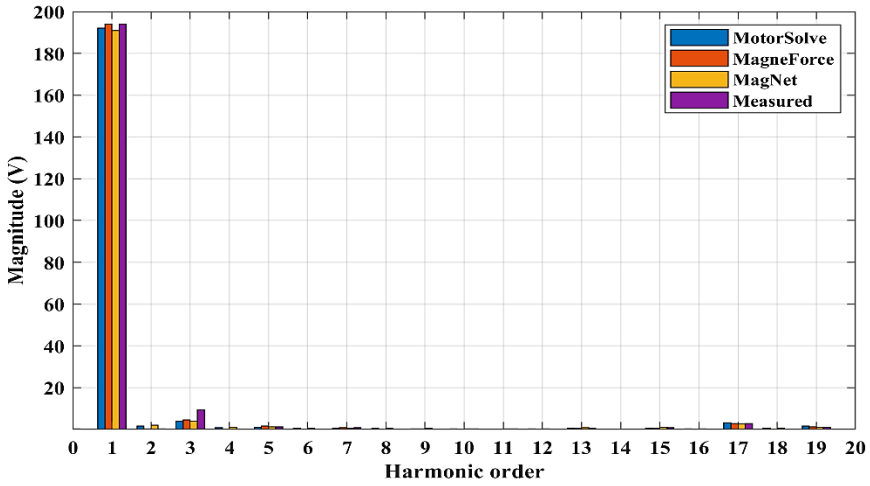

(a)

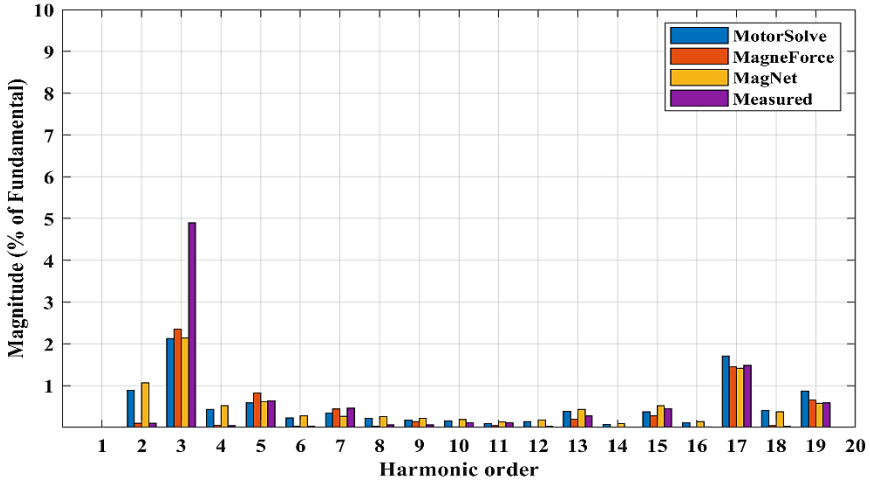

(b)

Fig. 2-8. FFT plots of back emf waveforms at @100% magnetization. (a) FFT plot of the back emf waveforms representing the fundamental components. (b) FFT plot of the back emf waveforms representing the harmonic components.

Table 2-III Comparisons of the fundamental peak and magnet flux linkage

		MotorSolve		MagneForce		MagNet		Measured	
		Fundamental peak (V)	**Flux linkage (V.s)**	**Fundamental peak (V)**	**Flux linkage (V.s)**	**Fundamental peak (V)**	**Flux linkage (V.s)**	**Fundamental peak (V)**	**Flux linkage (V.s)**
Magnetization	100%	192	0.510	194	0.515	191	0.506	194	0.515
	75%	145	0.385	141	0.375	143	0.381	144	0.384
	50%	89.9	0.238	86.2	0.229	88.4	0.235	89.9	0.239

2.3.3 Torque-angle characterization

The steady state torque of variable-flux machine in the *dq* domain can be obtained by

$$T_e = \frac{3}{2}\frac{P}{2}\left[\lambda_d i_q - \lambda_q i_d\right] = \frac{3}{2}\frac{P}{2}\left[\lambda_m i_q + \left(L_d - L_q\right) i_d i_q\right] \tag{2-1}$$

$$\begin{aligned} T_e &= \frac{3}{2}\frac{P}{2}\left[\lambda_m I_s \sin(\delta) + \left(L_d - L_q\right) I_s^2 \sin(2\delta)\right] \\ &= T_m + T_{rel} \end{aligned} \tag{2-2}$$

where λ_d is the total *d*-axis flux that is composed of the magnet flux linkage (λ_m) and the flux produced by the *d*-axis current component of the stator current, λ_q is the *q*-axis flux produced by the *q*-axis component of the stator current, *P* is the number of poles, I_s is the stator current, L_d is the *d*-axis inductance, L_q is the *q*-axis inductance, δ is the current angle, also called the torque angle, which is the angle between the stator current I_s and the *d*-axis. T_m is the magnet torque generated due to the interaction between the magnet flux and the stator current. T_{rel} is the reluctance torque produced by the variation in the magnetic reluctance along the *d* and *q* axes.

The angle for maximum torque can be calculated analytically by differentiating equation (2-1) [16]. However, the obtained analytical solution assumes that the machine inductances and flux linkages are constant, while the actual values depend on the armature current magnitude and current angle (δ). Hence, it is more accurate to obtain the maximum torque and angle relationship using FEA simulations.

The prototyped variable-flux machine is controlled using a vector controlled inverter. In the design of the control scheme, an important consideration is the current angle δ. The torque angle refers to the difference in angle between the magnetic flux axis of the reference stator current and the magnetic flux axis of a permanent magnet within a rotor. In practice, the current characteristics of a PMSM seldom match the ideal characteristics. Owing to the inductance levels of the motor winding process, the commutation induces a phase lag and deviations from the ideal sine-wave current [17]. These non-ideal characteristics of a machine reduce the torque-to-ampere ratio. Hence, in the vector controlled drive the current angle (δ) is used to regulate current vectors at optimal values. As δ can be controlled by the inverter, an appropriate value of δ can improve the torque-to-current ratio and provide optimal motor operation [18, 19].

Torque-angle curves are first simulated in the design software. In MotorSolve, the static torque curves can only be obtained by varying current advance angle, and during a simulation run, the rotor is stationary and aligned at the *d*-axis. In MagNet and MagneForce, the static torque curves can be generated by changing the current advance angle and keeping the rotor stationary, as well as by varying the rotor position and keeping the current angle fixed. In the design software, an alternating current source is connected to the machine, when the torque curves are obtained by varying the current advance angle. When the static torque curves are obtained by changing rotor position, a dc source is connected to the motor, where phase A of the machine is connected to the positive and phase B, and phase C are connected to the negative terminal of the dc source. It is also possible to generate torque-angle curves as a function of both the current angle and the rotor position. However, this is beyond the scope of the research work.

A method described in [20] is used to obtain the torque curves by varying current advance angle. For the prototyped machine, when static torque curves are obtained by varying the current angle, the rotor *d*-axis is first aligned with stator phase A-axis. The rotor shaft is then locked at the *d*-axis on the test bench. From the VSI, three phase ac currents are then applied from 1.414 A rms to 9.9 A rms in steps of 1.414 A rms. The torque angle is varied by varying the angle of the current vector from 0° to 90°. The output torque is recorded for each current magnitude and current angle.

In order to obtain the output torque at different rotor positions, the following process is followed. Initially, the rotor *d*-axis is aligned the with stator phase A-axis. The rotor shaft is then locked at the *d*-axis on the test bench. The prototyped machine is wye connected. During these static measurements, phase A of the machine is connected to the positive, and phase B and phase C are connected to the negative terminal of the dc supply. A fixed dc current equivalent to the peak value of three phase ac current is then supplied to the machine. The value of the applied dc current is from 2 A to 14 A in steps of 2 A. At each current level, the corresponding torque is recorded from the torque transducer. Similarly, the output torque for the angles between the *d*-axis and the *q*-axis of the rotor is obtained.

The magnet flux is then reduced to 75% by applying the demagnetization current pulse of −5 A magnitude. For 50% magnetization, a demagnetizing current pulse of −6.8 A is applied. The same procedures are followed to measure the torque-angle curves for different stator currents at magnetization levels of 75% and 50% respectively.

It is observed from Fig. 2-9 (a), Fig. 2-10 (a), and Fig. 2-11 (a) that the torque curves obtained by changing the current advance angle from the design software do not include the effects of the slot and the space harmonics. The torque curves generated by varying rotor positions contain both the slot and space harmonic effects. This information is quite useful for drives engineers to decide on the bandwidth of the controllers. Although the magnitude of torque curves obtained against the current angle matches with experiments, it is advantageous to obtain the torque curves against the rotor positions to design a more robust controller for the drive system. In addition, the experimental results also have an error band around the measurements. This error band includes the tolerance and resolution of the torque transducer and conditioner.

It can also be seen from Fig. 2-9, Fig. 2-10, and Fig. 2-11 that the measured value of the maximum torque for different stator currents occurs between 60˚ and 70˚ torque angle. The applied magnetizing *d*-axis current component at these torque angles guarantee the stable operation of AlNiCo magnets under high loading conditions. In addition, as the machine is designed with inverted saliency ($L_d > L_q$), the applied magnetizing *d*-axis current component at these torque angles is utilized to produce a positive reluctance torque.

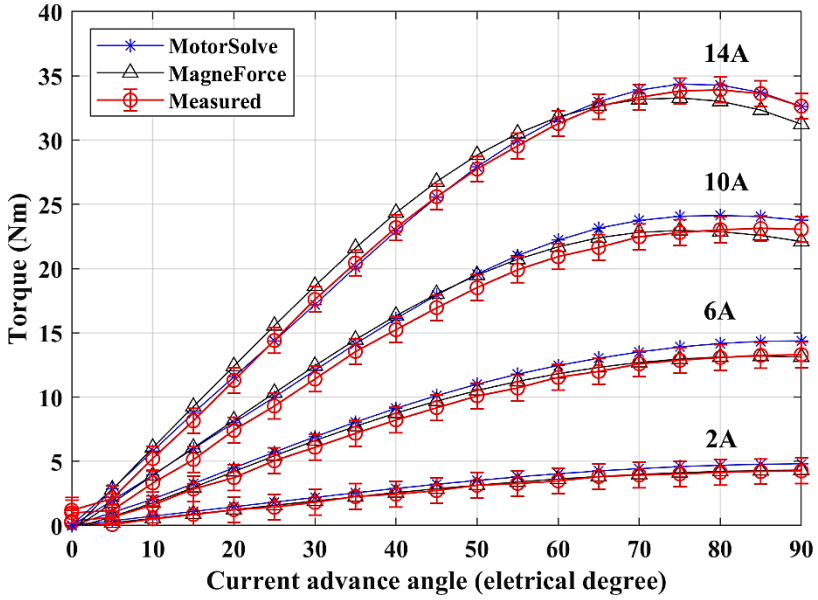

(a)

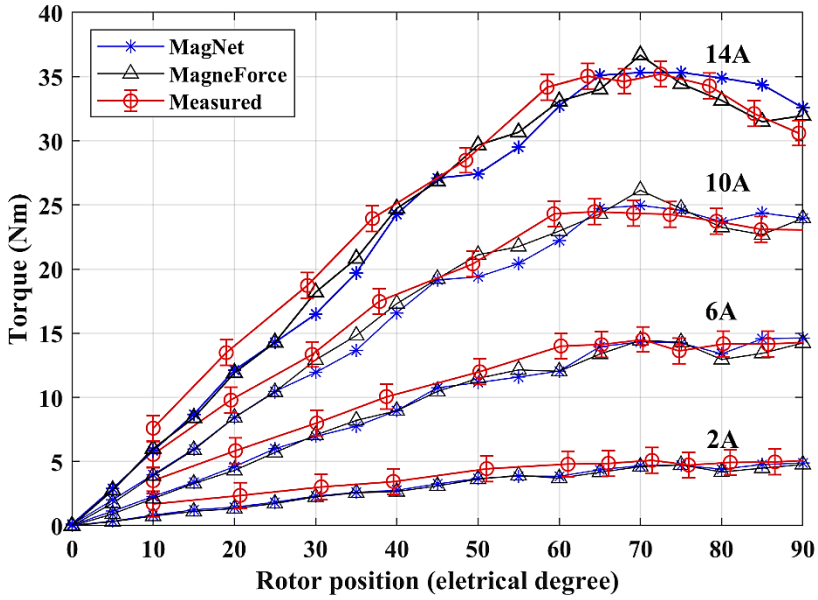

(b)

Fig. 2-9. Torque-angle comparison at 100% magnetization. (a) Measured and simulated torque-angle by varying current advance angle. (b) Measured and simulated torque-angle by varying rotor position.

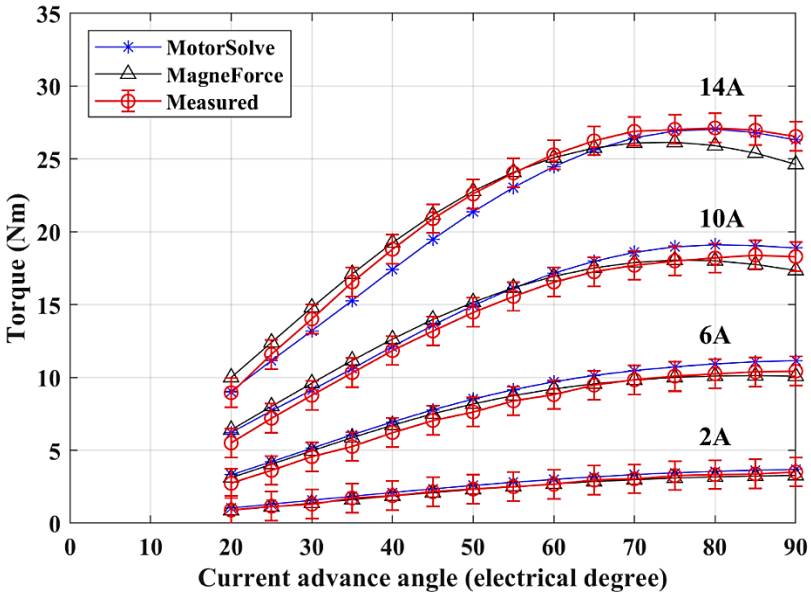

(a)

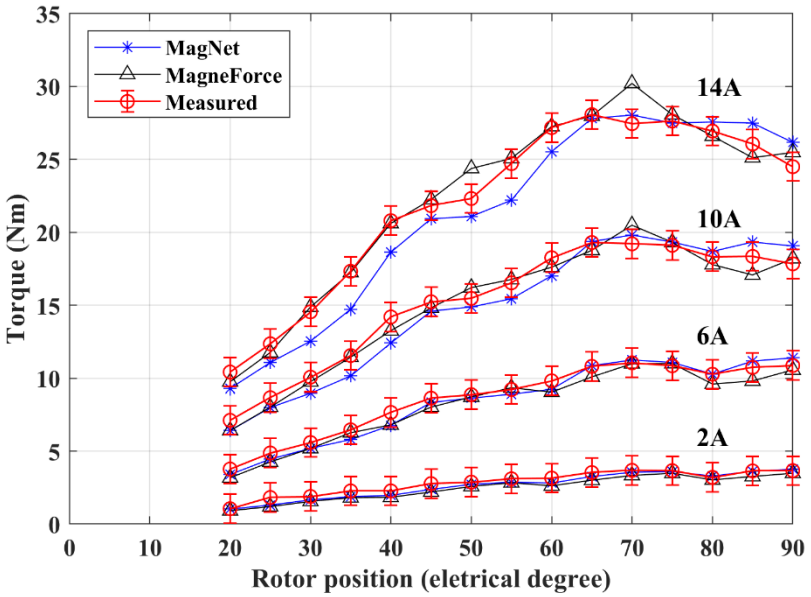

(b)

Fig. 2-10. Torque-angle comparison at 75% magnetization. (a) Measured and simulated torque-angle by varying current advance angle. (b) Measured and simulated torque-angle by varying rotor position.

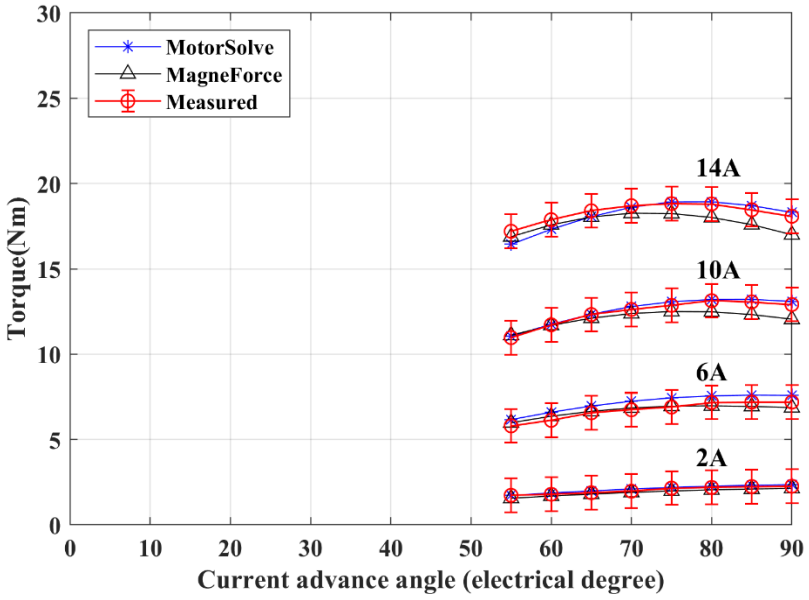

(a)

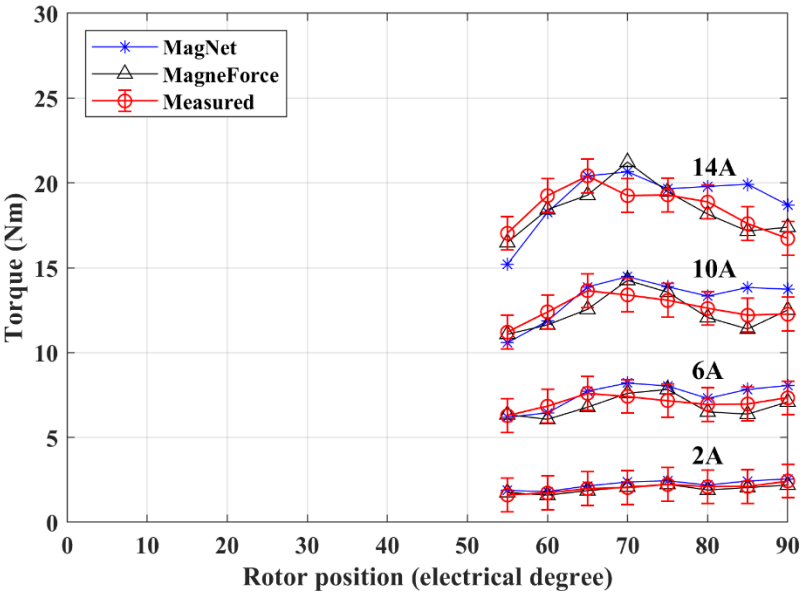

(b)

Fig. 2-11. Torque-angle comparison at 50% magnetization. (a) Measured and simulated torque-angle by varying current advance angle. (b) Measured and simulated torque-angle by varying rotor position.

A comparison shows a good correlation between the measured and simulated torque-angle curves for all magnetization levels. Furthermore, the simulated torque curves obtained by varying the rotor position and current angle are within the error band of the experimental results. This proves the accuracy of the software to simulate the machine design in detail. In

order to analyze the effect of load current on the magnetization state, the back-emf is measured after obtaining torque at each operating point. At 100% magnetization, for rated current of 10 A rms (14 A peak), the current advance angle is varied from 0° (I_d = 14 A, I_q = 0 A) to 90° (I_d = 0 A, I_q = 14 A) and same process is used for the other load currents. During back-emf measurement no change in the magnetization state is observed for any of the current advance angles and load currents. During experiments at 75% magnetization, it is observed that the magnetization level is increased, when the current advance angle is varied from 0° (I_d = 14 A, I_q = 0 A) to 15° (I_d = 13.52 A, I_q = 3.62 A) at the rated current of 10 A rms (14 A peak). The magnetization level is stable for the current advance angle from 20° to 90°. Also, during experiments at 50% magnetization, the magnetization level is increased at rated current, when the current advance angle is varied from 0° (I_d = 14 A, I_q = 0 A) to 50° (I_d = 8.99 A, I_q = 10.72 A) and the magnetization was stable for the current advance from 55° to 90°. Thus, at reduced magnetization levels, in order to avoid magnet magnetization, the prototyped variable-flux machine should not be operated below a certain torque angle. Hence, at 75% magnetization, the torque curves are obtained for the current advance angle from 20° to 90° for all load currents, and at 50% magnetization, the torque curves are obtained for the current advance angle from 55° to 90° for all load currents. This information is not available from simulations, as they are carried out with a static magnetization curve which does not reflect the actual dynamic operation of the magnets.

2.4 Core Loss Characterization

Core losses are typically a combination of several losses, which are frequency and flux density dependent. Therefore, for an accurate estimation of core losses, the loss components have to be well modeled. For better modeling of the core losses; when obtained both from analytical models and from measured data, core loss separation is imperative. Using the core loss separation approach, various physical influences on electrical steel due to frequency and flux density variations can be investigated. Moreover, when core losses are separated, it is easy to measure them and also be able to model them for general application in machine design or efficiency estimation. In this section, core loss separation, an analytical method to separate core losses at high frequencies in the steel laminations, and its application to predict the core losses in the prototype variable-flux machine are discussed. Measurement of core losses for the

variable-flux machine is also presented. A comparison is carried out of the core losses data obtained from the design software, an analytical method, and experiments.

2.4.1 Core loss separation

Traditionally, Steinmetz [21] modeled core losses by a two-term equation consisting of eddy current and hysteresis losses, and the specific total core loss is given by

$$P = K_h f B^n + K_e f^2 B^2 \tag{2-3}$$

where K_h, K_e, and n are the loss coefficients which are dependent on the material. However, (2-3) shows large discrepancies compared to the experimental results, particularly at high flux densities and high frequencies. This difference is normally described by the excess losses. In [22], Bertotti proposed an additional term to account for the excess losses based on the statistical loss theory. The Steinmetz core loss formula was modified to

$$P = K_h f B^n + K_e f^2 B^2 + K_{ex} f^{1.5} B^{1.5} \tag{2-4}$$

where K_{ex} is dependent on the material micro-structure, the conductivity, and the cross section area of the lamination.

The above specific core loss formulae use the extrapolation method to calculate the hysteresis loss per cycle with an assumption of a uniform flux density distribution across the lamination thickness, which is true only at low frequencies. These methods are widely used in the literature for loss separation and total loss calculation [23, 24, 25, 26, 27]. However, none of these models consider any physical characteristics occurring in the material. Moreover, the majority of these core loss formulae to some extent use curve fitting techniques and therefore can only work within a limited range of frequencies and flux densities. In addition, core loss data over a large frequency and flux density range are required to calculate the specific total losses. A large error can result if the model is used with the data beyond the range. One of the reasons for constraints associated with these models is the exclusion of the physical characteristics occurring in the material. Therefore, in order to obtain analytical solutions of Maxwell's equation, a method is required that incorporates a proper assumption of the magnetic properties of the materials based on physical understanding.

It has also been validated in [28] by means of FEA that the excess losses are primarily associated with the non-uniform distribution of the magnetic field in the lamination generated

by both the non-uniform distribution of the magnetic field and the skin effect. Hence, the specific total core losses can be characterized by the hysteresis and eddy current losses considering the realistic field distribution. The static hysteresis energy loss per cycle can be obtained by measuring the area enclosed by the hysteresis loop under static excitation. Nevertheless, special measuring devices are required for the measurement of the static loop [27]. It is also possible with the present FEA tools to separate core loss components in a short simulation run time. However, FEA models require a large core loss data at different frequencies and flux densities for various materials.

Various models are available to determine the eddy current losses considering the skin effect. However, these models do not include the hysteresis energy loss calculation due to the non-uniform magnetic field distribution. Hence, a better loss separation method is required as the method used in a model also affects the models' results.

2.4.2 Finite section method

A rapid and efficient finite section method for the separation of core losses using an analytical model to describe the flux density distribution across the lamination is proposed in [29]. The proposed method is implemented to separate hysteresis loss in M19G29 laminations and later applied to the prototyped variable-flux machine. First, the core losses are measured for M19G29 steel using an Epstein frame. The core losses are obtained at different frequencies between 20 Hz and 1000 Hz, and for a flux density of up to 1.75 T. The static hysteresis energy loss per cycle is then extrapolated from the measured core losses of 20 Hz and 30 Hz respectively. At these frequencies the influence of skin effect is negligible. The total hysteresis loss is obtained by multiplying the frequency by the static hysteresis energy loss per cycle. Also, the eddy current loss can be assumed dependent on the square of the frequency. Hence, the specific total core loss can be given by

$$P_t = Kf^2 + W_h f \tag{2-5}$$

where K depends on the lamination and the flux density, and W_h is the hysteresis energy loss per cycle. By using the measured core loss data P_{t1} and P_{t2} at frequencies f_1 (30 Hz) and f_2 (20 Hz), W_h is calculated using

$$W_h = \frac{(P_{t2}f_1^2) - (P_{t1}f_2^2)}{(f_1 f_2)(f_1 - f_2)} \tag{2-6}$$

The Steinmetz hysteresis loss formula given in (2-3) is only valid for the flux densities up to 1 T. Hence, a revised formula applicable for higher flux densities is used in the model which was proposed in [23, 26] as follows:

$$W_h(B) = K_h B^{a+bB+cB^2} \tag{2-7}$$

where $K_{h,}$ a, b, and c are the curve fitting constants. The values of these constants are obtained by curve fitting W_h of (6) against the flux density. Fig. 2-12 shows the curve fitting graph and the constant values are obtained as K_h=0.01348, a=1.8, b=0.6149, and c=0.0103.

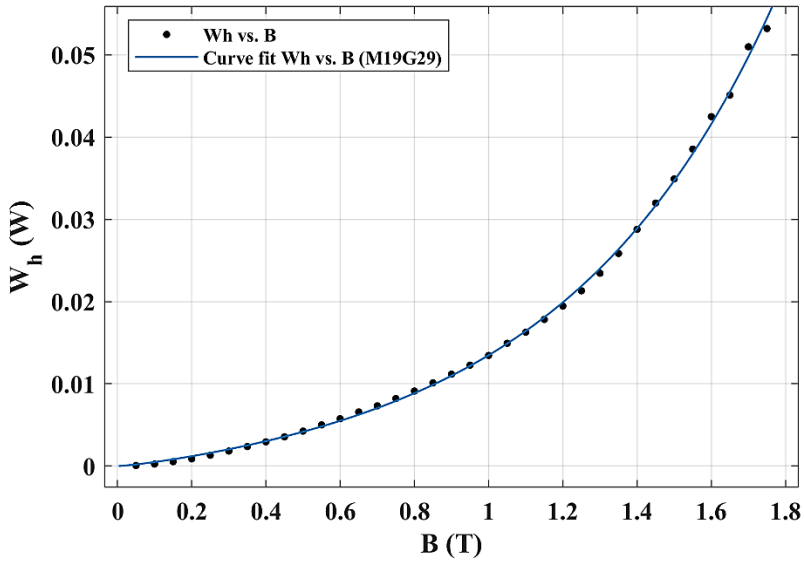

Fig. 2-12. Curvefit W_h vs. B.

A flux distribution model is implemented to include the influence of the skin effect on hysteresis losses. The flux density at a position y from the center of the lamination is obtained by equation (2-8) [30], where $\hat{y} = y/L$, ω, μ, σ, L, and B_b are the angular frequency, the magnetic permeability, the electrical conductivity, half the lamination thickness, and the flux density magnitude at the boundary, respectively.

$$B_p(\hat{y}) = B_b \sqrt{\frac{\cosh\left(\frac{2\hat{y}}{\lambda}\right) + \cos\left(\frac{2\hat{y}}{\lambda}\right)}{\cosh\left(\frac{2}{\lambda}\right) + \cos\left(\frac{2}{\lambda}\right)}} \tag{2-8}$$

$$\lambda = \sqrt{\frac{2}{L^2 \omega \mu \sigma}} \tag{2-9}$$

$$B_{ave,p} = B_b \lambda \frac{\sqrt{0.5 * \left[1 + exp\left(\frac{8}{\lambda}\right) - cos\left(\frac{4}{\lambda}\right) exp\left(\frac{4}{\lambda}\right)\right]}}{1 + 2\,cos\left(\frac{2}{\lambda}\right) exp\left(\frac{2}{\lambda}\right) + exp\left(\frac{4}{\lambda}\right)} \tag{2-10}$$

Due to the skin effect, in the measurement, the average flux density B_{ave} is different from the flux density B_b at the boundary. Hence, the peak value of the average flux density B_{avg_p} can be calculated using equation (2-10) [31].

Using Maxwell's equation with an assumption of uniform magnetic material, equations (2-8) and (2-10) are found. Nevertheless, the permeability of material also changes along the hysteresis curve subjected to the flux density level and therefore, permeability variation affects the flux density distribution through the lamination thickness. Hence, in order to consider the variation of field distribution with the flux density level, the magnetic permeability is varied with the flux density as a sum of sinusoidal function and is given by

$$\begin{aligned}\mu(B) = {} & (p_1 \times \sin(q_1 \times B + r_1)) + (p_2 \times \sin(q_2 \times B + r_2)) + \\ & (p_3 \times \sin(q_3 \times B + r_3)) + (p_4 \times \sin(q_4 \times B + r_4)) + (p_5 \times \sin(q_5 \times B + r_5))\end{aligned} \tag{2-11}$$

where p_1 to p_5, q_1 to q_5, and r_1 to r_5 are curve fitting coefficients calculated from the measured magnetic permeability at the frequency of 20Hz as shown in Fig. 2-13.

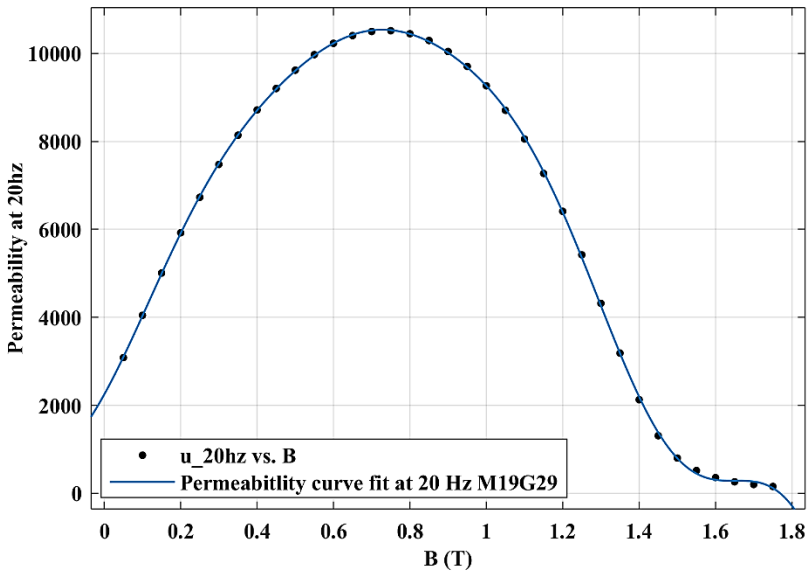

Fig. 2-13. Permeability curve fit.

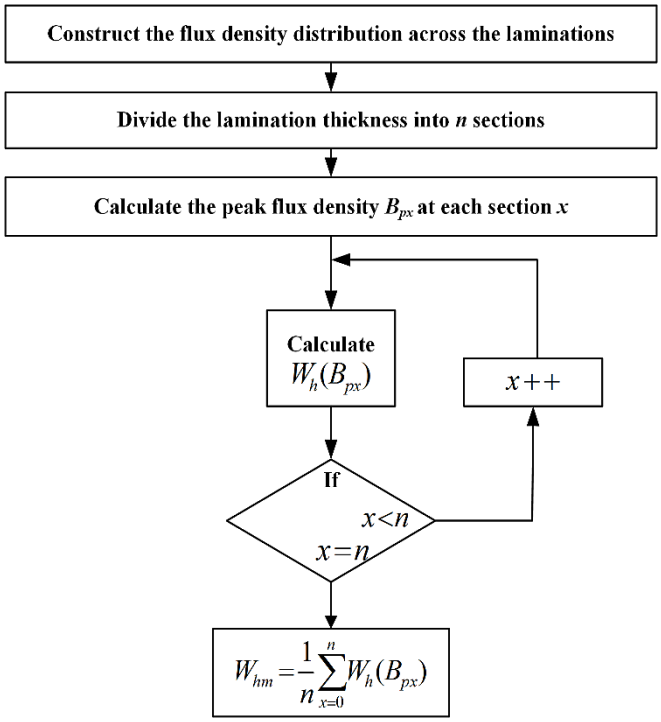

Fig. 2-14. Finite section method flow chart [29].

A mathematical model with the realistic flux distribution is adopted for precise assessment of the hysteresis losses in the lamination. In the model, first, the flux density distribution across the lamination thickness is first created using (2-8) to (2-11). The lamination is then divided into n different sections that are small enough to assume the uniform flux distribution in the sections. At each section, the hysteresis energy loss per cycle is calculated from (2-7) and by averaging the losses of all individual sections, the total hysteresis loss of the lamination is obtained. The model flow chart is shown in Fig. 2-14.

The eddy-current losses were obtained using the formula proposed in [31] as

$$P_e = \frac{\omega K_E B_{avg}^2}{2\lambda\mu\rho} \frac{\left[1 + exp\left(\frac{4}{\lambda}\right) + 2cos\left(\frac{2}{\lambda}\right) exp\left(\frac{2}{\lambda}\right)\right]\left[exp\left(\frac{4}{\lambda}\right) - 2\, exp\left(\frac{2}{\lambda}\right) \sin\left(\frac{2}{\lambda}\right) - 1\right]}{1 - 2\, cos\left(\frac{4}{\lambda}\right) exp\left(\frac{4}{\lambda}\right) + exp\left(\frac{8}{\lambda}\right)} \qquad (2\text{-}12)$$

where ρ = 7650 kg/m^3 is the mass density of M19G29 steel and K_E is a factor derived from [32] using the measured core loss and the hysteresis loss obtained from the finite section method. The value of the K_E used in the model is 1.6519, and that is obtained at 600Hz and 1.2T. In Fig. 2-15(a), (b), (c), and (d), the separated hysteresis losses, eddy-current losses, and total core losses estimated using the analytical method for M19G29 lamination are presented.

In addition, the total measured core losses from the Epstein frame and the core losses from the manufacturer datasheet are also included for comparison purposes. The manufacturer's data were obtained from the laminations steel database of electric motor education and research foundation [33]. Fig. 2-15(a), (b), (c), and (d) illustrate the loss comparison at 60Hz, 200Hz, 600Hz, and 1000Hz, respectively. The analytical losses are in a good agreement with the Epstein measurements and the manufacturer's data. Hence, the analytical method was utilized to estimate the core losses of the prototyped variable-flux machine.

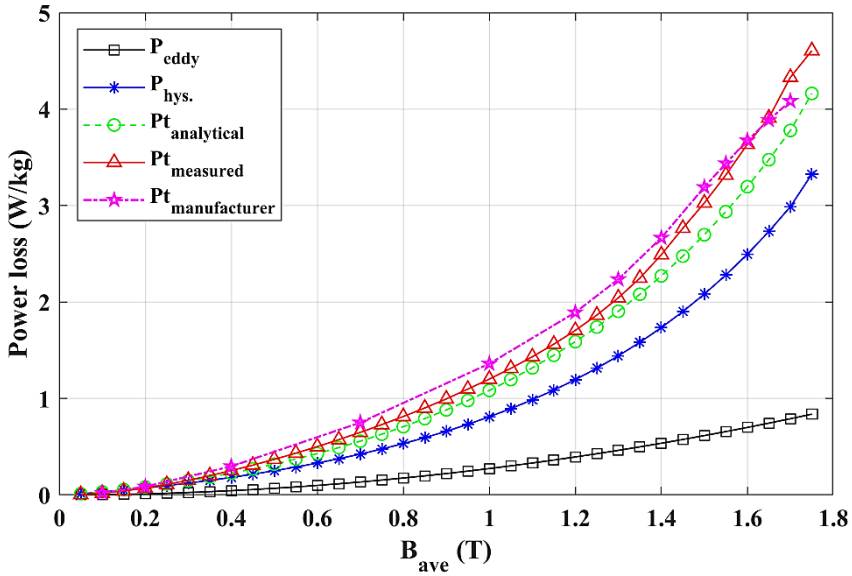

(a)

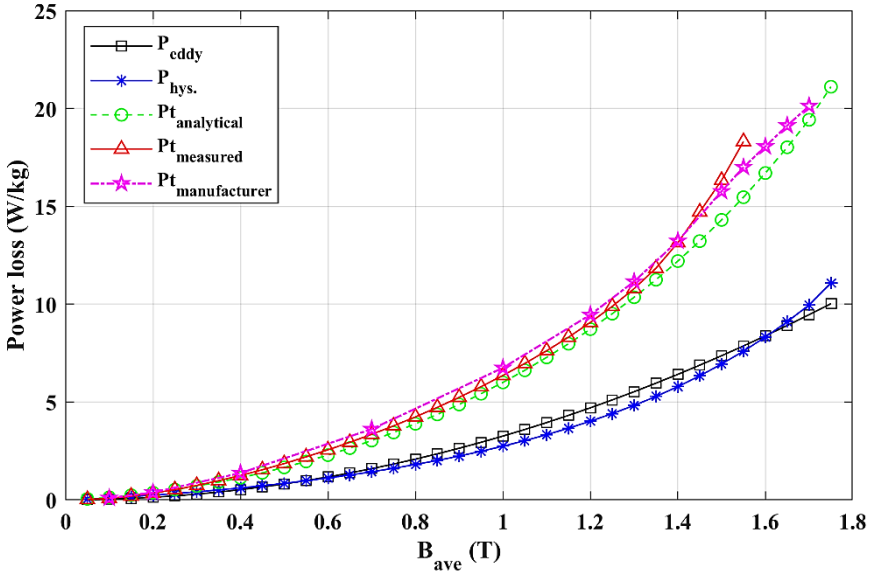

(b)

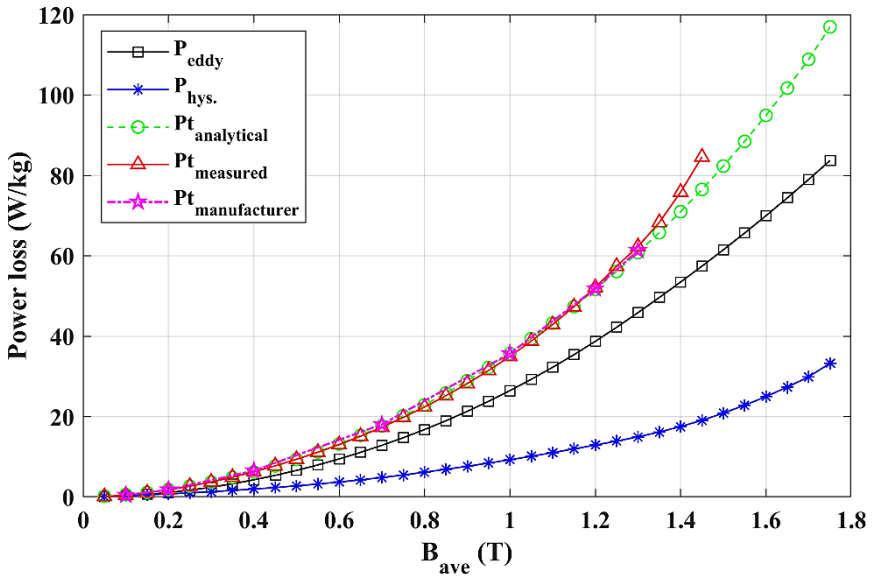

(c)

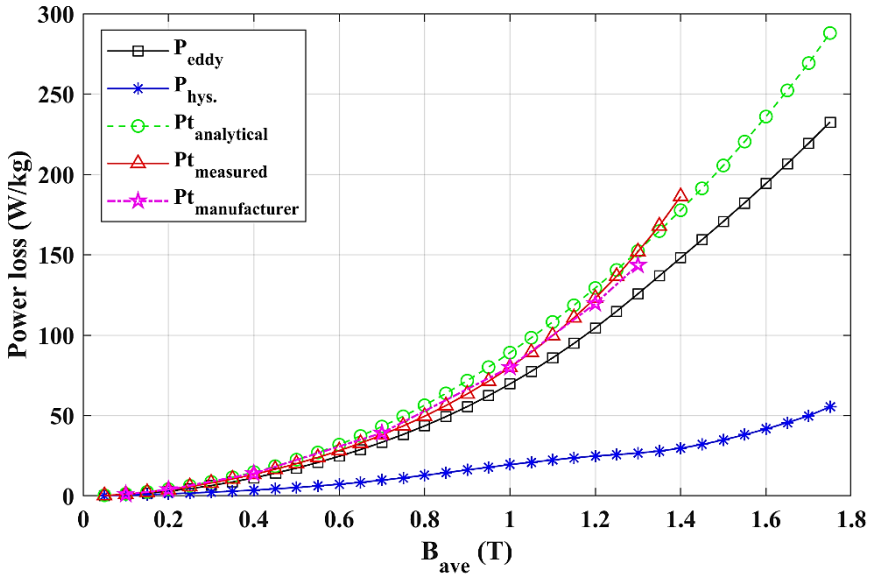

(d)

Fig. 2-15. Comparison of core losses in the lamination. (a) at 60Hz. (b) at 200 Hz. (c) at 600 Hz. (d) at 1000 Hz.

In order to estimate the core losses of the prototyped variable-flux machine using the analytical method, the flux density waveforms of the stator are required. To construct the flux density waveforms, no-load mesh data are obtained from MagneForce FEA software. Mesh element data are obtained for 60 different rotor positons from 0° to 120° to complete one electrical cycle. Element parameters such as coordinates, area, as well as the orthogonal components of the flux density, B_x and B_y are extracted at each rotor position. Then, using the

element data, the radial component B_{rad} and the tangential component B_θ of the flux density waveform for each element are constructed using (2-13), (2-14), and (2-15), where θ is the angle of the element.

$$B_{rad} = |B| \times cos\theta \tag{2-13}$$

$$B_\theta = |B| \times sin\theta \tag{2-14}$$

$$|B| = \sqrt{B_x^2 + B_y^2} \tag{2-15}$$

The hysteresis and the eddy current losses of the machine are calculated using radial and tangential flux density waveforms. For the hysteresis loss, first, the flux density distribution across the element thickness is created using (2-8) to (2-11) for both B_{rad} and B_θ. Each mesh element is then divided into 20 sections. At each section, the hysteresis energy loss per cycle is calculated from (2-7) for both components. For each element, the losses of all 20 sections are then averaged, and the hysteresis loss of each element is obtained by adding the losses due to B_{rad} and B_θ waveforms. The total hysteresis loss of the machine is obtained from the summation of the losses of each mesh element. The radial and tangential flux density waveforms are comprised of a series of harmonics. Hence, an FFT is carried out for B_{rad} and B_θ waveforms of each element. The eddy current losses are then calculated based on the magnitude and the frequency of the harmonics using (2-12), and the value of the factor K_E used in the model is 1.43. For each element, the eddy current losses are calculated for harmonics up to 16^{th} order. Eddy current losses due to all harmonics are then added to obtain the eddy current loss of the element. The total eddy current loss of the machine is obtained from the summation of the element losses.

In the design software of MotorSolve, MagNet, and MagneForce, the core losses are obtained using transient simulations. Moreover, in order to incorporate the eddy current losses of the magnets, the conductivity of the AlNiCo magnet is included during the design and simulations. At present the adopted core loss models in commercial machine design softwares are based on calculating the core losses using curve fitting techniques. Moreover, the core loss data in the software are provided by steel manufacturers which are generally obtained under sinusoidal excitations of 50 or 60 Hz and at a flux density of 1 T. In order to improve the

accuracy of the core loss prediction and also for better assessment, the measured core losses of M19G29 steel are then incorporated in the design software.

For core loss measurement the experimental setup shown in Fig. 2-4 is used. The variable-flux machine is coupled to a dc dynamometer so that it could be run as a generator. The magnet flux is initially reduced to approximately 0.0015 V.s (0.3%). The variable-flux machine is then run as a generator from 200 rpm to 2000 rpm in 200 rpm speed intervals. During each speed interval, the output torque of the dc machine is measured and utilized for the input power measurement of the variable-flux machine. When the magnets are completely demagnetized, the measured input power at different speed provides the approximate value of the friction and windage loss of the variable-flux machine. These friction and windage losses are then subtracted from the input power obtained when the variable-flux machine is run at 100% , 75%, and 50% of the magnet flux, respectively.

Fig. 2-16 (a), (b), and (c) present the measured, analytical, and simulated core losses of the prototyped variable-flux machine at 100%, 75%, and 50% magnet flux, respectively. The core loss comparison in Fig. 2-16 demonstrates that the core losses obtained from MotorSolve and MagNet are in a close agreement with the measured and analytical core losses for all three magnetization levels. MagneForce underestimates the core losses for all three magnetization levels. The core losses obtained from the analytical method correspond well with the simulated and measured core losses. This analysis presents the advantage of performing core loss analysis of a special machine like a variable-flux, using different FEA software and an analytical method. Due to the maximum speed limitation of the available dynamometer, the core losses can only be obtained for the maximum speed of 2000 rpm, which is 1.6 times the base speed and the machine is operating at 100 Hz frequency. Hence, no significant difference is observed among the core losses obtained from the software, analytical method, and the measurements. It can also be seen from Fig. 2-16 that there is inconsistency in the measured core losses. One of the possible causes of the deviation is the variation of the dc dynamometer armature circuit resistance.

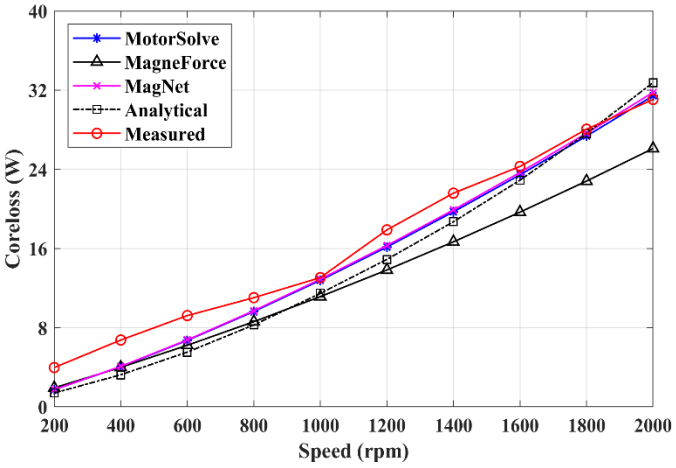

(a)

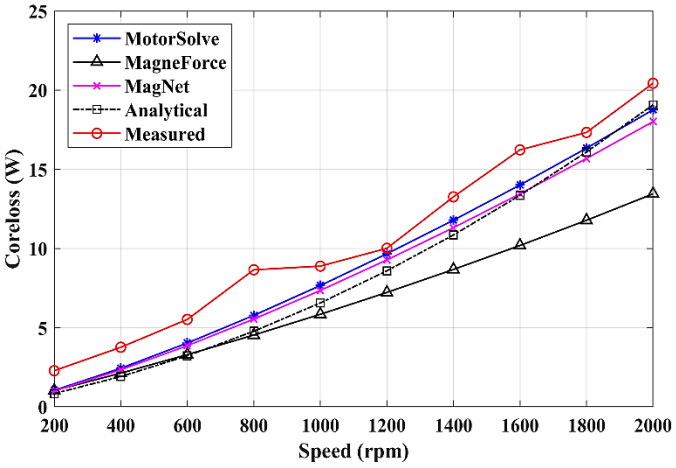

(b)

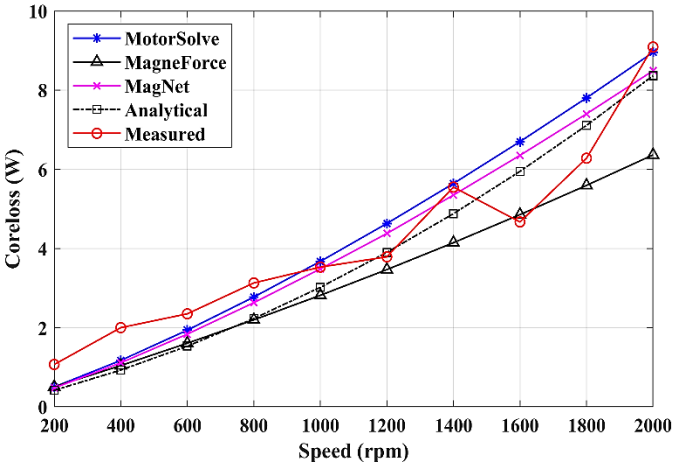

(c)

Fig. 2-16. Comparison of simulated, analytical, and measured core losses. (a) at 100% magnetization. (b) at 75% magnetization. (c) at 50% magnetization.

2.5 Summary

In this chapter, the back emf, magnet flux linkage, torque-angle, and core loss characterization of a 7.5 hp variable-flux permanent-magnet machine with AlNiCo magnets were presented. To validate the design methodologies, the accuracy of machine design software, and machine models, the designed variable-flux machine was simulated with three different machine design softwares namely, MagneForce, MotorSolve, and MagNet. The measurements and simulations were carried out at 100%, 75%, and 50% magnetization, respectively. All measurements were performed on the test setup shown in Fig. 2-4. A comparative analysis was performed among the results obtained from software and experimental characterizations.

For the prototyped machine, the magnetic properties of AlNiCo 9 magnet, as well as the static magnetization and demagnetization process of the AlNiCo magnets were described in 2.3. To estimate the magnitude of the magnet flux linkage, first the back emf was obtained, and the peak value of the fundamental component was obtained from an FFT and the rms value of the waveform. The peak value of the fundamental component was divided by the electrical speed of the machine to obtain the value of the magnet flux linkage. Fig. 2-7 and Table 2-III present the back emf and magnet flux linkage comparison, which show a considerable agreement between the simulation and the measurement.

The torque curves were obtained by varying both the current advance angle and the rotor position. Torque measurement by varying the current angle consumes less time compared to the torque measurement by varying rotor position. However, the torque curves generated by varying rotor positions contain both the slot and the space harmonics' effects and this is a very useful information for drives engineers to decide on the bandwidth of the controllers. Hence, it is advantageous to obtain the torque curves against the rotor positions from the drive aspect. The torque-angle comparison presented an acceptable match between the measured and the simulated torque-angle curves for all magnetization levels. As stated earlier the simulation results were within the error band of the experimental results. However, during the experiments at 75% and 50% magnetization, the AlNiCo magnets were magnetized when the rated current was applied. Thus, at reduced magnetizations, in order to avoid the possibility of magnet magnetization at all load currents, the torque curves were obtained from 20° to 90° at 75% magnetization and at 50% magnetization, the torque curves were obtained from 55° to 90°. This

information is not available from simulations, as the simulations were carried out with the static magnetization curves which do not reflect the actual dynamic operations of the magnets. It would be beneficial if the commercial FEA softwares could incorporate the dynamic non-linear hysteresis loops of the AlNiCo magnets.

Core loss characterization was discussed in section IV. Core losses were separated using an analytical model based on the finite section method proposed in [29]. The model was first applied to separate core losses in M19G29 steel laminations, and the results were compared with the experimental data obtained from the Epstein frame and with manufacturer's data. As a result of the considerable accuracy, the model was then implemented to predict the core losses in the prototyped variable-flux machine. In the design software of MotorSolve, MagNet, and MagneForce, the core losses were obtained using transient simulation, and the conductivity of the AlNiCo magnet was also considered to include the magnet eddy current loss. The core loss comparison in Fig. 2-16 demonstrates that the core losses obtained from MotorSolve and MagNet were in close proximity to the measured and analytical core losses for all three magnetization levels. However, the MagneForce underestimates the core losses for all three magnetizations. Moreover, the variation of dynamometer armature circuit resistance caused a deviation in the measured core losses. The comparative analysis of core loss shows the advantage of performing core loss analysis of a special machine like a variable-flux, using different FEA softwares and an analytical method.

Chapter 3 Fabrication and Assembly Method for Synchronous Reluctance Machines

The desired performance of a machine necessitates a precise manufacturing and assembly of its different components. In this chapter, a comprehensive manufacturing and assembly process of synchronous reluctance machines (SynRMs) is presented. One stator and two transversally laminated anisotropic (TLA) SynRM rotors are manufactured using cold-roll nongrain-oriented (CRNGO) steel. To enhance the performance of the designed SynRM, a TLA segmented SynRM rotor is fabricated using cold-roll graino-riented steel (CRGO). Various laminations cutting methods are discussed. The application of nontraditional photochemical machining (PCM) process to cut SynRM stator and rotor laminations to achieve high-dimensional tolerances is also presented. In addition, different stages of manufacturing, stator and rotor assembly techniques, rotor balancing procedure as well as specialized components used at various stages of the process are described.

3.1 Introduction

The requirements of advanced powertrains of electric vehicles (EVs) and hybrid electric vehicles (HEVs) are high performance electric machines with high efficiency and low construction cost. Thus, the selection process of an appropriate electric motor for traction is critical [1, 34]. The unstable cost of rare-earth magnets and limited resources have caused a shift towards a new generation of machine technologies which do not have permanent magnets. The synchronous reluctance machine (SynRM) has been gaining attention for traction applications as it does not use permanent magnets (PMs). Hence, it is immune to the fluctuating prices of PMs. In addition, the SynRM rotor structure is simple and only made of steel, and it does not have a copper or aluminum cage in the rotor which reduces the rotor losses significantly. Hence, it has a low-priced construction and can have acceptable power and torque densities, and flux-weakening capability. The SynRM is less expensive compared to the permanent magnet synchronous machine (PMSM) with possibility of higher efficiency compared to the induction machine (IM) [35].

The SynRM is a singly excited salient machine, and the operating principle of the SynRM was developed more than a century ago [36]. This is based on the variation of reluctance for

developing torque, necessitating that the *d*-axis and *q*-axis inductance ratio and difference be as high as possible. In a SynRM there are no rotor copper losses. This allows SynRM to operate at a continuous torque that is at least equivalent to other wound or cage rotor machines of the same size. In order to accomplish these requirements, the rotor geometry of the SynRM has to be designed such that the ratio of the *d*-axis and *q*-axis inductances, known as saliency ratio (ξ), is to be as high as possible. In order to achieve a higher saliency ratio, axially laminated anisotropic (ALA) and transversally laminated anisotropic (TLA) rotor geometries are investigated. Between the two rotor geometries, the TLA rotor is preferable in many applications because of its ease of manufacturing and lower core losses [37]. Fig. 3-1 presents an example of a TLA type rotor.

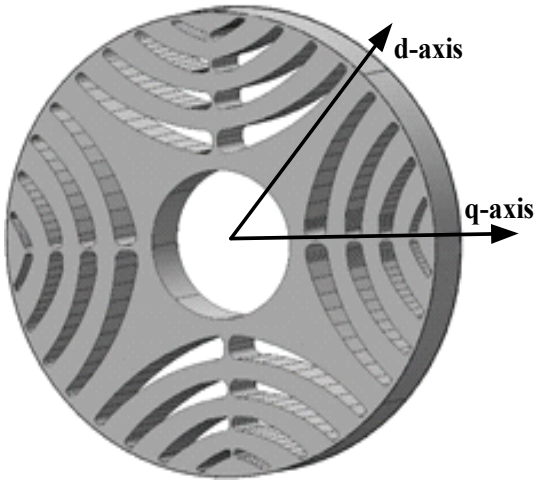

Fig. 3-1. Illustration of a 4-pole TLA rotor

It is intricate to achieve optimal SynRM performance in terms of output torque, power factor, torque ripple, efficiency, and choosing the flux-barrier parameters of the rotor due to various parameters of the SynRM machine. Hence, a sizing methodology is required to optimize the machine parameters to obtain better performance. In [38], a detailed sizing methodology was proposed to size a SynRM to meet a specific torque-speed characteristic for traction applications. The proposed method is based on the mathematical model of the machine, equivalent circuit, initial data, and some assigned parameters. The sizing process of the proposed machine starts with formulating initial data and assigning the key parameters, which are used to obtain geometric, magnetic, and electric parameters of the machine, along with the mathematical model.

Fig. 3-2 represents the rotor slot pitch angle (α) and stator slot pitch angle (β) in a single pole of a four-pole, 36-slot stator, and four-layer rotor SynRM. The SynRMs have higher torque ripple compared to the PMSM and IM, which are produced due to rotor anisotropy [39, 40], as shown in Fig. 3-2. In the SynRM, the torque ripples are primarily produced by stator and rotor slot interaction and depend on the placement of the stator and rotor slot openings. Moreover, the stator slot pitch angle (β) and rotor slot pitch angle (α) have a significant effect on the torque ripple. In order to reduce torque ripple, various methods were proposed in [41, 42, 43, 44]. In [45], for a TLA rotor, a new method to obtain a promising value of the rotor slot pitch angle (α) as a function of the most important geometrical parameters was proposed for reducing the torque ripple produced due to the stator and rotor slotting mutual effect.

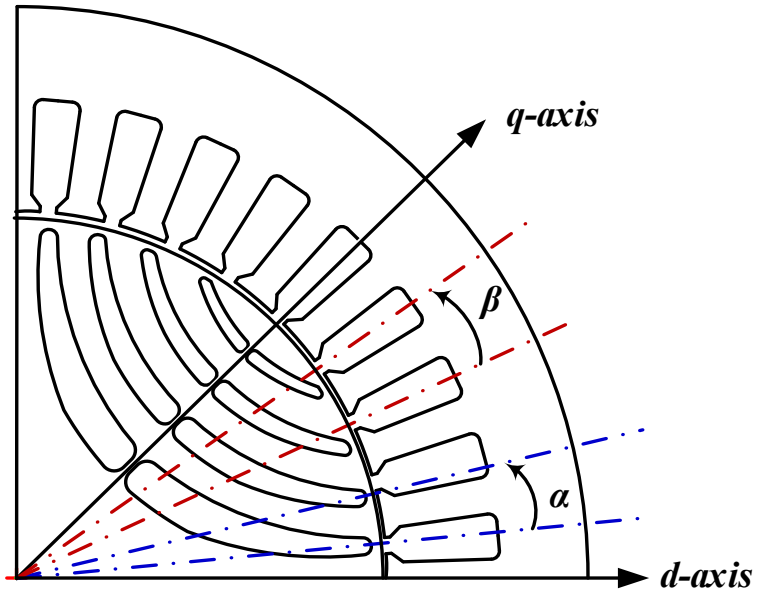

Fig. 3-2. Stator and rotor slot pitch illustration for a 4-pole TLA rotor.

Today, the majority of the rotating electric machines are manufactured using nonoriented steel cores which possess significant core loss. In order to enhance the performance of ac machines in terms of reduced core loss, higher saliency, efficiency, torque density as well as compactness, the machines can be fabricated with grain-oriented (GO) segmented laminations as GO steel has lower core loss. However, as a result of the high anisotropy of GO steels, their utilization was limited to high power synchronous machines [46] and ALA rotors of SynRMs [47]. In the recent past, the application of GO steel for small and medium power induction machines was presented in [48], where the nonsegmented stator core is assembled by shifting

each GO lamination from the previous one with a constant spatial angle. Moreover, in order to achieve higher saliency, efficiency, torque density, and compactness for a high performance SynRM for traction applications, an innovative design of a TLA segmented rotor with cold-roll grain-oriented (CRGO) steel was also proposed in [45]. An individual set of one-pole laminations is produced from CRGO steel sheets in a way that the direction of the q-axis of a pole is perpendicular and the d-axis is parallel to the rolling direction of the steel sheet.

In the TLA rotors, design parameters such as the number of poles, number of flux guides and barriers, location and size of the barriers and guides, insulation ratio, air gap length, as well as the width of radial and tangential ribs have significant effects on the saliency ratio. In addition, geometrically the width of the tangential and radial ribs have a considerable effect on the rotor mechanical integrity during the high-speed operations [49]. Thus, the influence of the magnetic and rotational forces on the rotor geometry must be analyzed prior to manufacturing. Special care should be taken during the design as well as during manufacturing and assembly of the rotor parts.

3.2 Synchronous Reluctance Motor Specifications

In the method proposed in [45] to reduce torque ripple of the SynRM, the rotor geometry is designed for nonidentical stator slot pitch (β) and rotor slot pitch (α) in a way that when one end of a flux barrier moves to a corresponding stator slot, the opposite end of the flux barrier departs from a corresponding stator slot. Hence, when the machine rotates, one flux barrier end produces positive torque pulsation and the other negative, which in turn cancels each other, thus reducing the total torque ripples produced by the stator and rotor slots mutual effects.

In order to validate the sizing methodology proposed in [38] as well as the method to reduce torque ripple in TLA SynRM rotors and the novel TLA segmented CRGO rotor geometry proposed in [45], one stator and two TLA rotors with different rotor slot pitches (α) are designed and fabricated using M15G29 CRNGO steel. In addition, one segmented pole rotor is manufactured with M5 CRGO laminations. The stator and rotors are fabricated according to the specification listed in Table I [50]. All rotor geometries are designed with four poles and four internal layers.

Table 3-I Machine Specification

Rated power	7.5 hp	
Peak torque	60 Nm	
Rated current	20 A	
Rated voltage	230 V	
Base speed	850 rpm	
Number of poles	4	
Number of slots	36	
Air gap	0.4 mm	
Magnetic loading	0.8 T	
Rotor internal layers	4	
Winding type	distributed, fully pitched	
Winding turns	25	
Winding connection	delta (Δ)	
Stator outer diameter	208 mm	
Rotor outer diameter	134.2 mm	
Stack length	200 mm	
Saliency ratio (L_d/L_q)	5	
Electrical steel	Stator	CRNGO M15G29
	Two non-segmented TLA rotors	CRNGO M15G29
	Segmented TLA rotor	CRGO M5
Frame size	NEMA 215T (IEC 132)	

Fig. 3-3(a) and (b) present the prime dimensions of the stator, slot, and teeth of the prototyped SynRM. The stator lamination is shown in Fig. 3-3(c). The stator is wound with a fully pitched distributed single-layer winding. The winding coil has 25 turns and is made of two strands of 16-AWG copper wire. H class insulation is used. The stator of the SynRM is installed

in a NEMA 215T (IEC 132) frame size cast iron body. This is the maximum frame size of the motor that can be installed on the dynamometer test bench of the laboratory. Therefore, the outer diameter of the stator and other motor dimensions are selected accordingly. The detailed design of the SynRM machines is discussed in [50].

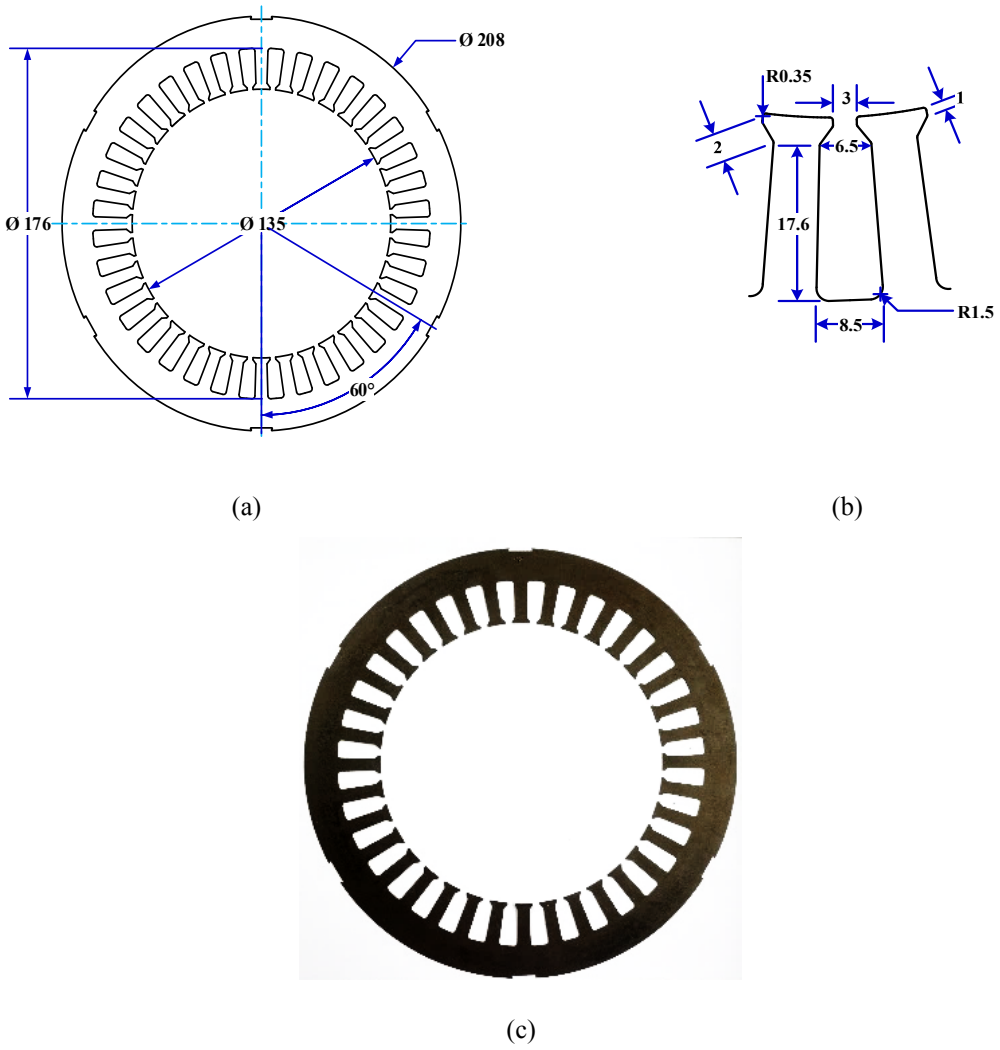

Fig. 3-3. (a) Stator dimensions in mm. (b) Stator slot and teeth dimensions in mm. (c) Prototype stator lamination.

The fabrication drawing with the main dimensions of two different TLA CRNGO rotors is shown in Fig. 3-4(a) and Fig. 3-5(a). The rotor of Fig. 3-4(a) is designed with a rotor slot pitch (α) of 8.5°, which is lower than the stator slot pitch (β) of 10°. The rotor of Fig. 3-5(a) is designed with equal rotor and stator slot pitch angle ($\alpha = \beta = 10°$), where the stator slot openings and the rotor barrier ends are identical. The lamination prototype of the rotor with $\alpha = 8.5°$ and

10° is shown in Fig. 3-4(b) and Fig. 3-5(b), respectively. The provision of a 4 mm × 8 mm key way is made to interlock rotor laminations with the motor shaft as illustrated in Fig. 3-4 and Fig. 3-5. Moreover, in order to align and clamp rotor laminations, four 6.5 mm guided pin holes are created between the barriers on the rotor lamination, as shown in Fig. 3-4 and Fig. 3-5.

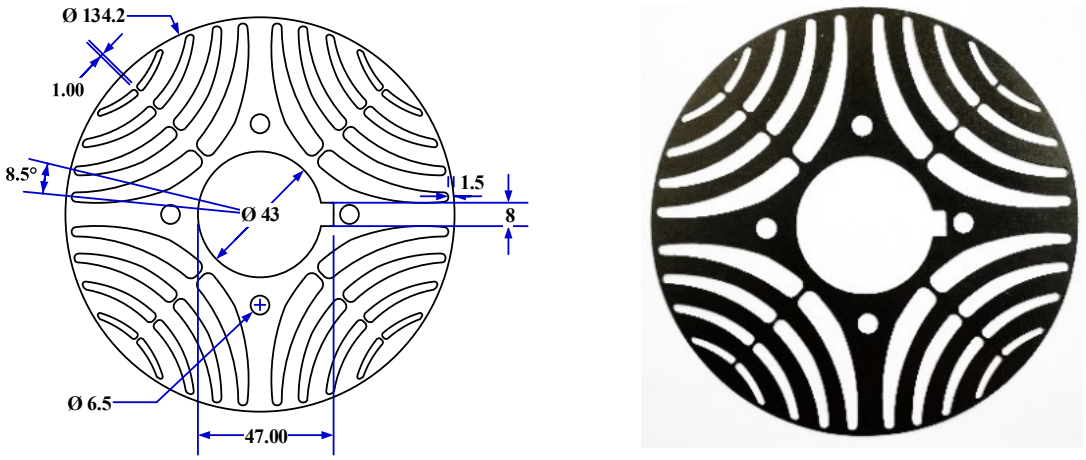

(a) (b)

Fig. 3-4. (a) Rotor dimension in mm for the rotor with α=8.5°. (b) Prototype rotor lamination with α=8.5°.

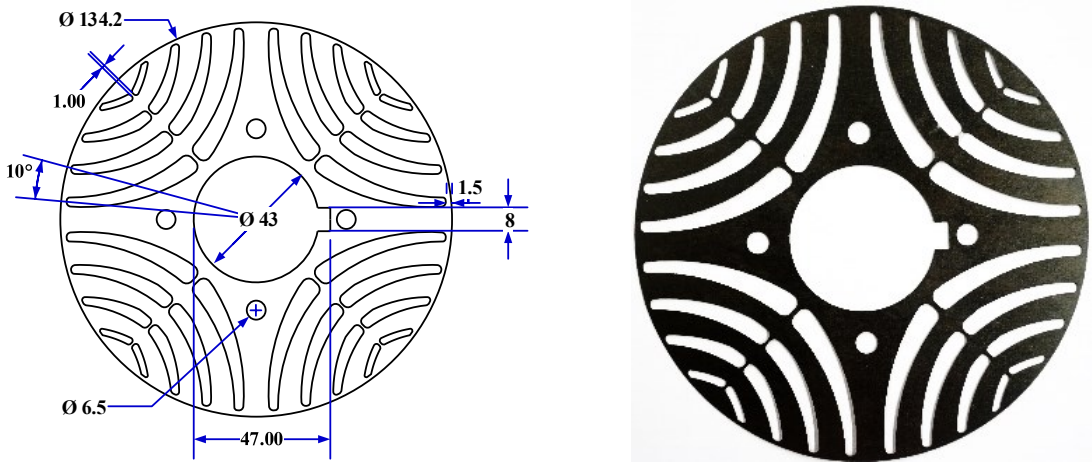

(a) (b)

Fig. 3-5. (a) Rotor dimension in mm for the rotor with α=10°. (b) Prototype rotor lamination with α=10°.

Fig. 3-6(a) and (b) depict the fabrication drawing with main dimensions of the segmented TLA CRGO rotor and its individual pole, respectively. In [45], an asymmetrical geometry of the single-pole lamination is described to simplify the rotor assembly process. In order to do so, as shown in Fig. 3-6(b), the width of the flux guide at the y-axis is increased by 2.5 mm, whereas

the width of the flux guide at *x*-axis is reduced by 2.5 mm while keeping the total width of the flux guide constant at 7.2 mm, as shown in Fig. 3-6(a). Furthermore, the barrier geometries are kept symmetrical with respect to the *q*-axis. The segmented pole lamination prototypes are shown in Fig. 3-6(c). As indicated in Fig. 3-6(b), two very small tabs are created on the surface of each pole. These tabs are used to indicate grain direction with respect to lamination geometry and to maintain lamination uniformity during the assembly process. In each segmented pole, a 3 mm × 8.4 mm key is created to interlock rotor laminations with the motor shaft as illustrated in Fig. 3-6(b). Moreover, in order to align and clamp rotor laminations, two 3.2 mm guided pin holes are created on the lamination of each pole, as shown in Fig. 3-6(b).

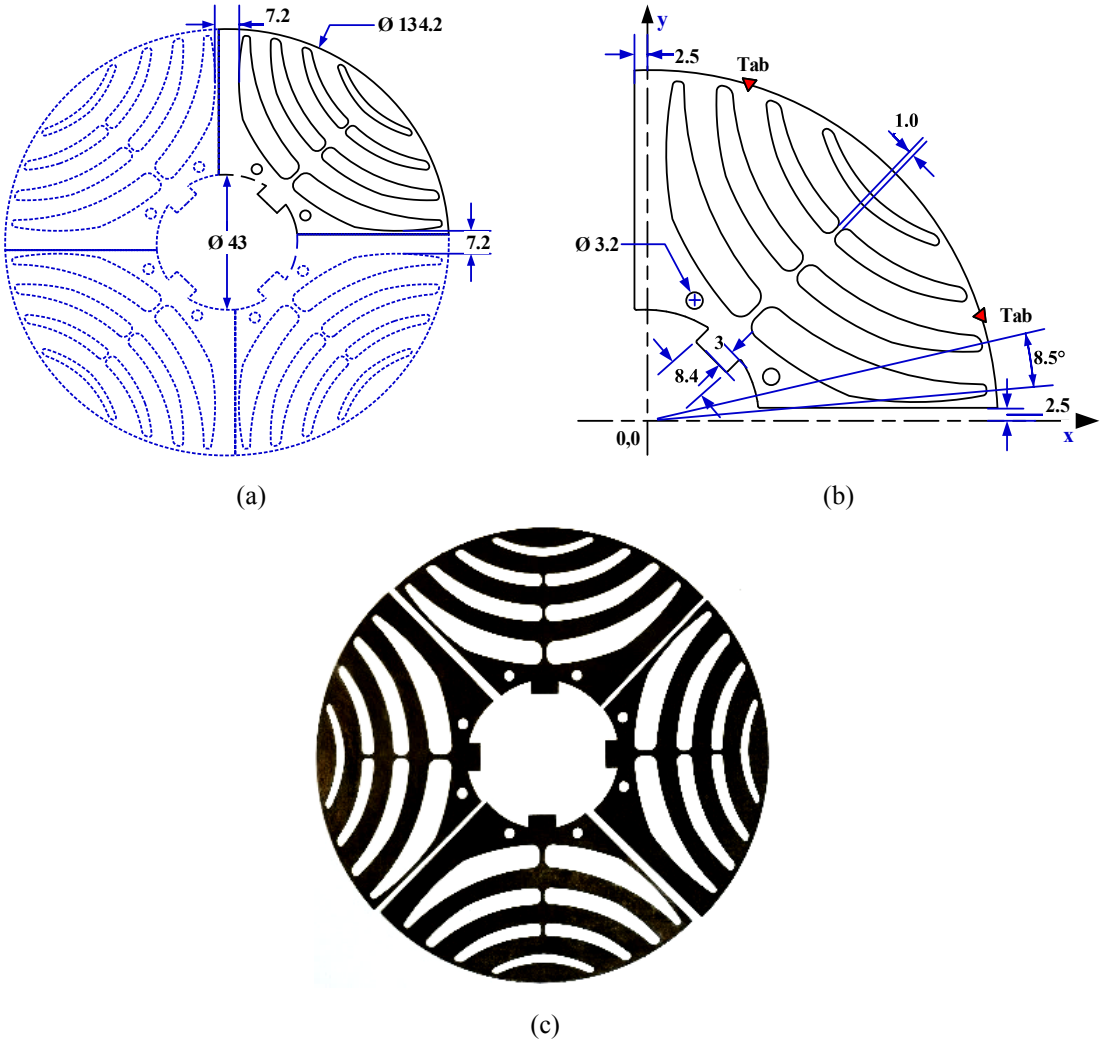

Fig. 3-6. (a) CRGO rotor dimensions in mm. (b) Single pole lamination dimensions in mm. (c) Four single pole CRGO lamination.

3.3 Lamination Cutting

The majority of today's electrical rotating machines are generally fabricated with thin steel laminations. Various methods exist to cut laminations. Dimensional accuracy, finishing of the edges, and magnetic properties of the laminations are greatly influenced by the method of manufacturing, as the cutting processes produce different stresses in the lamination. In addition, especially in the prototyping stage, the manufacturing cost is also a key factor in choosing a particular method of lamination cutting. The most extensively used techniques are die punching, laser cutting, and photochemical machining (PCM) [51]. In all three methods, an accuracy of ±0.0254 mm (25 μ) is achievable.

3.3.1 Die punching

In die punching, dies are fabricated according to the lamination shape and profile and are then used with a suitable mechanical or hydraulic press to remove the lamination out of an electrical steel sheet. A single or several laminations can be produced in each cycle. Laminations with burr-free edges and high-dimensional tolerances can be produced [52]. It is reported in [53] that the process of punching generates stresses at edges, which in turn alters the magnetic properties of the material leading to increased losses. Moreover, dies wear out after several operational hours, and then magnifying the above problem. Wearing out of the dies may also affect the dimensional accuracy of the laminations. In addition, to restore the magnetic properties in laminations, annealing is performed at high temperatures.

In the process of the die fabrication, the preliminary cost is high; however, the production cost is quite low. The estimated time to fabricate a die punch set to produce SynRM laminations is approximately six months. The average lamination production rate with a die punch and a power press machine is 50 laminations per minute. Hence, this makes the method more suitable for mass production. Once dies are fabricated, alterations to dies are difficult and expensive. This is another limitation of the die punching method, especially for prototyping.

3.3.2 Laser cutting

In laser cutting, a lamination can be produced without any contact of the work piece with a cutting tool or use of any kind of force. Almost any shape can be created without changing a tool. The lamination design is computerized and can easily be modified. The dimensional

accuracy is good, and the setup cost is moderate to low [52]. However, lamination edges experience high temperature stresses, which can cause permanent damage to the magnetic properties [54]. Additionally, a skilled manufacturer with precise apparatus for laser cutting is required in order to achieve high tolerances up to ±25 μ. During the initial development stages of the designed SynRM, the laser cutting is attempted. A fiber laser source manufactured by IPG photonics is used. The laser machine has an output power of 1 kW. The laser beam wavelength is 1070 ±10 nm, M^2 factor is <1.1 and oxygen is used as an assist gas. However, it is relatively difficult to laser cut a lamination having an insulation coating on the surface. During the initial trials, the required quality and the tolerances of laminations through laser cutting were not achieved. It is because the steel sheets came with a C5 coating, and during the cutting process, the laser damaged not only the coating but also the tangential and radial ribs of the rotor. Hence, laser cutting is difficult to be used for developing the SynRM rotors.

3.3.3 Photochemical machining

PCM, also known as photo etching and chemical milling, has many benefits for fabricating thin metal parts, which include enhanced accuracy, low-cost tooling, burr-free parts, economical prototyping, and higher production rate.

PCM is particularly advantageous in the prototyping phase, when various design variants can be produced and tested with little additional cost. In PCM, the cost of the phototool for a component is merely $200 to $300, as opposed to $10,000 to $50,000 to develop punching tools and dies [55]. In addition, alterations to existing designs can also be achieved at a low cost. Furthermore, PCM offers stress-free blanking of sheet metal without affecting the chemical or physical properties of the material. The traditional punching process can alter the magnetic and other physical properties. Moreover, the existing laser cutting process induces thermal stress and leaves a heat-affected zone on the metal parts. PCM can easily and economically reproduce complex geometries with ultrahigh resolutions. Photomachining is preferred for brittle, delicate, and sensitive materials, which might get damaged during the punching and laser cutting process. Hence, PCM is used to develop the designed SynRM stator and rotor laminations.

The PCM process starts with a flat piece of material and then the unwanted areas of the material are chemically etched away. Various stages of the PCM process are as follows:

1) **Cutting:** The metal sheets are cut to a specific dimension required by the machine size and also for the efficient use of the coating material, which reduces waste during the PCM process.

2) **Cleaning:** For proper adhesion between the sheet metal and the photoresist during the coating process, cleaning and removal of impurities from the metal sheet are performed using chemicals.

3) **Coating:** In the PCM process, the material should be coated with photoresist directly after cleaning. The coating is photosensitive and resistant to the etchant used to remove the material.

4) **Phototooling:** A photographically prepared film called a phototool is used to shield the material that is to remain after etching. The phototool is produced from a computer-aided design (CAD), sketch or blueprint file supplied by the designer. The phototool may contain one or many exact images of the desired part.

5) **Exposing:** In this stage of the PCM process, material with the photosensitive coating is exposed to ultraviolet (UV) light. This is a direct process that transfers the phototool image onto the coated material.

6) **Developing:** The material sheets must develop after exposing. The material is then sprayed or immersed with a developer. The run through the developer removes the unpolymerized areas of the image. After developing, the metal sheet is left with the images of the design protected by photoresist.

7) **Photo-etching:** During the photo-etching process, the material is sprayed or immersed with a chemical etchant. Any part of the material not protected by the photo resist is dissolved.

At the end, photochemical machined parts are removed from the protective coating of photoresist. Various stages of the PCM process used to produce SynRM rotor laminations are illustrated in Fig. 3-7. For the fabrication of the SynRMs discussed in this chapter, 500W UV light source is used. This light source is within the exposure machine. The wavelength of the UV lamp is between 350 and 400 nm. Sodium Carbonate is used as a photoresist developer. The Ferric Chloride solution is used as an etchant. The time to produce four pieces of SynRM's

laminations is approximately 20 minutes using two PCM machines. The stack length of the SynRM stator is 200 mm and the thickness of M15G29 steel is 0.36 mm. Hence, a total of 556 laminations are required, each for the stator and rotor stack. The total time to produce these stator and rotor laminations for one machine is around 92 hours.

Lamination sheet cutting and cleaning	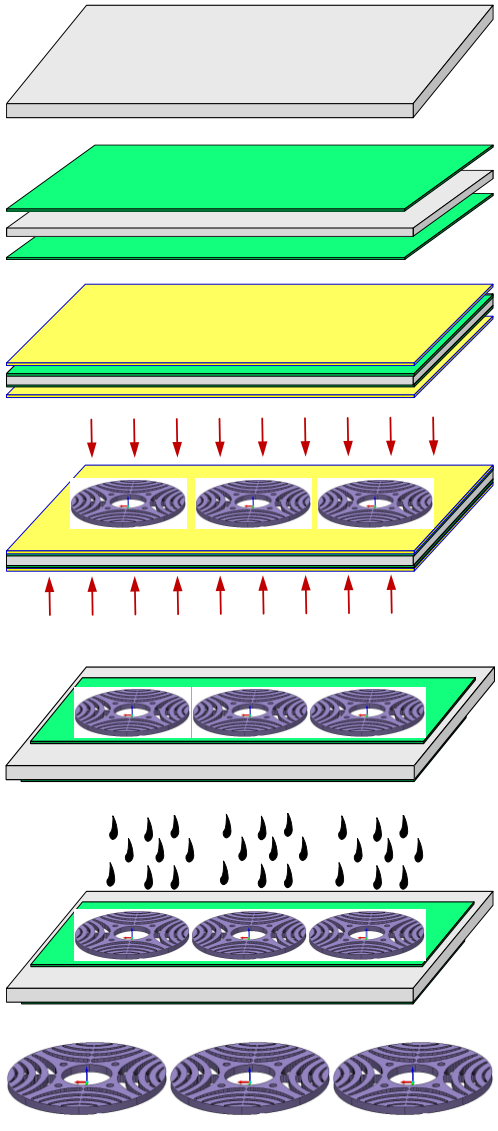
Coating with photoresist film	
Phototooling	
UV light exposing	
Developing	
Etching	
Final product	

Fig. 3-7. Photo chemical machining (PCM) process.

Although the PCM offers many advantages over die punching and laser cutting, the process requires skilled operator as well as the disposal and recycling of the etchant. The summary of

the advantages and disadvantages of die punching, laser cutting, and PCM are presented in Table 3-II.

Table 3-II Comparison of lamination cutting methods

Process	Advantages	Disadvantages
Die punching	• High production rate. • Single or multiple lamination can be produced. • Suitable only for mass production.	• High tooling and setup cost. • Design alternation is difficult and costly. • Wearing out of dies. • Stresses at cutting edge alter the magnetic properties of lamination. • Annealing is required to restore magnetic properties.
Laser cutting	• No tooling. Setup cost is moderate to low. • Design is computerized and easy to modify. • Economic for prototyping and small volume production.	• Require skilled operator and programmer. • Thermal stresses and heat-affected zones affect the magnetic properties of lamination. • Difficult to laser cut laminations having insulation coating. • Process is linear. Multiple parts cannot be created simultaneously.
PCM	• Low-cost tooling. • Stress and Burr free parts. • Does not affect properties of the material. • Multiple parts can be created simultaneously. • Economic for prototyping as well as for high volume production.	• Etchant disposal and recycling cost. • High skilled operator is required.

3.4 Assembly

In this section, different stages of stator and rotor assembly and specific components employed during assembly are presented.

3.4.1 Stator assembly

Lamination design is an electrical and mechanical consideration. For the complete stator assembly, a few important factors should be accounted for when designing laminations that directly affects the fabrication. Moreover, it is extremely important that stator and rotor cores are precisely stacked in the least amount of time. There are several lamination stacking methods such as welding, riveting, bolting, bonding, and cleat notch [51]. One of these methods is selected based on the motor being manufactured.

Welding is a well-known, inexpensive, and reliable method for stacking stator cores. In spite of several recent advancements in the welding technologies, it still has many disadvantages such as manual loading of the laminations, cleanup and polishing of welded parts in order to fit the stack in the frame, and a high level of maintenance [56]. Moreover, the welding process increases iron loss as it affects the magnetic properties of the laminations [57].

In riveting and bolting, holes are drilled on the lamination surface. The drilled holes decrease the effective cross sectional area of the lamination, which may affect the performance of the machine. Moreover, the heads of the rivets and bolts can be a hindrance for the winding end turns [51].

In bonding, the lamination stack is built by applying an adhesive on the laminations. Cores are then aligned on a fixture and heated to set the adhesive. The bonding method not only requires an oven to cure the bonding agents and a fixture for the assembled stack, but also the physical strength needed in large stacks is questionable.

In the cleat notch method, the cores are assembled by inserting a steel strip into every notch on the outer diameter (O.D) of the stator laminations. This method offers good dimensional stability with very little increase in core loss. The cleating strip steel is low cost and the process is fast. Also, cleating machines are very flexible and require minimal setup. Hence, the cleating notch method is used to stack and clamp the stator laminations for the prototyped SynRM stator. The configuration of cleat notch is for stacking in which the likeness of the notch should be

maintained for all laminations, irrespective of the stator size [58]. Depending on the size of the motor, the amount of notches may differ, ranging from 2 to 16 per stator. The position of the cleat notches should be in line with a slot opening or lamination tooth; however, alignment with a lamination tooth is preferable.

In the prototyped stator, six cleat notches are placed 60° apart and in line with the lamination tooth, as shown in Fig. 3-3(a) and Fig. 3-8, respectively. The enlarged view and dimensions of the cleat notch are shown in Fig. 3-9. The prototyped stator stack is installed in a NEMA 215T (IEC 132) cast iron frame using a hydraulic press. Fig. 3-10 shows the complete assembled and wound stator in the cast iron frame.

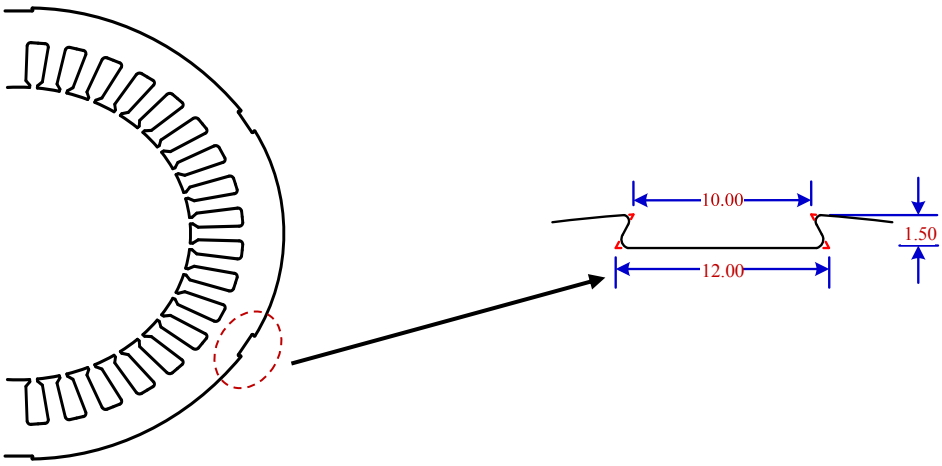

Fig. 3-8. SynRM machine stator lamination.

Fig. 3-9. Enlarged view of the cleat notch.

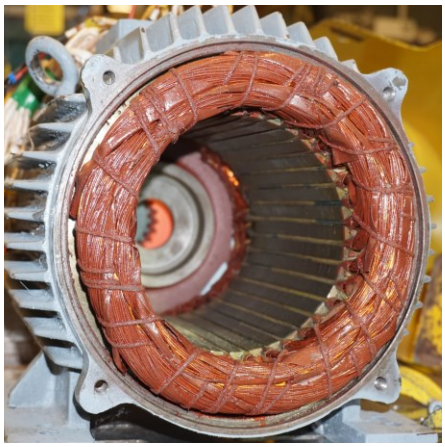

Fig. 3-10. Wound stator within a SynRM machine frame.

3.4.2 Rotor assembly

The assembly prototyped SynRM rotors shown in Fig. 3-4(a), Fig. 3-5(a), and Fig. 3-6(a) comprise of a shaft, rotor laminations, polyether ether ketone (PEEK) studs, Bakelite (Hylam) end plates, a lock nut, and bearings, as shown in Fig. 3-11, Fig. 3-13, and Fig. 3-16, respectively. The rotor shaft diameter and keyway size are selected according to IEC reference chart [59].

For the CRNGO rotors, the assembly process begins with the installation of a ϕ180 mm × 12 mm bakelite end plate on the nondrive end (NDE) of the shaft. A locking key is then inserted in the key way of the shaft. A detailed shaft drawing is presented in Fig. 3-11. A total of four M6 × 240 mm PEEK studs are then installed on the bakelite plate and locked by M6 PEEK nuts at NDE side. Rotor laminations are then installed one by one by aligning the lamination key way with the shaft key as well as PEEK studs and guided pin holes created between barriers. The complete CRNGO rotor stack is shown in Fig. 3-12.

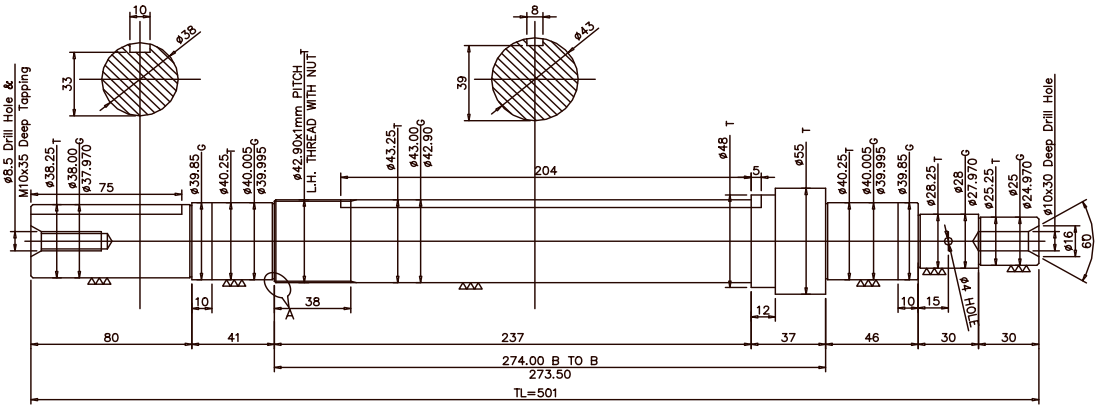

Fig. 3-11. CRNGO rotor shaft drawing.

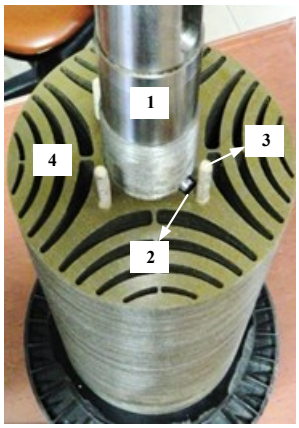

Fig. 3-12. CRNGO rotor assembly. (1) Rotor shaft. (2) Keyway. (3) PEEK stud. (4) Lamination.

To build a rotor stack from single-pole CRGO laminations, in [45], a lamination overlapping method is proposed. Due to the asymmetrical design of the single-pole laminations, it is possible to achieve an overlapping structure. As shown in Fig. 3-6(b), two 3.2 mm guided pin holes are created on each pole to align and clamp laminations. However, due to design errors, during the overlapping lamination stacking process, an offset/misalignment is observed between guided pin holes. Hence, as shown in Fig. 3-13, four M6 × 240 mm PEEK studs are installed on Bakelite plate and locked by M6 PEEK nuts at the NDE side of the shaft. A special shaft (spline) with four keyways is fabricated to install the segmented pole laminations. A detailed shaft drawing is presented in Fig. 3-14. The CRGO rotor assembly begins with making the first layer of laminations by positioning four segmented poles through PEEK studs in the shaft key slot, as shown in Fig. 3-13. The second layer is placed on top of the first layer by flipping every single-pole lamination around the *q*-axis by 180°, and this process continues until the last layer.

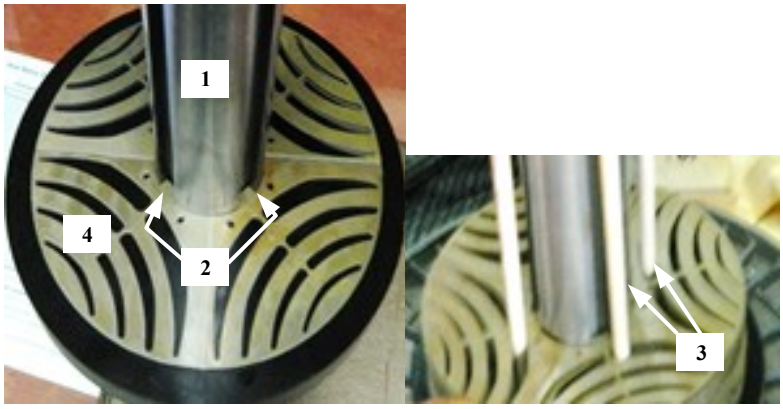

Fig. 3-13. CRGO rotor assembly. (1) Rotor shaft. (2) Keyways. (3) PEE studs. (4) Single pole lamination.

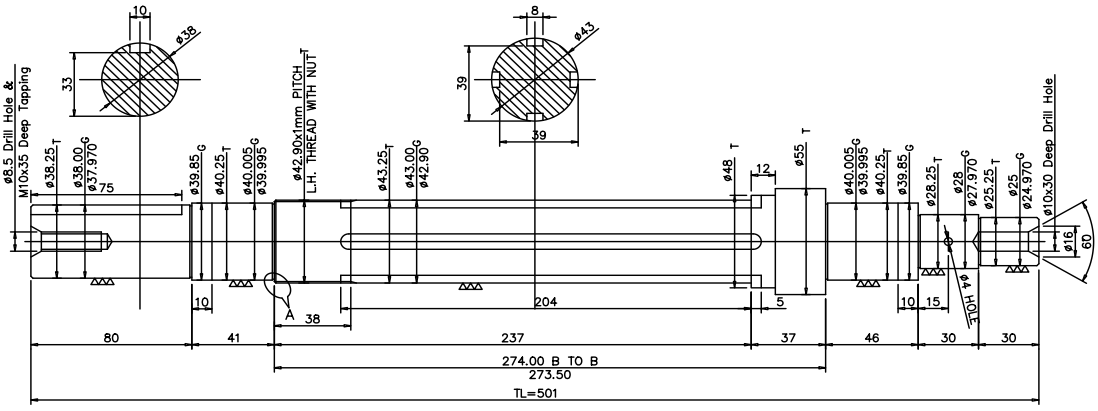

Fig. 3-14. CRGO rotor shaft drawing.

PEEK is a nonconductive and nonmagnetic organic thermoplastic material with high temperature withstand capability [60]. The Bakelite (Hylam) grade P1 according to IS: 2036-1995 [61] is used for the end plates. This is due to its good insulation properties, mechanical and impact strength, high dielectric strength, light weight, ease of machining, and excellent tensile strength.

In order to enhance the robustness of the rotor, the flux barriers of all three rotors are filled with epoxy resin. Fig. 3-15 shows the epoxy-filled CRNGO rotor. Fire retardant (FR) polyester epoxy resin of an electrical grade is used. The curing is achieved at a room temperature by adding a catalyst and an accelerator. The organic peroxide is used as a catalyst and an accelerator is based on a cobalt. The catalyst and accelerators are used in proportion of 5% each of the total weight of the resin. After the epoxy settled down, in all three rotors, the second ϕ180 mm × 12 mm bakelite end plate is installed on the drive end (DE) side of the laminated core through PEEK studs and is fixed using M6 nuts. A metal nut is then installed on the DE side of the rotor, in order to couple the laminated core and the end plates with each other. Rotors are then taken for O.D turning to obtain a uniform airgap of 0.4 mm. A total of one 6208-2z bearing is then installed on the DE and the NDE side. For a 6208-2z bearing, the maximum permissible r/min is 10,000, the maximum dynamic load capacity is 22.35 kN, and it can work up to the maximum temperature of 250 °C, which is good enough for the static and dynamic testing as well as the operation of the designed SynRM. The tolerance of ±0.015 mm (15 μ) is maintained during the entire manufacturing and assembly of the various components of the machine.

Fig. 3-15. Epoxy filled rotor.

Rotor dynamic balancing is then accomplished. Balancing is performed on SCHENCK RoTec dynamic balancing machine, model no. H10BK+CAB 610. The Balancing is executed at 1000 r/min and in three stages. In the first stage, only the rotor shafts are balanced. In the second stage, the assembled rotors are balanced without bearings, and in the third stage, the assembled rotors are balanced with bearings. The final rotor prototype is depicted in Fig. 3-16.

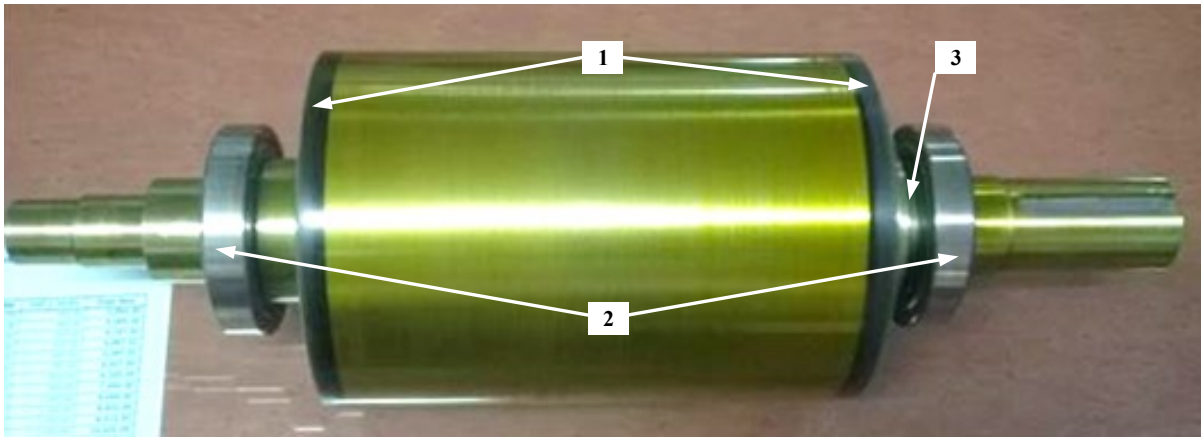

Fig. 3-16. Complete prototyped rotor. (1) Bakelite (Hylam) plates. (2) Bearings. (3) Lock nut.

3.5 Summary

In this chapter, the fabrication and assembly process of SynRM machines proposed in [50] were presented. To validate the sizing methodology proposed in [38] as well as the method to reduce torque ripple in TLA SynRM rotors and the novel TLA segmented CRGO rotor geometry proposed in [49], one stator, two designs of TLA CRNGO rotors with different rotor slot pitch (α), and one segmented pole CRGO rotor were investigated and prototyped. Three different lamination cutting methods were presented. The application of a nontraditional PCM process to develop SynRM motor laminations was described. In addition, stator and rotor assembly processes, rotor balancing procedure, as well as specific components utilized in fabrication were presented. The tolerance of ±0.015 mm (15μ) was maintained during the entire manufacturing and assembly of the various components of the machine.

Chapter 4 Characterization of Synchronous Reluctance Machines

In this chapter, in order to validate the accuracy of the design and fabrication, characterization of three synchronous reluctance machines (SynRMs) described in Chapter 3 is presented. This comprises the static torque-angle characterization, inductance characterization, and dynamic characterization of the prototyped SynRMs. The SynRM designs of Fig. 3-4 (rotor with α = 8.5° and β = 10°) and Fig. 3-5 (rotor with α = 10° and β = 10°) are also analyzed in three different machine design softwares, MotorSolve, MagNet, and MagneForce, respectively. Due to the limitations of the design software, it is not possible to include CRGO material characteristics in the design software. Hence, only experimental characterization results for the SynRM CRGO rotor shown in Fig. 3-6 are included. A special regenerative dynamometer test setup is developed in order to perform the dynamics tests.

4.1 Introduction

In the SynRM, the electromagnetic torque is generated due to the interaction between the stator magnetomotive force (MMF) and rotor saliency. From Fig. 4-1, various equations of the electromagnetic torque can be obtained using (4-1) to (4-3) [39, 62]. It is clear from (4-1) to (4-3) that at a particular voltage and operating speed, the developed torque in the SynRM reaches its maximum at a specific current or torque angle (δ) and it also depends on the saliency ratio (ζ). From Fig. 4-1 and (4-1) to (4-3) the relation between load and current angles is derived as (4-4).

$$T_e = \frac{3}{2}\frac{P}{2}\left[\left(L_d - L_q\right) i_d i_q\right] \tag{4-1}$$

$$T_e = \frac{3}{2}\frac{P}{2}\left[\left(L_d - L_q\right) I_s^2 \sin 2\delta\right] \tag{4-2}$$

$$T_e = \frac{3}{2}\frac{P}{2}\left[\left(\zeta - 1\right)\left(\frac{E_m}{\omega L_d}\right)^2 \sin 2\delta\right] \tag{4-3}$$

$$\theta = \tan^{-1}(\zeta \tan \delta) \tag{4-4}$$

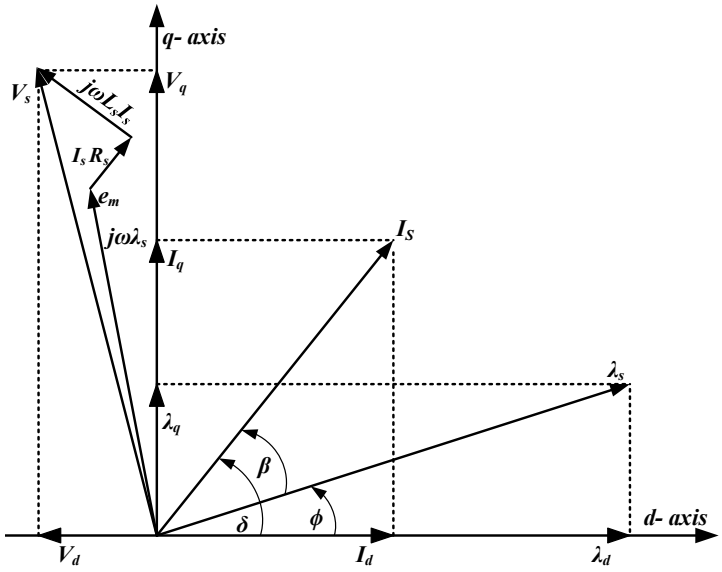

Fig. 4-1. Synchronous reluctance machine (SynRM) phasor diagram.

The maximum torque can be obtained analytically by differentiating (4-2) [19]. However, the obtained analytical solution assumes that the machine inductances and flux linkages are constant, whereas the actual parameters depend on the stator current and the angle (δ). Therefore, it is more accurate to obtain the maximum torque and angle relationship using the FEA simulations. Hence, various FEA simulations are first performed at different magnitudes and angles of the stator phase current in three different FEA softwares as mentioned in Chapter 1. Fig. 4-2(a) and (b), Fig. 4-3(a) and (b), as well as Fig. 4-4(a) and (b) present the geometry and the *d*-axis flux plot of the designed SynRM rotor of Fig. 3-4 (rotor with $\alpha = 8.5°$ and $\beta = 10°$) in MotorSolve, MagNet, and MagneForce, respectively.

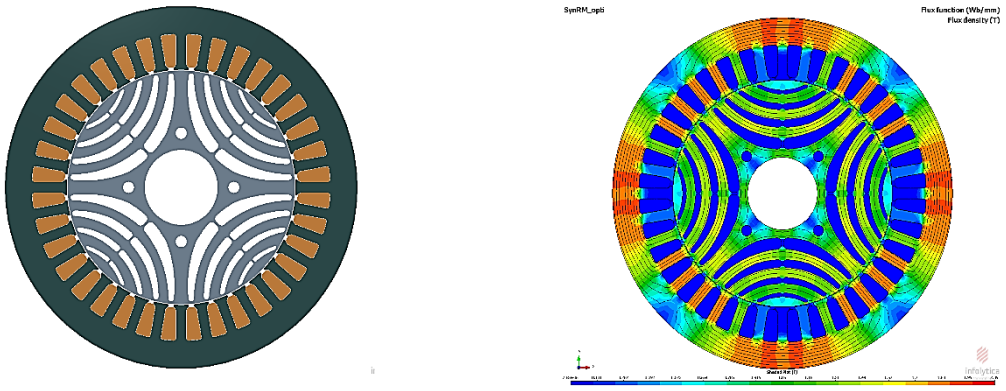

(a) (b)

Fig. 4-2. SynRM model in MotorSolve (a) Geometry. (b) *d*-axis flux plot.

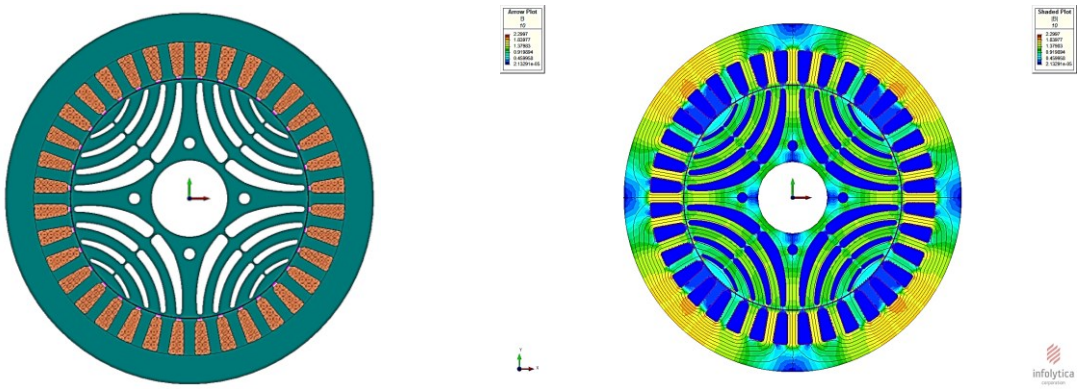

(a) (b)

Fig. 4-3. SynRM model in MagNet (a) Geometry. (b) *d*-axis flux plot.

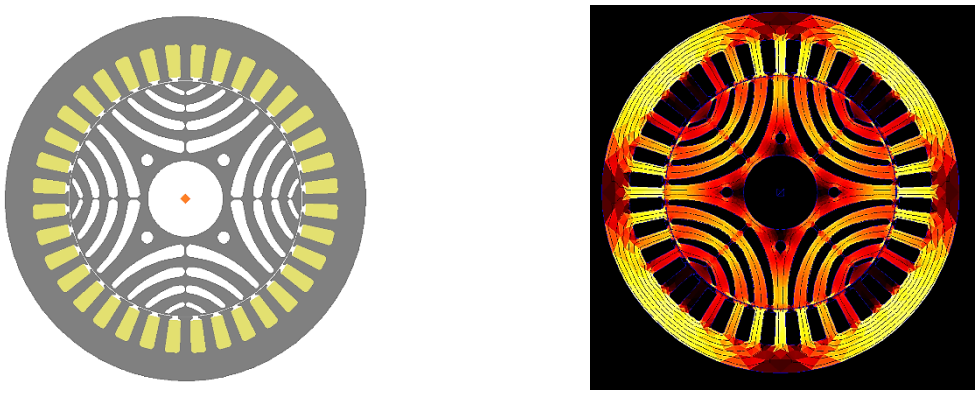

(a) (b)

Fig. 4-4. SynRM model in MagneForce (a) Geometry. (b) *d*-axis flux plot.

Torque-angle curves are first simulated in the design software. As discussed in section 2.3.3, in MotorSolve, the static torque curves can only be obtained by a varying current angle (δ), and during a simulation run, the rotor is stationary and aligned at the *d*-axis. In MagNet and MagneForce, the static torque curves can be generated by changing the current angle (δ) and keeping the rotor stationary as well as by varying the rotor position and keeping the current angle fixed. In the design software, an alternating current source is connected to the machine, when the torque curves are obtained by a varying current angle (δ). When the static torque curves are obtained by changing rotor position, a dc source is connected to the motor where phase A of the machine is connected to the positive and phase B and phase C are connected to the negative terminal of the dc source. It is also possible to generate torque-angle curves as a function of both the current angle and the rotor position. However, this is beyond the scope of the research work.

4.2 Static torque-angle characterization

The prototyped SynRM is controlled using a vector controlled inverter. In the design of the control scheme, an important consideration is the current angle (δ). In practice, the real characteristics of a SynRM rarely match the ideal characteristics. Owing to the inductance levels of the motor winding, the commutation induces a phase lag and deviations from the ideal sine-wave current [16]. These non-ideal characteristics reduce the torque-to-ampere ratio. Hence, in the vector controlled drive, the current angle (δ) is selected to regulate current vectors at optimal values. As the δ can be controlled by the inverter, an appropriate value of δ can improve the torque-to-current ratio and provide an optimal motor operation [17, 18].

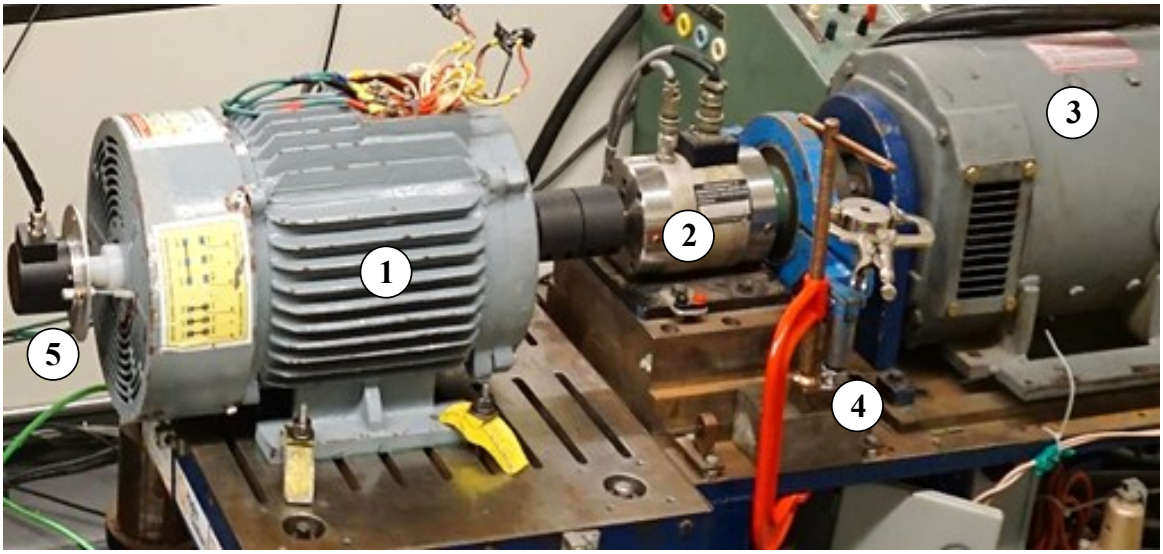

Fig. 4-5. SynRM machine test setup. (1) Prototype. (2) Torque transducer. (3) dc machine. (4) Mechanical clamp. (5) Encoder.

In order to verify the accuracy of design and fabrication, the prototyped rotors of Fig. 3-4, Fig. 3-5, and Fig. 3-6 are tested. Fig. 4-5 shows the test setup for the SynRM machine. The test setup comprises a SynRM prototype, a dc machine, a torque transducer, a dc power source, a position encoder, a data acquisition unit, a voltage source inverter (VSI), and a real time system. The SynRM is coupled to a torque transducer. Various static tests are performed on the prototyped machine. In order to obtain the static torque at different currents and rotor positions, the prototyped SynRM with the rotor in Fig. 3-4 with $\alpha = 8.5°$ and $\beta = 10°$ is initially locked at the *d*-axis of the rotor on the test bench. As shown in Fig. 4-5, a mechanical clamp is used to lock the rotor at different positions. A fixed dc current is then supplied to the SynRM. The value

of the supplied dc current is increased from 2A to 18 A in steps of 2 A. At each current level the resultant torque is recorded from a torque transducer. The output torque for various currents is obtained at every 5° electrical (2.5° mechanical) from *d*-axis to *q*-axis of the rotor. A similar method is followed to measure the output torque of the prototype SynRM rotor in Fig. 3-5 with identical rotor and stator slot pitch ($\alpha = \beta = 10°$) and the CRGO rotor in Fig. 3-6. The measurement schematic of the SynRM torque-angle characterization by varying rotor position is shown in Fig. 4-6.

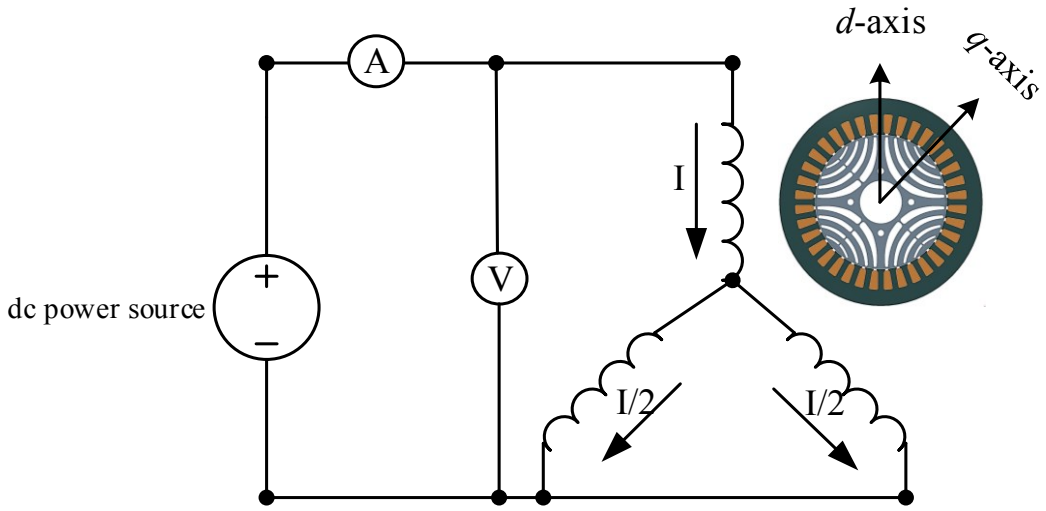

Fig. 4-6. Schematic of SynRM torque-angle characterization by varying rotor position.

A method described in [20] is used to obtain the torque curves by varying the current angle (δ). For the prototyped machines, when static torque curves are obtained by varying the current angle, the rotor *d*-axis is first aligned with the stator phase A-axis. The rotor shaft is then locked at the *d*-axis on the test bench as shown in Fig. 4-5. From the VSI, three phase ac currents are then applied from 1.414 A rms to 9.9 A rms in steps of 1.414 A rms. The torque angle is varied by varying the angle of the current vector from 0° to 90°. The output torque is recorded for each current magnitude and current angle. Fig. 4-7 represents the measurement schematic of the SynRM torque-angle characterization by the varying current angle.

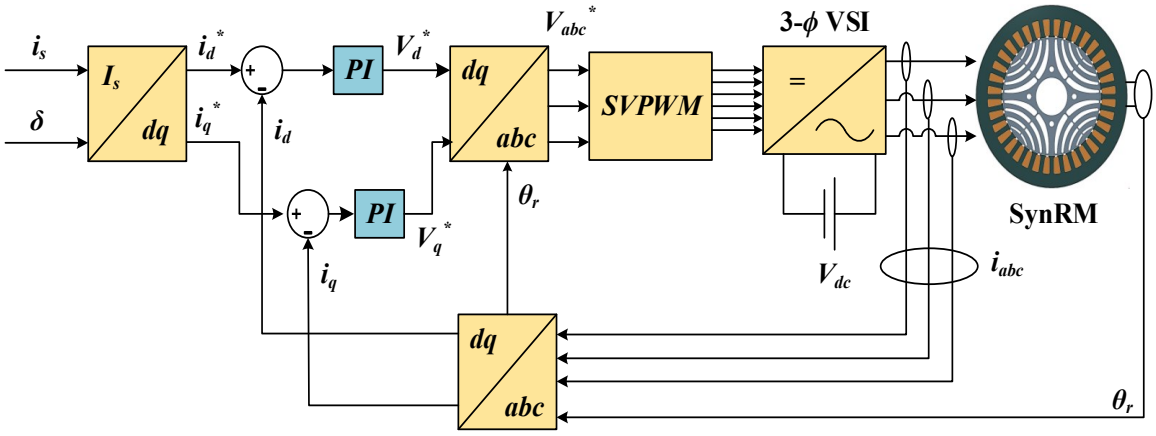

Fig. 4-7. Schematic of the test setup of the SynRM torque-angle characterization by varying current angle.

Fig. 4-8, Fig. 4-9, and Fig. 4-10 present the measured static torque curves obtained for different currents by varying rotor positions and current angles. The torque-angle curves for the SynRM rotor design in Fig. 3-4 with $\alpha = 8.5°$, $\beta = 10°$ are shown in Fig. 4-8(a) and (b). For the rotor design in Fig. 3-5 with $\alpha = \beta = 10°$ the torque curves are presented in Fig. 4-9(a) and (b). The measured torque-angle curves for the CRGO rotor in Fig. 3-6 with $\alpha = 8°$, $\beta = 10°$ are depicted in Fig. 4-10. The torque-angle curves obtained by varying rotor positions are presented for the peak stator currents of 4 A, 10 A, and 16 A, respectively, with 16 A being the maximum phase peak current which is a line current of 19.59 A rms. The torque-angle curves obtained by varying the current angle are presented for the peak stator currents of 4 A, 8 A, and 12 A, respectively, with 12 A being the maximum phase peak current which is a line current of 14.7 A rms. In addition, the experimental results also have an error band around the measurements. This error band includes the tolerance and resolution of the torque transducer and conditioner.

The value of the peak torque for the rotor in Fig. 3-4, Fig. 3-5, and Fig. 3-6 is 52.45 Nm, 65.6 Nm, and 52.5 Nm, respectively. Results show a good correlation with the designed value of the peak torque of 60 Nm listed in Table 3-I. This is due to the tight tolerances (±0.015 mm) maintained during the fabrication and assembly process. It can be seen from experimental results that the maximum torque occurs between the rotor positions of around 45° and 50° electrical degree which is 22.5° and 25° mechanical degrees. This information is useful for the design of speed and torque controllers.

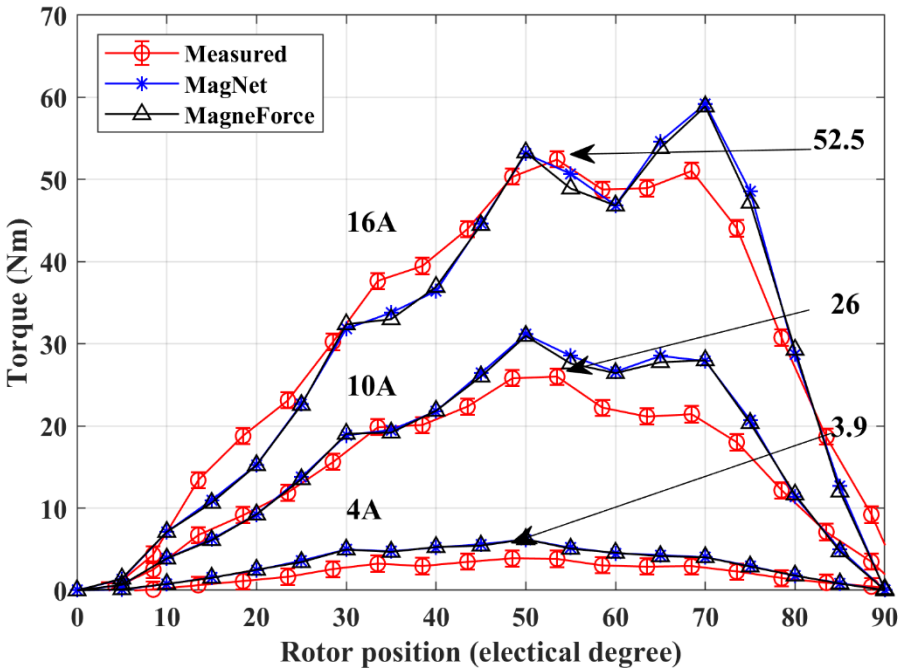

(a)

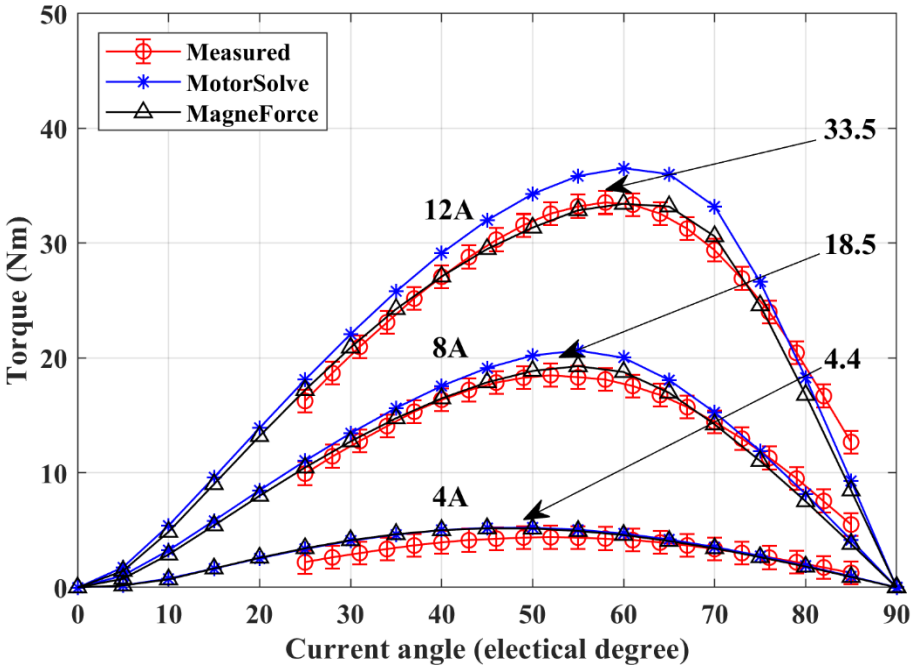

(b)

Fig. 4-8. Comparison of torque-angle curves for the SynRM rotor with α = 8.5°, β = 10°. (a) Measured and simulated torque-angle curves by varying rotor position. (b) Measured and simulated torque-angle curves by varying current advance angle.

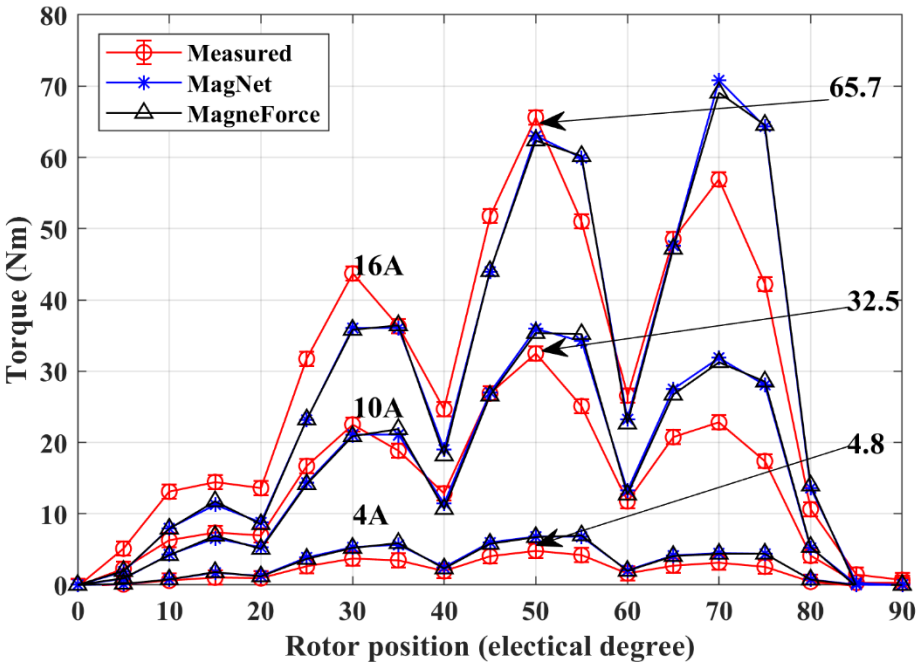

(a)

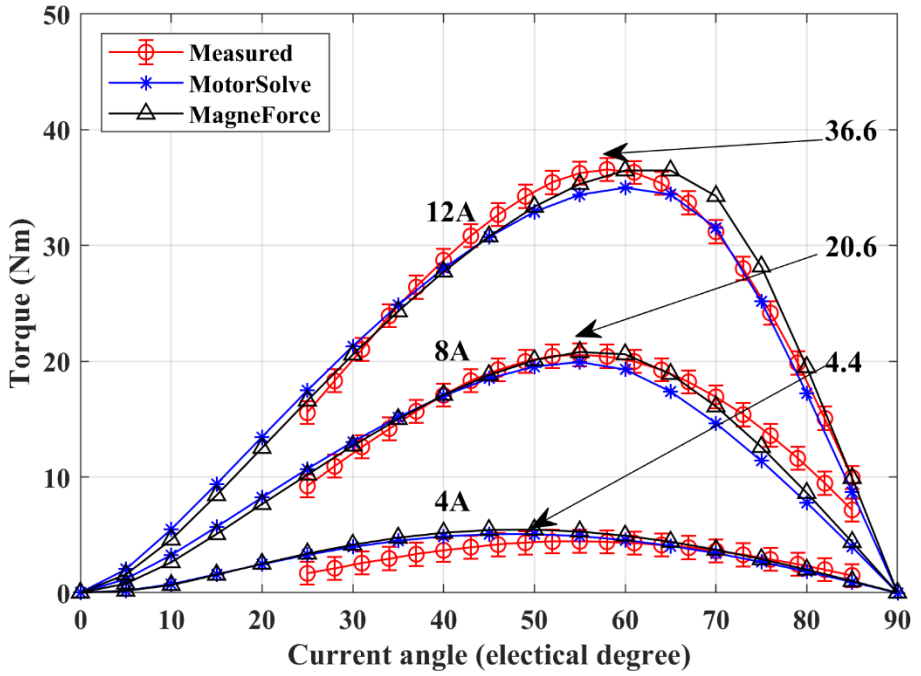

(b)

Fig. 4-9. Comparison of torque-angle curves for the SynRM rotor with α = 10°, β = 10°. (a) Measured and simulated torque-angle curves by varying rotor position. (b) Measured and simulated curves torque-angle by varying current advance angle.

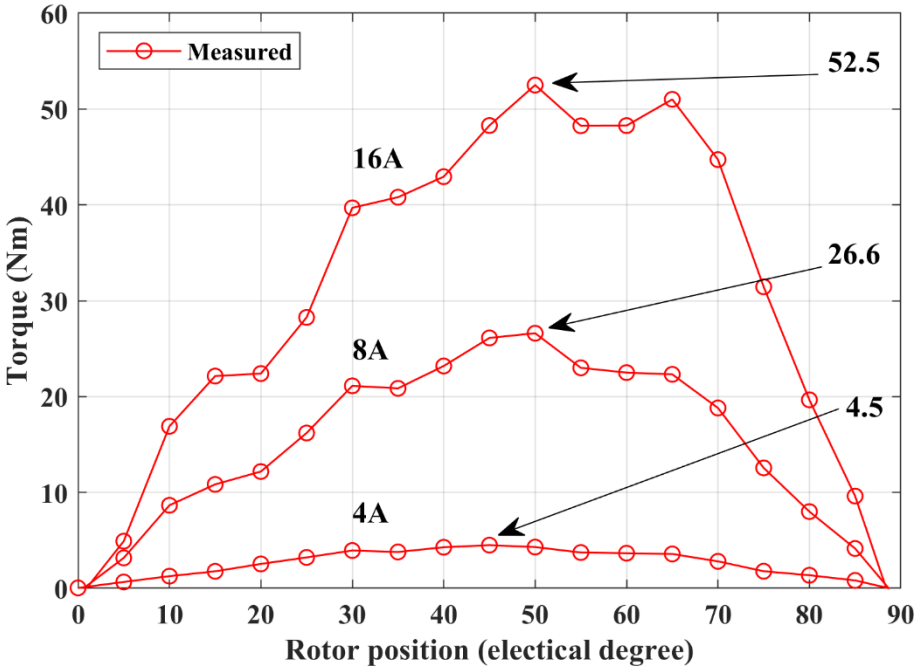

(a)

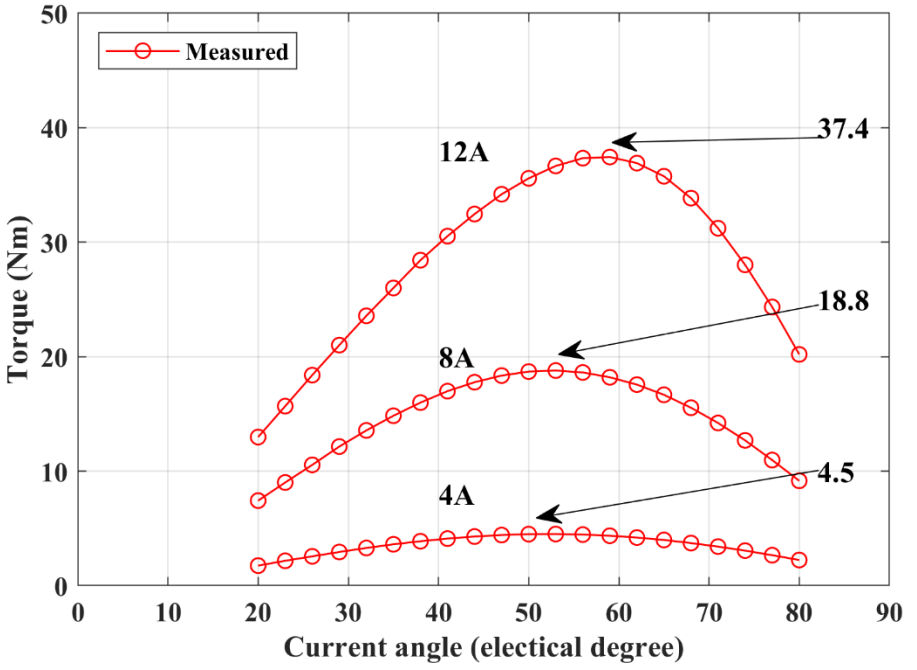

(b)

Fig. 4-10. Comparison of torque-angle curves for the CRGO SynRM rotor with α = 8.5°, β = 10°. (a) Measured torque-angle curves by varying rotor position. (b) Measured torque-angle curves by varying current advance angle.

For the rotor design in Fig. 3-5, the stator and rotor slot pitches are alike ($\alpha = \beta = 10°$), and at every 10° mechanical (20° electrical) all rotor slots face the stator slots. Hence, when the rotor rotates, a large variation in the inductance occurs at every 10° mechanical (20° electrical). It causes a considerable pulsation in the output torque due to stator and rotor slots mutual effect. This is also apparent from the torque-angle curves of Fig. 4-9(a) that at every 10° mechanical (20° electrical), the torque varies from the local minimum value to local maximum value. For the CRNGO rotor design in Fig. 3-4 and the CRGO rotor design in Fig. 3-6, the rotor and the stator slot pitches are nonidentical. Therefore, the variation of the inductance with respect to the rotor position is not as significant, due to which the torque pulsation decreases. This can be determined from the torque-angle curves in Fig. 4-8(a) and Fig. 4-10(a).

It is observed from Fig. 4-8(b), Fig. 4-9(b), and Fig. 4-10(b) that the torque curves obtained by changing the current angle do not include the effects of the slot and the space harmonics. The torque curves generated by varying rotor positions contain both the slot and space harmonic effects. This information is quite useful for drives engineers to decide on the bandwidth of the controllers. Although the magnitude of torque curves obtained against the current angle matches with experiments, it is advantageous to obtain the torque curves against the rotor positions from the drive perspective. Furthermore, the simulated torque curves obtained by varying the rotor position and current angle are within the error band of the experimental results. This proves the accuracy of the software to simulate the machine design in detail.

4.3 Inductance characterization

An accurate characterization of the direct-axis (d-axis) inductance (L_d) and quadrature-axis (q-axis) inductance (L_q) is required in the design and operation of the vector controlled drive as the drive's controller parameters are heavily dependent on the inductance values. The inductance characterization of the designed SynRMs is first analyzed in the design software. The three phase flux linkages λ_a, λ_b, and λ_c are required to obtain the d-axis flux linkage (λ_d) and q-axis flux linkage (λ_q), which are then used to find the L_d and L_q. In MagneForce, λ_a, λ_b, and λ_c are not directly available. Hence first, the winding's self-inductances (L_{aa}, L_{bb}, L_{cc}) and mutual inductances (L_{ab}, $L_{ac,}$ L_{ba}, L_{bc}, L_{ca}, L_{cb}) are obtained from the field explorer panel at the d-axis and q-axis, respectively. The flux linkages λ_a, λ_b, and λ_b are then calculated using (4-5). In MotorSolve and MagNet, the flux linkages λ_a, λ_b, and λ_b are directly obtained at the d-axis and

q-axis, respectively. The value of the λ_d , λ_q, $L_{d,}$ and L_q are then calculated using (4-6) and (4-7). Alternatively, (4-8) can also be used to calculate L_d and L_q. The saliency ratio is calculated using (4-9). For the designed SynRMs, L_d and L_q are obtained for the phase current of 1A rms to 14 A rms. In (4-7), i_a, i_b, and i_c are the peak value of current in phase A, B, and C, respectively. In (4-8), $i_{d,q}$ is the peak value of phase A current (i_a).

$$\begin{bmatrix}\lambda_a\\ \lambda_b\\ \lambda_c\end{bmatrix} = \begin{bmatrix}L_{aa} & L_{ab} & L_{ac}\\ L_{ba} & L_{bb} & L_{bc}\\ L_{ca} & L_{cb} & L_{cc}\end{bmatrix}\begin{bmatrix}i_a\\ i_b\\ i_b\end{bmatrix} \tag{4-5}$$

$$\lambda_d, \lambda_q = \frac{2}{3}(\lambda_a - 0.5\lambda_b - 0.5\lambda_c) \tag{4-6}$$

$$L_d, L_q = \left(\frac{\lambda_a - 0.5\lambda_b - 0.5\lambda_c}{i_a - 0.5i_b - 0.5i_b}\right) \times 1000 \tag{4-7}$$

$$L_d, L_q = \frac{2}{3}\left(\frac{\lambda_a - 0.5\lambda_b - 0.5\lambda_c}{i_{d,q}}\right) \times 1000 \tag{4-8}$$

$$\zeta = \frac{L_d}{L_q} \tag{4-9}$$

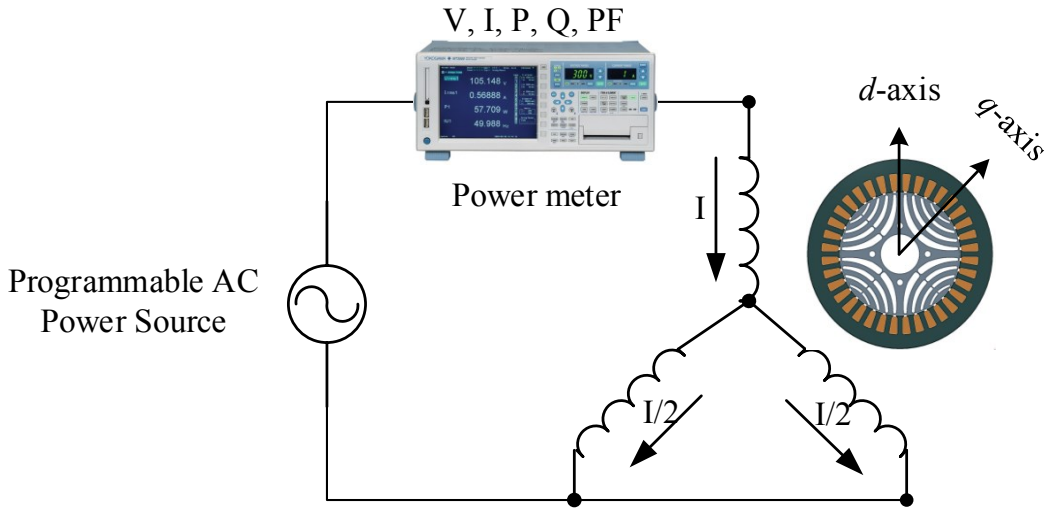

Fig. 4-11. Schematic of SynRM inductance characterization test setup.

For the inductance measurement of the prototyped SynRMs, the same test setup of Fig. 4-5 is used. The *d* and *q* axes inductances are measured using the ac standstill test according to IEEE 1812™-2014 [63]. The AMETEK® MX-30-3-pi programmable ac power source and YOKOGAWA WT300 high precision power meter are employed during the inductance measurement. In this test, ac currents of the desired magnitude and frequency are supplied to the phase winding of the machine while the rotor is locked at *d*-axis or *q*-axis. The schematic of the inductance measurement is shown in Fig. 4-11. For each current magnitude, the rms values of the phase voltage, current, and reactive power are recorded in the power meter. Using (4-10) and (4-11), the value of the *d* and *q* axes inductances are calculated, where X is the phase reactance, V is the rms value of the applied voltage, Q is the measured reactive power, f is the frequency of the applied voltage, L_d is the *d*-axis inductance, and L_q is the *q*-axis inductance, respectively. The saliency of the machine is calculated using (4-9). The design speed of the prototyped SynRMs is 850 rpm (28.33 Hz). Moreover, for the prototyped SynRMs, due to high values of inductances, a higher supply voltage is required to apply the rated current in the phase windings. Hence, for the prototyped SynRMs, the inductance measurements are carried out at the supply frequency of 17 Hz in order to apply the rated current within the maximum voltage limit of the ac power source. The inductances are obtained for the current of 1 A rms to 14 A rms.

$$X = \frac{V^2}{Q}\,(\Omega) \tag{4-10}$$

$$L_d, L_q = \frac{2}{3}\frac{X}{(2\pi f)} \times 1000\ (mH) \tag{4-11}$$

Fig. 4-12, Fig. 4-13, and Fig. 4-14 compare the simulated and measured inductances as well as the saliency. The comparison presents an acceptable agreement between the simulated and experimental data. It is discussed in Chapter 3 that the SynRM rotors of Fig. 3-4 and Fig. 3-5 are fabricated with M15G29 CRNGO steel. In order to enhance the performance of the SynRM in terms of a higher saliency ratio, efficiency, and torque density the SynRM rotor of Fig. 3-6 is fabricated with M5 CRGO steel. The CRNGO material possesses uniform magnetic and electric characteristics throughout its surface. The CRGO steel presents superior magnetic characteristics along the rolling direction, whereas the magnetic permeability is lower than the

CRNGO steel when the magnetic field is applied perpendicular to the rolling direction. Hence, the lower permeability of the CRGO steel reduces *q*-axis inductance. Fig. 4-15 compares the measured inductance and the saliency of the SynRM rotors. It is evident from Fig. 4-15 that the *q*-axis inductance of the CRGO SynRM reduces significantly between 1 A and 7 A. However, from 8 A to 14 A, the inductance is almost the same as CRNGO rotors, as the magnetic permeability of the CRGO and CRNGO steel is not significantly different at higher currents.

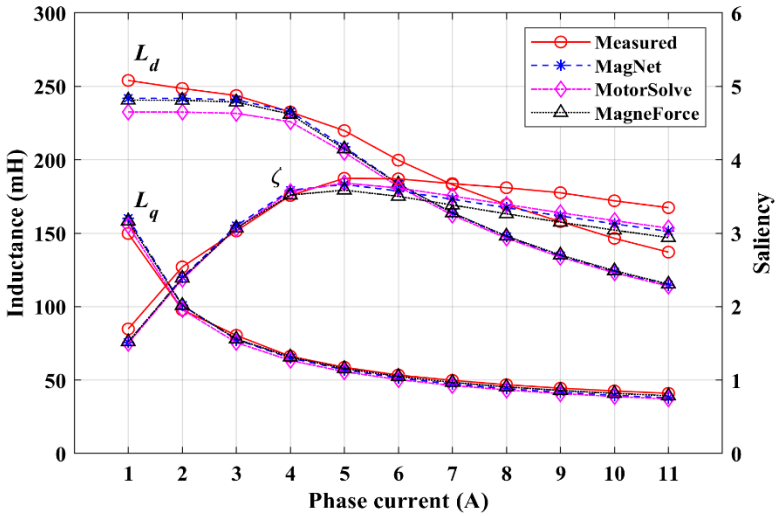

Fig. 4-12. Comparison of the measured and simulated inductance and saliency for the SynRM rotor with α=10°, β=10°.

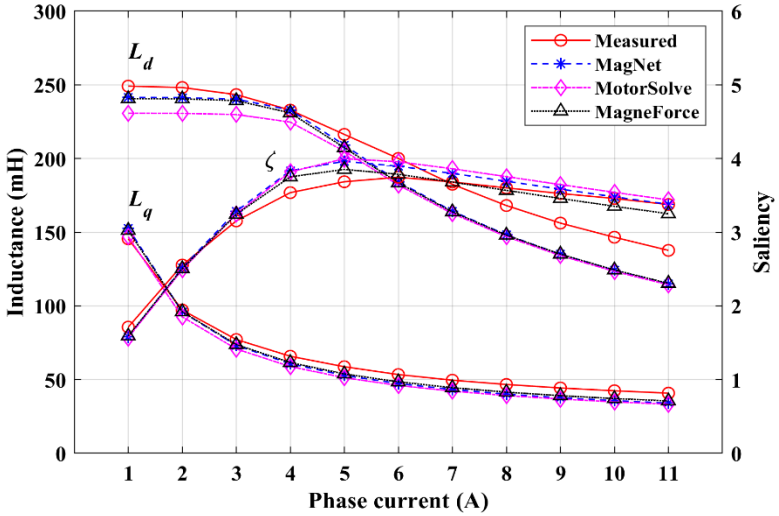

Fig. 4-13. Comparison of the measured and simulated inductance and saliency for the SynRM rotor with α=8.5°, β=10°.

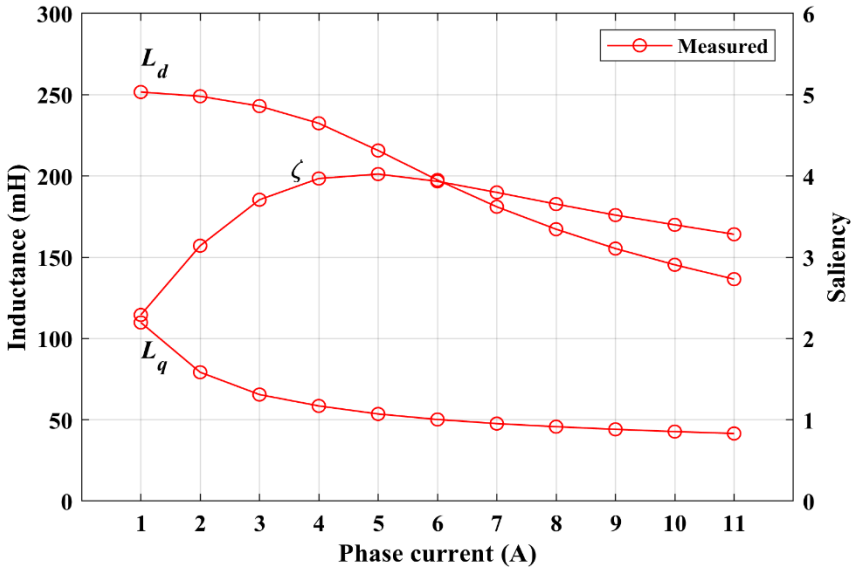

Fig. 4-14. Measured inductance and saliency for the SynRM CRGO rotor with α=8.5°, β=10°.

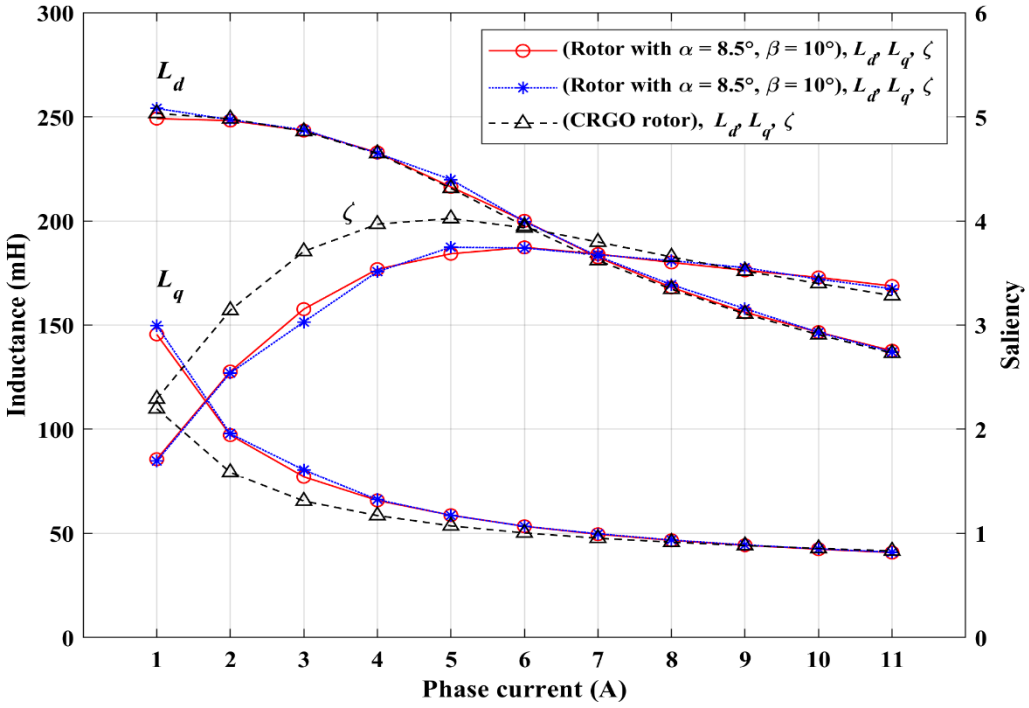

Fig. 4-15. Comparison of the measured inductances and saliency for the SynRM rotors.

4.4 Dynamic characterization

The dynamic characteristics of the prototyped SynRMs are also analyzed. A special regenerative dynamometer test setup is developed in order to perform dynamics tests. Fig. 4-16 shows the schematic representation of the test setup. The test setup and equipment are illustrated in Fig. 4-17.

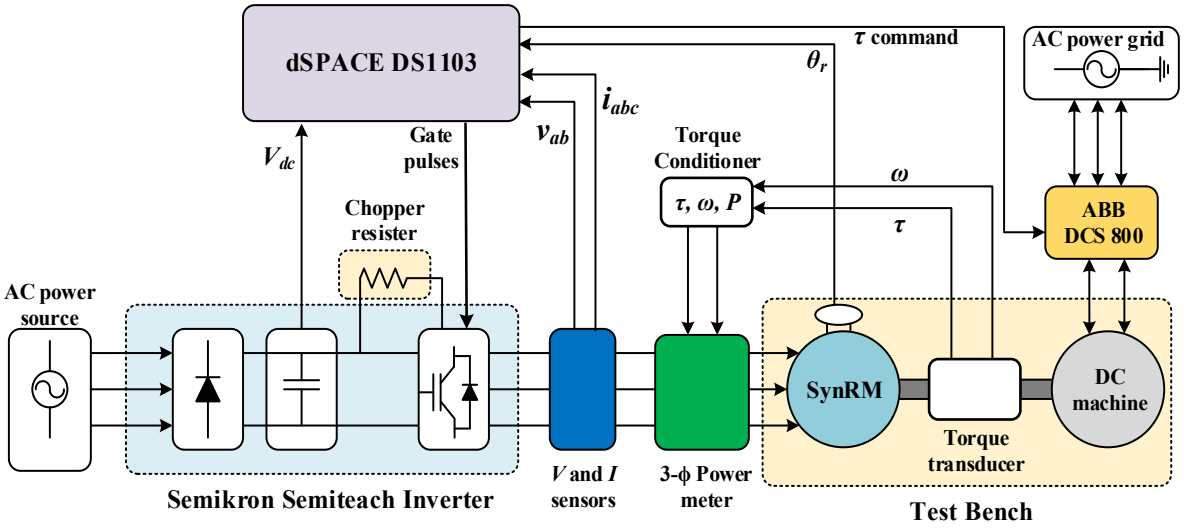

Fig. 4-16. Schematic of SynRM dynamic characterization.

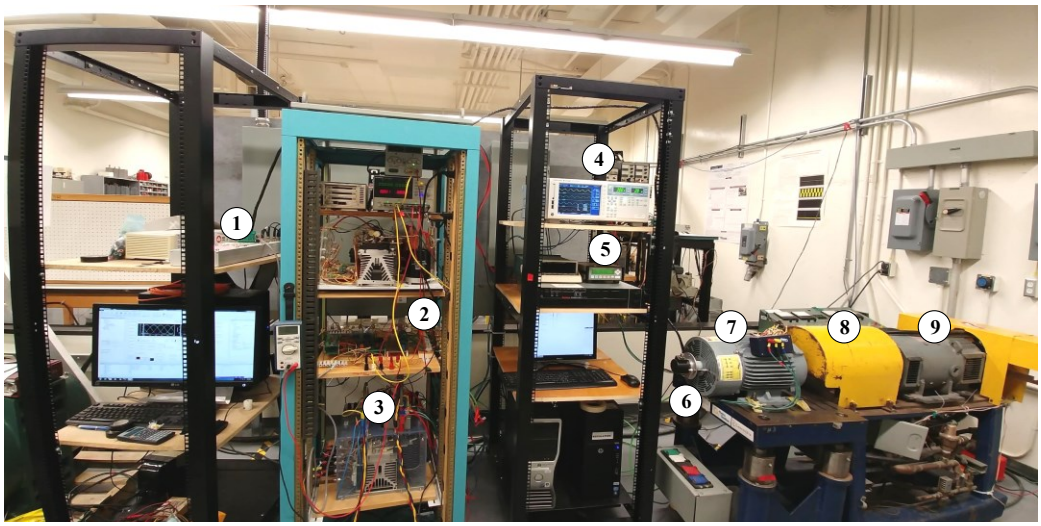

Fig. 4-17. Experimental setup for SynRM dynamic characterization. (1) dSPACE DS1103 real-time controller. (2) Current and voltage sensors. (3) Inverter. (4) Power meter. (5) Torque conditioner. (6) Encoder. (7) Prototype SynRM. (8) Torque transducer. (9) DC machine.

The test setup consists of an AMETEK® MX-30-3-pi programmable ac power source, which is connected to the three phase diode rectifier input of the SEMIKRON SEMITEACH inverter. A dc-link capacitor connects the rectifier to the three-phase inverter. The three-phase two-level inverter system installed with insulated-gate bipolar transistors (IGBTs) is rated for 50 A and 1200 V. A braking chopper is also included in the inverter circuit. A resistance bank is connected with the chopper for the deceleration and the negative torque tests. The inverter feeds the SynRM through LEM LA 100-P current sensors. The inverter output and dc-link voltages are measured using voltage sensors LEM LV 20-P and LEM LV 100. A YOKOGAWA WT3000 high precision power meter is connected between the inverter and motor terminals for the measurement of various electrical quantities. The prototyped SynRM is connected to the dc dynamometer through a S. Himmelstein MCRT® 2930T torque transducer. The output of the torque transducer is connected to a torque conditioner for the measurement of the shaft torque, speed, and power. The torque and speed outputs of the torque conditioner are also connected to the power meter for the efficiency measurement. The dc dynamometer is connected to the grid via a 4-Q ABB DCS-800 regenerative drive. The SynRM control scheme is implemented in the dSPACE DS1103 real-time controller using MATLAB-Simulink. A 12-bit position encoder (model#925 B-S-4096-CCW-SG-21-N-PP-N) from Encoder Product Company (EPC) is installed on the NDE side of the prototyped SynRM. The encoder output is connected to the digital I/O of DS1103 board. Inverter gating pulses are generated from the slave I/O of DS1103 board. A sampling time (T_s) of 25μs and the switching frequency (f_s) of 8 kHz are used for all dynamic measurements. The maximum current capacity of the 4-Q ABB DCS-800 regenerative drive is 25 A. Hence, for the prototyped SynRMs, the maximum applied load torque (T_L) is limited to 16 Nm, where the corresponding line current (I_L) is 9.8 A rms ($\hat{I}_s$ = 8 A).

4.4.1 Optimal current vector control

The optimal current vector trajectory is investigated for the maximum torque per ampere (MTPA) control. It can be seen from Fig. 4-8, Fig. 4-9, and Fig. 4-10 that at low current magnitudes, the current angle (δ) at which the torque per current becomes a maximum is around 45°, where the d and q axes currents are equal ($i_d = i_q$). At high current magnitudes, the saturation in the steel is considerable. Hence, the MTPA point moves away from δ = 45° to a

higher value of δ. Fig. 4.18 illustrates the measured τ versus δ curves for the SynRM rotor in Fig. 3-4 for the peak phase current of 4 A to 14 A. The red square points highlight the maximum torque to current ratio. The corresponding δ is used to determine the MTPA trajectory.

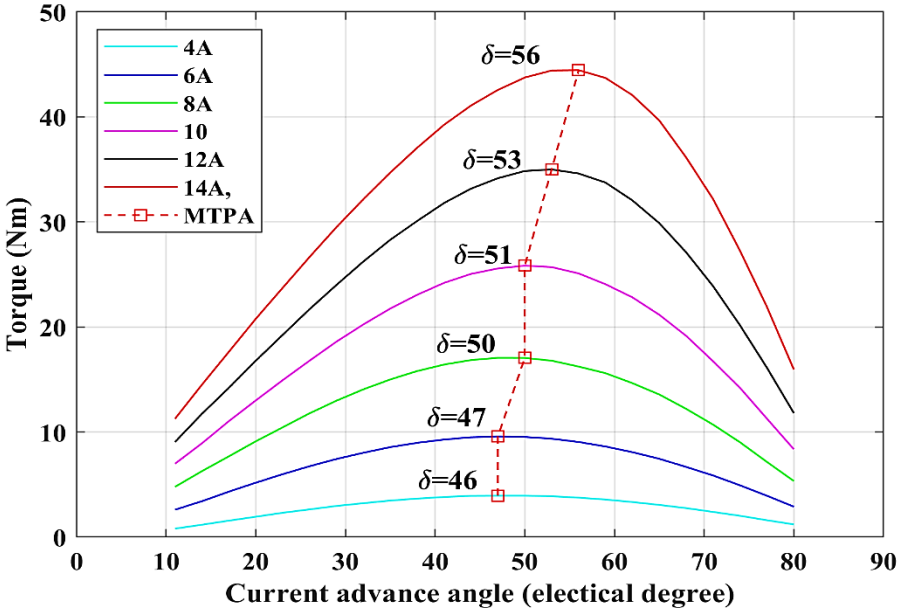

Fig. 4-18. Measured torque versus current angle for MTPA.

4.4.2 Torque and mechanical power versus speed

The torque and mechanical power versus speed curves are essential for appropriate comparison of electrical machines under similar operating conditions. The torque-speed curves are usually characterized by the rated torque, rated power, and base speed of the machine. These curves also represent the torque production capability of the machine as well as the speed (base speed) that can be attained before the point where the output torque needs to be decreased during the field weakening operation in order to maintain a constant output power. For the prototyped SynRM rotors, the torque-speed curves are obtained using MTPA control at I_L = 9.8 A rms ($\hat{I}_s$ = 8 A). Fig. 4-19, Fig. 4-20, and Fig. 4-21 represent the measured and simulated torque-speed curve of the prototyped SynRM rotors. For the prototyped SynRM rotor with α = 8.5°, β = 10°, the measured torque-speed curve has an acceptable agreement with the simulated torque-speed curve as illustrated in Fig. 4-19. Moreover, it is possible to attain the maximum speed of 2100 rpm (2.47 times the base speed) using MTPA control. On the other hand, for the prototyped SynRM rotor with α = 10°, β = 10°, due to high torque ripple

produced by the rotor geometry, it is difficult to control the machine over the wide torque-speed envelope. Hence, the torque-speed curve is obtained up to the speed of 1200 rpm as shown in Fig. 4-20. For the SynRM CRGO rotor, it is possible to attain the maximum speed of 2450 rpm (2.88 times the base speed) using MTPA control. Fig. 4-22 compares the measured torque-speed of the prototyped SynRMs. It is evident from Fig. 4-22 that the SynRM CRGO rotor possesses a wider torque-speed envelope and higher torque capability for the same operating conditions.

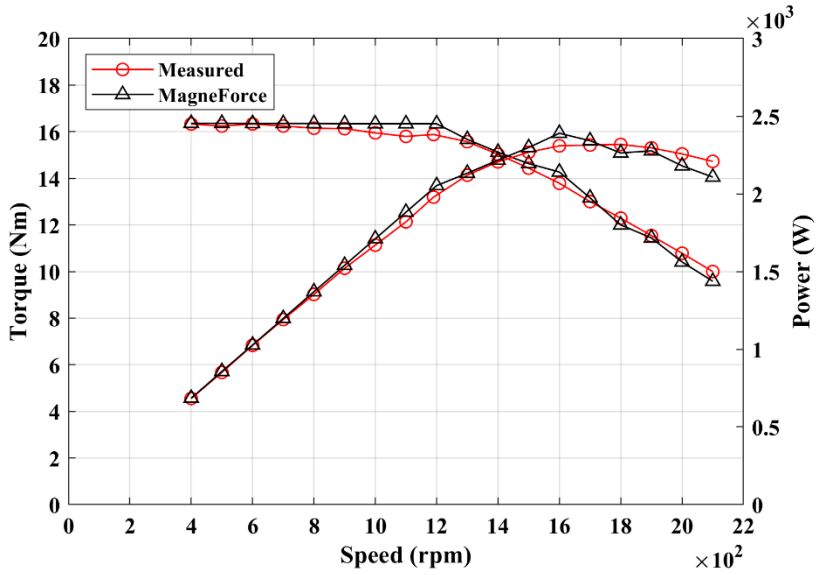

Fig. 4-19. Torque and shaft power versus speed of the SynRM rotor with α=8.5°, β=10°.

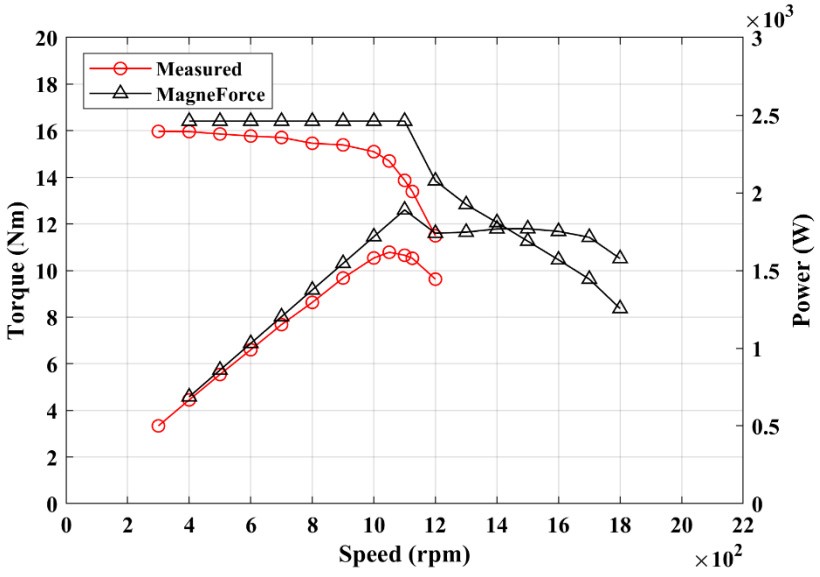

Fig. 4-20. Torque and shaft power versus speed of the SynRM rotor with α = 10°, β = 10°.

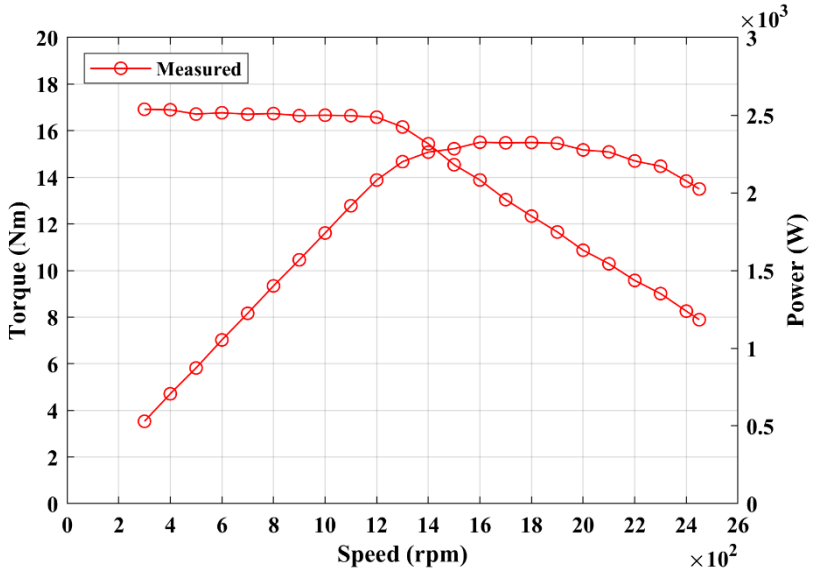

Fig. 4-21. Torque and shaft power versus speed of the SynRM CRGO rotor.

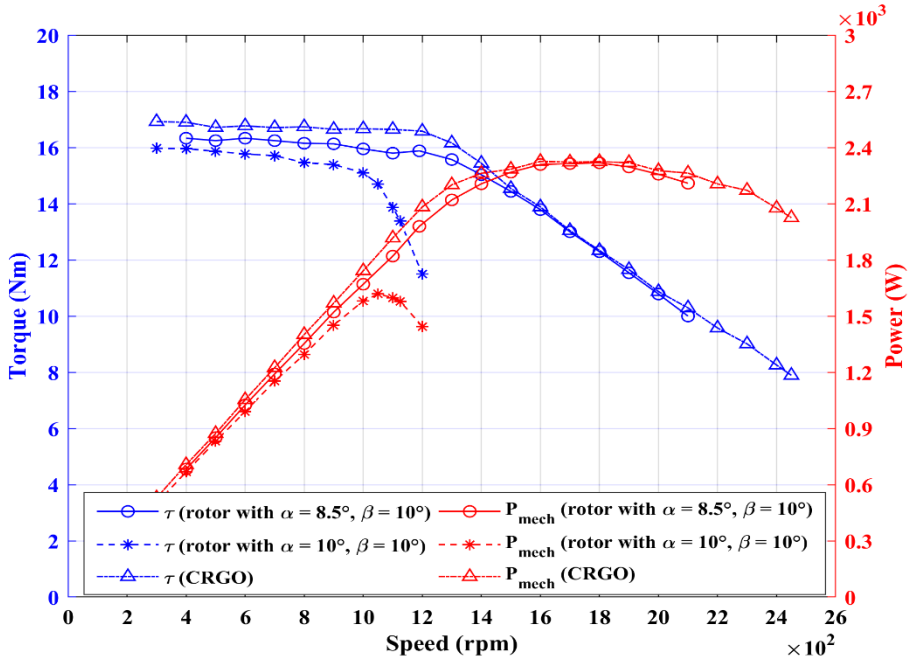

Fig. 4-22. Comparison of the measured torque and shaft power versus speed of the SynRM rotors.

4.4.3 Power factor and efficiency versus speed

In addition to the torque-speed characterization, the power factor (PF) characterization of a machine is very essential as it represents the ratio of the motor power and volt-ampere (VA) rating of an inverter. A machine with low PF requires an inverter with higher VA rating when

compared to a machine with a high PF. Fig. 4-23 represents the measured PF characteristics for the prototyped SynRMs. The PF characteristics are obtained for the torque-speed envelope presented in Fig. 4-22. For the prototyped SynRM rotors with $\alpha = 8.5°$, $\beta = 10°$, and the CRGO, the PF is almost constant up to the base speed of 1200 rpm. When the speed is higher than the base speed, the PF increases and reaches a relative maximum value. For the rotor with $\alpha = 8.5°$, $\beta = 10°$, the maximum PF is 0.66 at 1700 rpm and $\delta = 65°$, whereas for CRGO rotor the maximum PF is 0.68 at 1700 rpm and $\delta = 65°$. This information is substantial to calculate the inverter VA rating. Beyond this point, the PF decreases due to the flux weakening operation of the machine. It is apparent from Fig. 4-23 that the PF of the CRGO rotor is higher than the other rotors and this is due to the enhanced saliency of the rotor. Hence, the SynRM with CRGO rotor would require a lower VA rated inverter compared to the other two rotors. The difference in power factor is not very noticeable as the measurements are carried at 50% of the rated condition of the machine. Nevertheless, it would be significant at full load. Fig. 4-23 also shows the measured efficiency obtained along the torque-speed envelope at the optimal current vector trajectory. Between the base speed (1200 rpm) and the maximum one, the efficiency is above 90%. The maximum efficiency over the torque-speed envelope for the rotors is 96%.

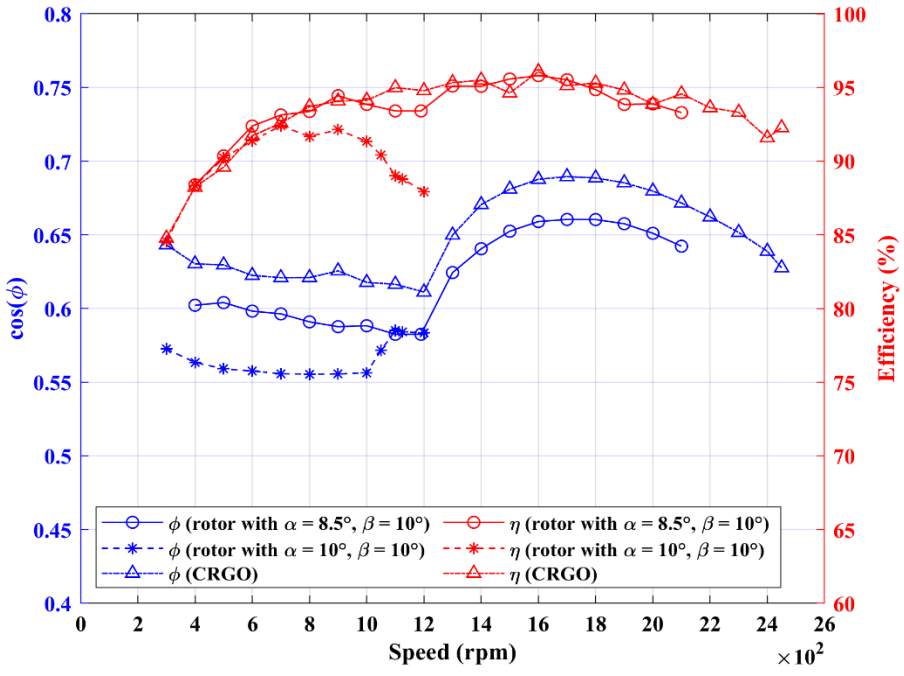

Fig. 4-23. Measured power factor and efficiency versus speed.

4.4.4 Steady-state torque

Fig. 4-24, Fig. 4-25, and Fig. 4-26 present the simulated and measured steady-state torque for the prototyped SynRMs for the load torque of 16 Nm and 8 Nm, respectively. The load torque of 16 Nm and 8 Nm is applied to the machine at 800 rpm, and the corresponding amplitude of the line currents (I_L) are 9.9 A rms ($\hat{I}_s$ = 8 A) and 6.8 A rms ($\hat{I}_s$ = 5.55 A), respectively. Table 4-I and Table 4-II compare the average torque obtained from the measurements and simulations. The comparison presents an acceptable agreement between the simulated and measured torques. As discussed in section 4.2, the SynRM rotor with similar slot pitches (α = 10°, β = 10°) produces higher torque ripple than the rotor with nonidentical rotor and stator slot pitches. It is also observed from Fig. 4-24 and Fig. 4-25 that the steady state torque of the SynRM rotor with α = 10°, β = 10° obtained from simulations has higher torque ripple. However, due to the bandwidth limitation of the torque transducer, it is not possible to capture the torque ripple of the prototyped SynRMs during measurements.

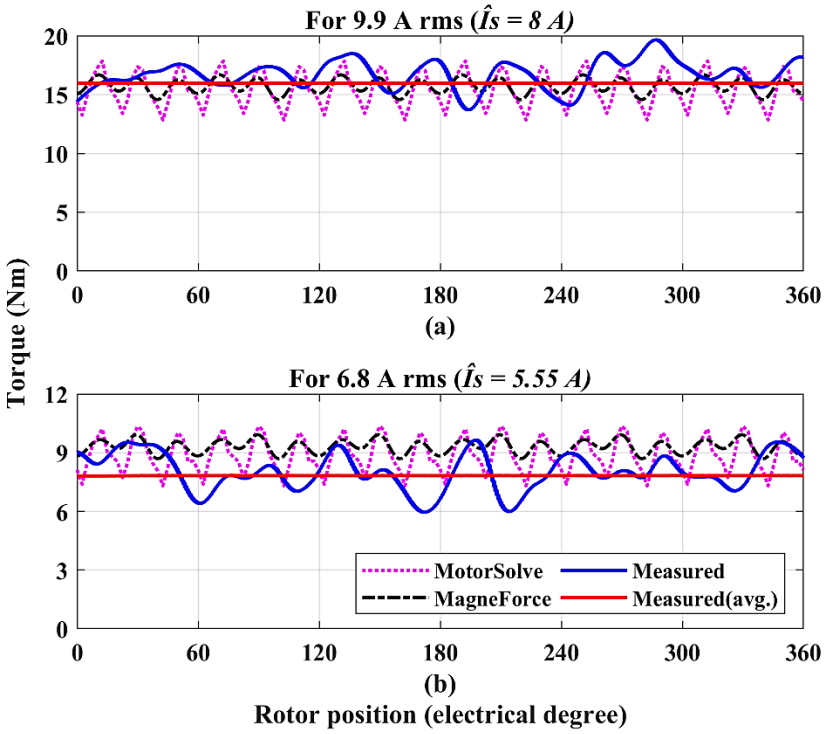

Fig. 4-24. Steady state torque for SynRM with α = 8.5°, β = 10° at 800 rpm. (a) T_L = 16 Nm at I_L = 9.9 A rms ($\hat{I}_s$ = 8 A). (b) T_L = 8 Nm at I_L = 6.8 A rms ($\hat{I}_s$ = 5.55 A).

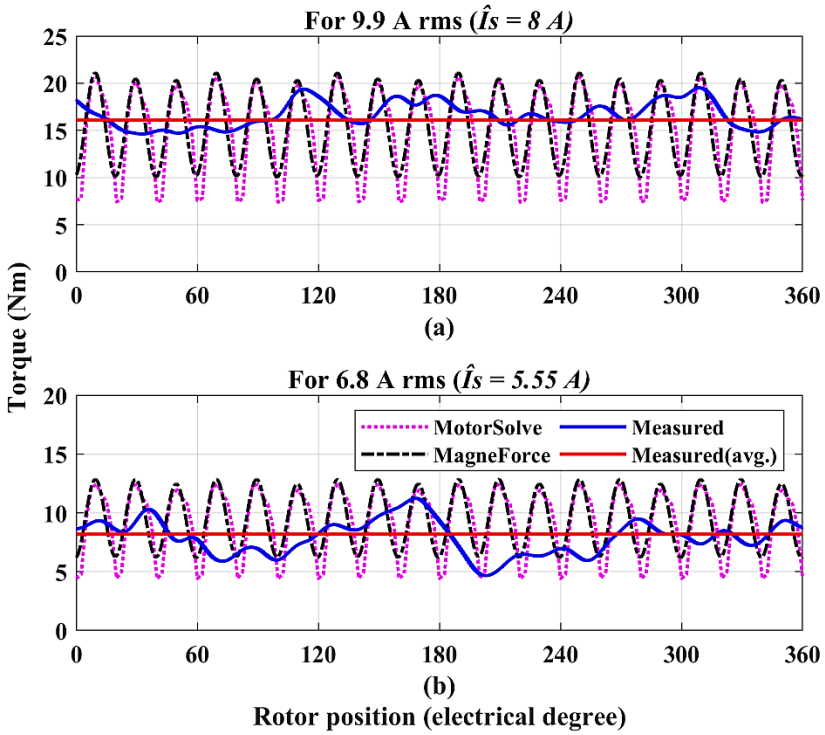

Fig. 4-25. Steady state torque for SynRM with α = 8.5°, β = 10° at 800 rpm. (a) T_L = 16 Nm at I_L = 9.9 A rms ($\hat{I}_s$ = 8 A). (b) T_L = 8 Nm at I_L = 6.8 A rms ($\hat{I}_s$ = 5.55 A).

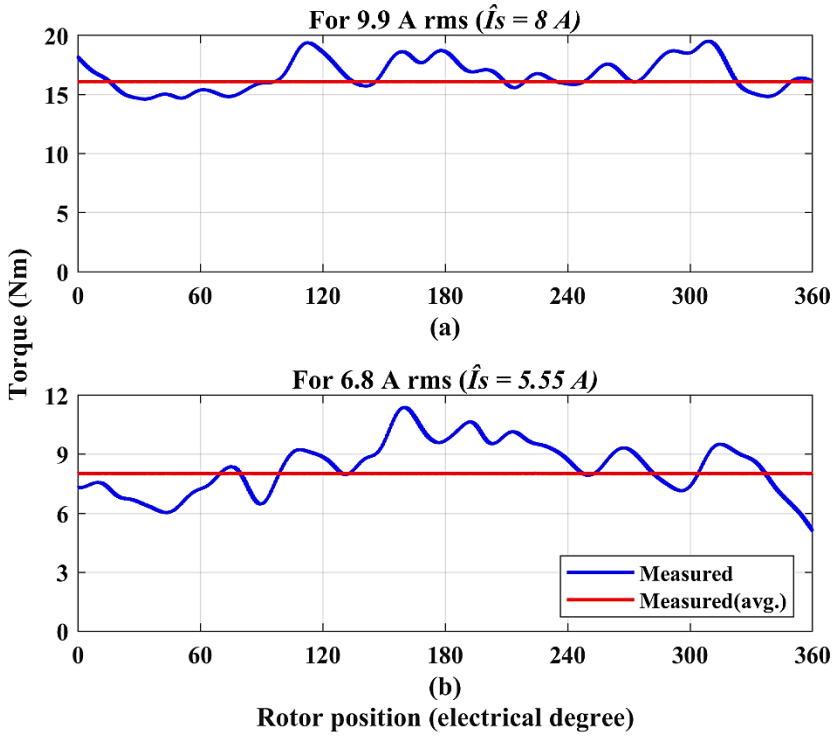

Fig. 4-26. Steady state torque for SynRM CRGO at 800 rpm. (a) T_L = 16 Nm at I_L = 9.9 A rms ($\hat{I}_s$ = 8 A). (b) T_L = 8 Nm at I_L = 6.8 A rms ($\hat{I}_s$ = 5.55 A).

Table 4-I Measured torque for 9.9 A rms ($\hat{I}s$ = 8 A) at 800 rpm

	Measured (Nm)	**MotorSolve (Nm)**	**MagneForce (Nm)**
SynRM (α = 8.5°, β = 10°)	15.98	15.45	15.72
SynRM (α = 10°, β = 10°)	16.09	15.02	15.38
SynRM CRGO	16.09	NA	NA

Table 4-II Measured torque for 6.8 A rms ($\hat{I}s$ = 5.5 A) at 800 rpm

	Measured (Nm)	**MotorSolve (Nm)**	**MagneForce (Nm)**
SynRM (α = 8.5°, β = 10°)	7.83	8.88	9.3
SynRM (α = 10°, β = 10°)	8.19	9.2	9.47
SynRM CRGO	8.02	NA	NA

4.5 Summary

In this chapter, the static torque-angle, inductance, and dynamic characterization of three SynRM designs discussed in Chapter 3 were presented. For the two CRNGO rotors, the characterizations were also carried out using three different machine design softwares, MotorSolve, MagNet, and MagneForce. However, due to the limitation of the design software, for the SynRM CRGO rotor, only experimental characterization results were presented.

The static torque-angle curves were obtained by varying both the rotor position and current angle. The torque-angle measurements were performed on the test setup shown in Fig. 4-5. The SynRM rotor with same stator and rotor slot pitches ($\alpha = \beta$ = 10°), produces a considerable pulsation in the output torque due to stator and rotor slots mutual effect as shown in Fig. 4-8(a). It was observed from Fig. 4-9(a) and Fig. 4-10(a) that, by varying the rotor slot pitch angle torque pulsation can be reduced significantly without considerable variation in the average torque and output power. Torque measurement by the varying current angle consumes less time as compared to the torque measurement by the varying rotor position. However, the torque curves generated by varying rotor positions contain both the slot and the space harmonics' effects and this is a very useful information for drives engineers to decide on the bandwidth of the controllers. Furthermore, the simulated torque curves obtained by varying the rotor position

and current angle were within the error band of the experimental results.

Inductance characterization was carried out in order to calculate the drives controller's parameters. The *d* and *q* axes inductances, as well as the saliency ratio were calculated using flux linkages obtained at different currents from the design softwares. The inductance measurements were carried out according to IEEE 1812™-2014 ac standstill test at 17 Hz supply frequency and for the phase current of 1 A rms to 14 A rms. The comparison presented a good agreement between the simulated and experimental data. Moreover, for the SynRM CRGO rotor, the lower permeability of the CRGO steel reduces *q*-axis inductance. It was validated in Fig. 4-15 that the *q*-axis inductance of the CRGO SynRM reduces significantly compared to the other two rotors. This, in turn, improved the saliency and performance of the machine.

The dynamic characterization of the prototyped SynRMs was also carried out. A special regenerative dynamometer test setup was developed in order to perform dynamic tests. The optimal current vector trajectory was investigated for MTPA control. Torque-speed curves were obtained for the prototyped rotors using MTPA control under similar operating conditions. Due to higher torque ripple, it was difficult to control the CRNGO rotor with ($\alpha = \beta = 10°$) over the wide torque-speed envelope. Among the three SynRM rotors, the SynRM CRGO possesses wider torque-speed envelope and higher torque capability for the same operating conditions. The PF and efficiency characterizations were carried out along the torque-speed envelope at the optimal current vector trajectory. The PF information can be used to decide the VA rating of the operating inverter. The SynRM CRGO rotor possesses higher power PF due to its higher saliency. The efficiency of the SynRM CRNGO ($\alpha = 8.5°$, $\beta = 10°$) and CRGO rotors are above 90% between the base and maximum speed. The maximum efficiency over the torque-speed envelope for these two rotors is 96%. In addition, steady state torque was also measured and simulated at two different torque levels. The average torque comparison presented an acceptable agreement between the simulated and measured results. Because of the limited bandwidth of the torque transducer, the torque ripple of the SynRMs could not be measured directly.

Chapter 5 Characterization of an Interior Permanent Magnet Synchronous Machine with Aligned Magnet and Reluctance Torques

In this chapter, a novel interior permanent magnet synchronous machine (PMSM) topology with aligned magnet and reluctance torques is characterized. The no-load back emf and static torque-angle are simulated and measured. The machine is simulated in the MagneForce software. Due to the asymmetric geometry of the rotor, it is not possible to model the interior PMSM in the MotorSolve software. A search coil based advance instrumentation system to monitor the machine's parameters is discussed. Moreover, the design, fabrication, and installation of the search coil in the stator of the novel interior PMSM are presented. Due to the limitations of both the MagneForce and MotorSolve, the MagNet software is used to model the search coils. These search coils are included in three different parts of the stator. The flux density waveform is obtained from the voltage induced in the search coil. This is further supported by the measurements of the prototyped interior PMSM.

5.1 Introduction

Permanent magnet synchronous machines (PMSMs) are being used extensively in numerous applications ranging from small house hold appliances to large wind turbines. These electric motors may be designed with different rotor structures, where rare earth magnets are often included to achieve high performance. Interior PMSMs have been extensively used for electric and hybrid electric tractions, such as the Chevy Volt and Nissan Leaf. Nevertheless, the rare-earth magnet price is high, and sourcing is managed by a few countries. This makes some electric vehicle (EV) manufacturers build a traction drivetrain without rare earth PMs, such as the Tesla Model S, which uses copper rotor induction motors (IMs). As an alternative to rare-earth-free or less-rare-earth traction machines, the variable-flux PM machine with AlNiCo magnets, the synchronous reluctance machine (SynRM), and the PM-assisted synchronous reluctance machine (PMa-SynRM) can be considered [11, 3].

It is discussed in Chapter 2 that AlNiCo magnets are very stable with temperature variations and can operate at a flux density comparable to rare-earth magnets. The AlNiCo based PMSM

can provide torque densities equivalent to rare-earth PMSMs. Moreover, the low coercivity of AlNiCo can be utilized in variable flux machines to achieve enhanced field weakening operation [7, 64]. Nevertheless, the variable flux machine technology is not fully established yet; in addition, an advanced control strategy is required for its control, which is still an ongoing research topic [65, 66, 67, 68]. The SynRM is PM less and it has low price construction as well as offers an acceptable flux-weakening capability. However, it has poor power factor and low torque density [3]. To overcome these issues, the SynRM is often designed with Ferrite or AlNiCo magnets or a small amount of rare-earth magnets. Nevertheless, there is a possibility of magnet demagnetization or magnetization associated in the machine with weaker or less PM during high armature reaction and flux weakening.

Accelerated research has been going on to reduce the amount of rare-earth magnets in interior PMSMs through design optimization methods [69, 70, 71]. These machines can provide high torque density and superior field weakening performance, as they can utilize both the magnet and reluctance torque components. However, in conventional interior PMSMs, these two torque components reach their maximum values at different torque angles. Hence, the machine overall torque can only utilize the reluctance and magnet torques partially. Ideally, if one of the torque components is shifted towards the other, the machine torque utilization will be improved. There have been attempts to reduce the phase shift between the magnet torque and reluctance torques. In [72], the reluctance torque in an inset PMSM is shifted towards the magnet torque, and a similar approach is used in [73] to shift the reluctance torque component in an interior PMSM. Recently, authors in [74] have proposed an innovative design of an interior PMSM, where the phase shift between the torque components is reduced without compromising the reluctance torque magnitude. The finite element analysis (FEA) of the design suggested that the magnet and reluctance torques are aligned with no compromise in the reluctance torque component. Such a machine is of high importance because of the higher torque density and capability to produce the equivalent torque to that of a conventional interior PMSM with a reduced magnet volume.

5.2 Design and Specification of an Interior Permanent Magnet Synchronous Machine with Aligned Magnet and Reluctance Torques

Based on the location of the magnet, the PMSMs are mainly classified into surface, inset,

and interior as shown in Fig. 5-1(a), (b), and (c). The average torque in the PMSM consists of the magnet and reluctance torques. The magnet torque is produced by the interaction of the fields produced by the magnets in the rotor and the stator, whereas the reluctance torque is generated by the unequal reluctances of *d* and *q* axes. The surface PMSM in Fig. 5-1(a) has a higher magnet torque due to magnet proximity to the air gap and negligible reluctance torque. Hence, the surface PMSM require higher magnet volume to produce the required torque. In the inset and interior PMSMs in Fig. 5-1(b) and (c), the *d* and *q* axes reluctances are not equal; and therefore, produce reluctance torque. Because of the reluctance torque component, a reduced quantity of magnet is required to generate the same output torque as that of a surface PMSM. The electromagnetic torque of the PMSM in the rotor reference frame can be represented as,

$$T_e = \frac{3}{2}\frac{P}{2}\left[\lambda_m I_s \sin(\delta) + \left(L_d - L_q\right) I_s^2 \sin(2\delta)\right] \tag{5-1}$$

$$T_e = T_m + T_{rel}$$

where P is the number of poles, λ_m is the magnet flux linkage, I_s is the stator current, L_d is the d-axis inductance, L_q is the q-axis inductance, δ is the current angle, T_m is the magnet torque, T_{rel} is the reluctance torque.

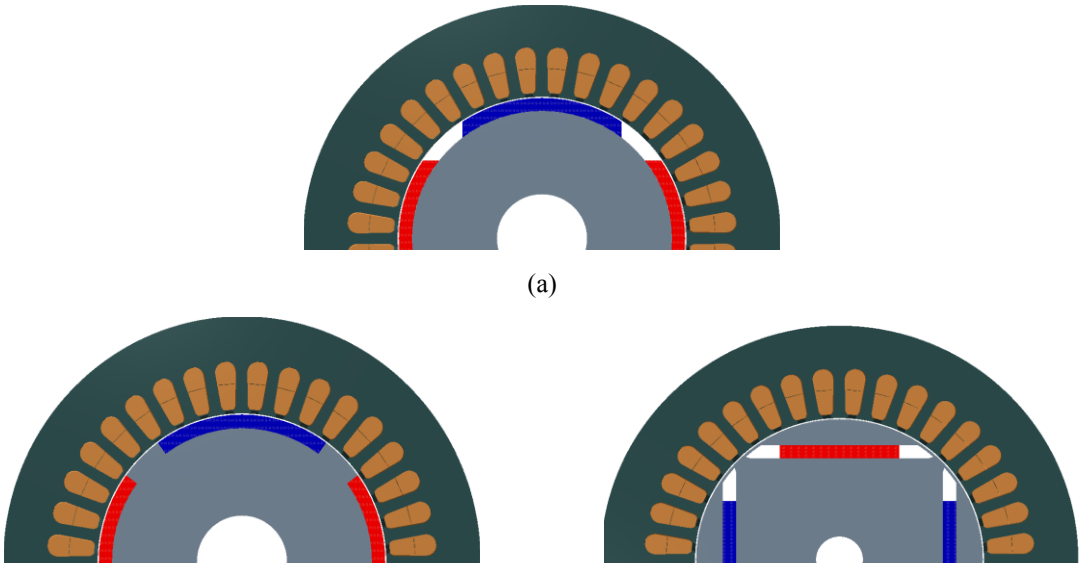

(a)

(b) (c)

Fig. 5-1. PMSM classification based on magnet location. (a) Surface PMSM. (b) Inset PMSM. (c) Interior PMSM.

Fig. 5-2 illustrates the torque components of a typical inset or interior PMSMs as a function of torque angle (δ). It is evident from Fig. 5-2 that in conventional PMSMs, the torque components T_m and T_{rel} attain their maximum values at the torque angle of 90° and 135°, respectively. Due to this phase shift, the peak magnitude of total torque is less than the algebraic sum of the individual peaks. Therefore, the total torque of the machine cannot fully utilize the magnet and reluctance torques at any operating point. In theory, if one of the torque components is moved towards the other, the machine torque utilization can be enhanced; hence, the same output torque can be produced with a reduced magnet volume. In a PMSM, a shift in a reluctance torque can be achieved simply by adding an air gap beside the magnet. In [72], the reluctance torque in an inset PMSM is shifted towards the magnet torque by adding an air-gap beside the magnet. In [73], a similar method is implemented for shifting the reluctance torque component for an interior PMSM. The analysis of the topologies presented in [72] and [73] suggested that a limited gain in the machine total torque is realized, as the additional air-gap caused a reduction in the reluctance torque magnitude. In addition, the torque ripple of the designs is relatively higher.

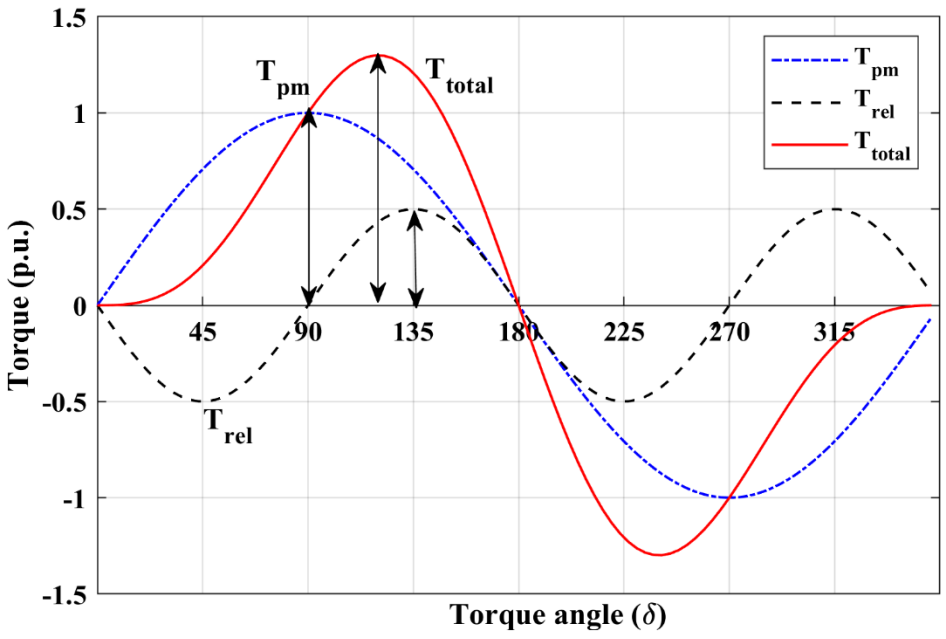

Fig. 5-2. Torque components of IPMSM.

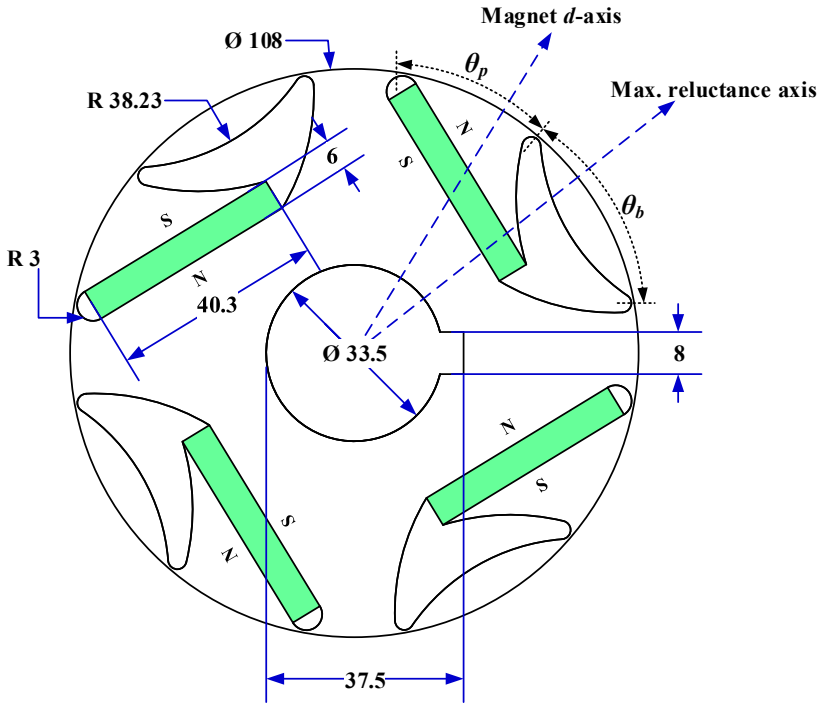

Fig. 5-3. A novel IPMSM with aligned magnet and reluctance torques.

In [74], the authors have proposed a novel design of an interior PMSM to attain a significant phase shift between the torque components, where the reluctance torque magnitude is not compromised. Fig. 5-3 shows the rotor of the proposed interior PMSM with the main dimensions. In the proposed design, the rotor contains a flux barrier similar to that of the SynRM rotor, which is introduced with an intention to guide the magnet flux away from the maximum reluctance axis. This flux barrier also guides the armature flux through the rotor steel within a barrier angle (θ_b). This results in a further shift in the reluctance axis, which leads to improve the utilization of the machine torque components. It is presented in Fig. 5-2 that the phase shift between the peak of the magnet and reluctance torques is 45°. Hence, to utilize fully both the torque components, the shift angle between the magnet and reluctance axes should be at 45°. For the proposed interior PMSM, the angle shift of 45° between the magnet and reluctance axes is obtained at θ_b = 74.4° and at the pole arc angle (θ_p) = 58.8°. The torque analysis of the prosed design is then carried out in a FEA software using the frozen permeability method. Fig. 5-4 displays the torque obtained by FEA simulation of the machine. The plot shows that the magnet and reluctance torques peak at the same torque angle. Furthermore, various FEA simulations and analysis are carried out for the back emf harmonics, torque ripple, and average output torque. A double layer lap winding design is considered,

where the coils are shorted by 1-slot. In simulations, the pole arc (θ_p) is varied between 50° and 90° to study the effect on the torque ripple and average torque. The promising value of θ_p found is 60°. In a similar manner, the flux barrier angle (θ_b) is varied between 60° and 90° to analyze its influence on the torque ripple and average torque, as the θ_b also affects the reluctance torque in addition to the shift angle. The promising value of θ_b is found to be 80°.

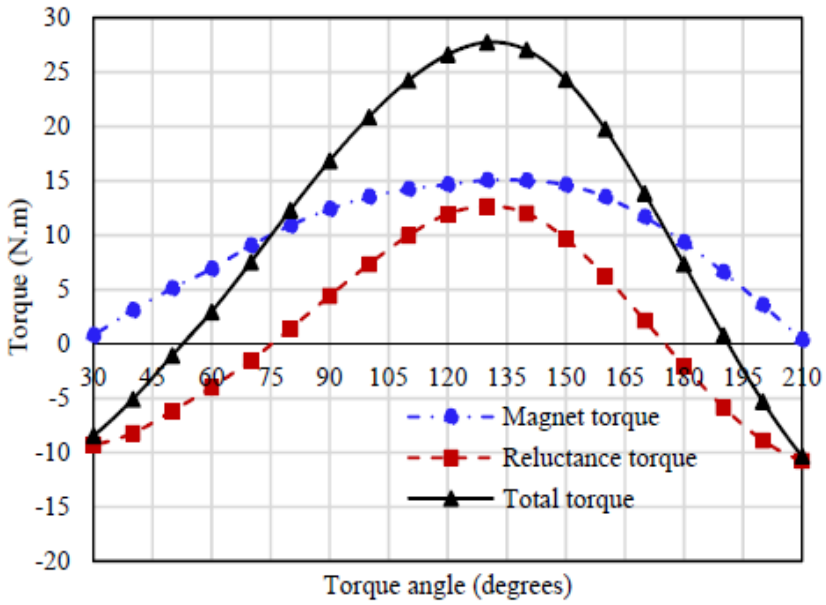

Fig. 5-4. Torque components of the proposed interior IPMSM *[72]*.

In order to validate the proposed design, a comparative analysis is carried out for the torque and magnet volume between the proposed design and three different types of PMSMs. All the machines are analyzed using the same stator. The magnet volume is altered in order to generate the total torque of 27.5 N.m. The comparison is presented in Table 5-I. It is concluded from Table 5-I that the surface PMSM in Fig. 5-1(a) uses the highest magnet volume, as the total torque of the machine is produced only by the magnet. Since the interior PMSM in Fig. 5-1(c) produces higher reluctance torque, 10.7% lower magnet volume is required compared to the inset PMSM in Fig. 5-1(b). Even though the proposed interior PMSM design has 16.9% lower magnet torque and a comparable reluctance torque to the interior PMSM, the machine is still capable of generating the same total torque with almost 19.5% lower magnet volume, as the utilization of machine's torque components has enhanced.

Table 5-I Performance Comparison of PMSMs [72].

	Surface PMSM	Inset PMSM	Interior PMSM	Proposed IPMSM
Magnet volume (mm^3)	54266	40906	36750	30225
Maximum total torque (Nm)	27.5 Nm			
Maximum magnet torque (Nm)	27.5	22	17	14.39
Maximum reluctance torque (Nm)	0	9.13	14.12	14.42

In order to validate the proposed concept, a prototype is fabricated using M36G29 CRNGO steel and SmCo magnets according to the specification listed in Table 5-II. A standard induction motor stator is used. The stator winding coil has 7 turns and is comprised of seven strands of 21 SWG copper wires. The machine is fabricated with class H insulation. The rotor laminations are fabricated using the photochemical machining (PCM) described in section 3.3.3. The rotor is assembled according to the method discussed in section 3.4.2. The rotor geometry is presented in Fig. 5-3. The prototyped rotor and its different components are depicted in Fig. 5-5.

Table 5-II Machine specification

Number of poles	4
Number of slots	36
Stator outer diameter (mm)	180
Axial length (mm)	125
Air gap length (mm)	0.5
Stator skew	1 slot (10°)
Magnet material	SmCo18
Steel material	M36 G29
DC bus voltage (V)	300
Rated current (A rms)	14
Output torque (Nm)	27
Base speed (rpm)	1350

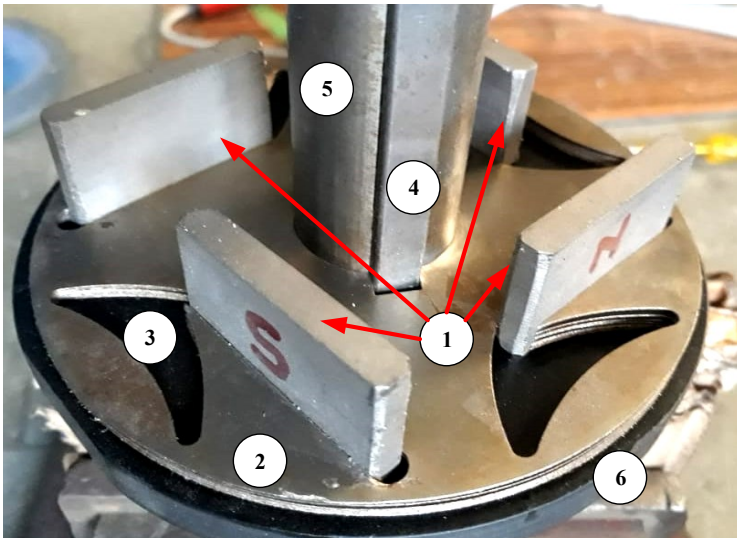

Fig. 5-5. Prototyped rotor. (1) SmCo18 magnets. (2) Rotor lamination. (3) Flux barrier. (4) Keyway. (5) Shaft. (6) Bakelite end plate.

5.3 Back emf characterization

In the prototyped interior PMSM, the SmCo magnets are inserted in a magnetized state. The back emf is then measured in order to assess the magnet flux linkage (λ_m) and back emf constant. Fig. 5-6 shows the test setup for the characterization of the prototyped interior PMSM. The test bench includes a direct current (dc) dynamometer, a torque transducer, a position encoder, a data acquisition unit, and a real-time system. The prototyped interior PMSM is coupled to the dc dynamometer through a torque transducer.

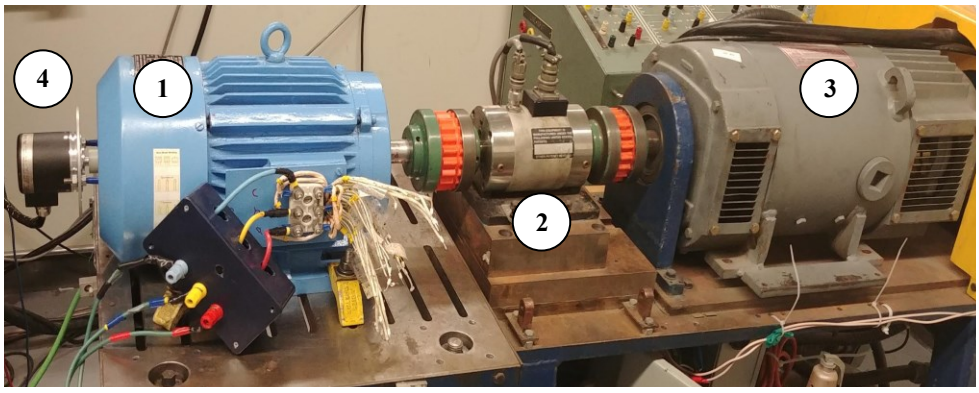

Fig. 5-6. Interior PMSM machine test setup. (1) Prototype. (2) Torque transducer. (3) dc machine. (4) Encoder.

In order to estimate the magnitude of the magnet flux linkage (λ_m), the prototyped interior PMSM is first run as a generator from 200 rpm to 2200 rpm in steps of 200 rpm. At each speed, the generated back emf is measured. Fig. 5-7 represents the back emf waveforms obtained from the design software and measurements at 1000 rpm. It can be seen from Fig. 5-7 that there is a good match between the simulation and measurement. As mentioned in the previous section, the interior PMSM is designed and simulated for the stator that is skewed by 1 slot (10° mechanical). However, the skewing of the stator is not considered during manufacturing. Therefore, the measured back emf waveform in Fig. 5-7 (black plot) of the prototyped interior PMSM has higher harmonics than the interior PMSM with the skewed stator. Fig. 5-7 also presents the simulated back emf waveform of the same interior PMSM with the skewed stator (red plot) and non-skewed stator (blue plot).

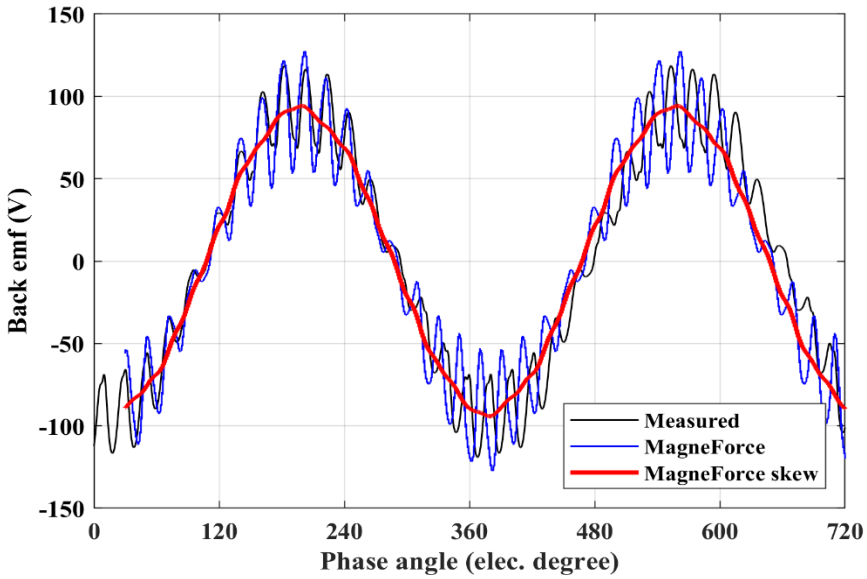

Fig. 5-7. Back emf comparison.

The peak value of the fundamental component of the back emf waveform is required to estimate the magnet flux linkage. However, the back emf waveforms of Fig. 5-7 contain harmonics. Hence, the peak value of the fundamental component of the back emf is obtained using the fast Fourier transform (FFT). Fig. 5-8 presents the FFT plot of the back emf waveform and the peak value of the fundamental component. The peak magnitude obtained from the FFT is similar to the peak value obtained from the rms value of the back emf waveform. To obtain the value of the magnet flux linkage, the peak value of the fundamental component is then divided by the electrical speed (209.44 rad/sec) of the machine. Table 5-III compares the peak

value of the fundamental component and the magnet flux linkage obtained from the measurements and MagneForce software at 1000 rpm.

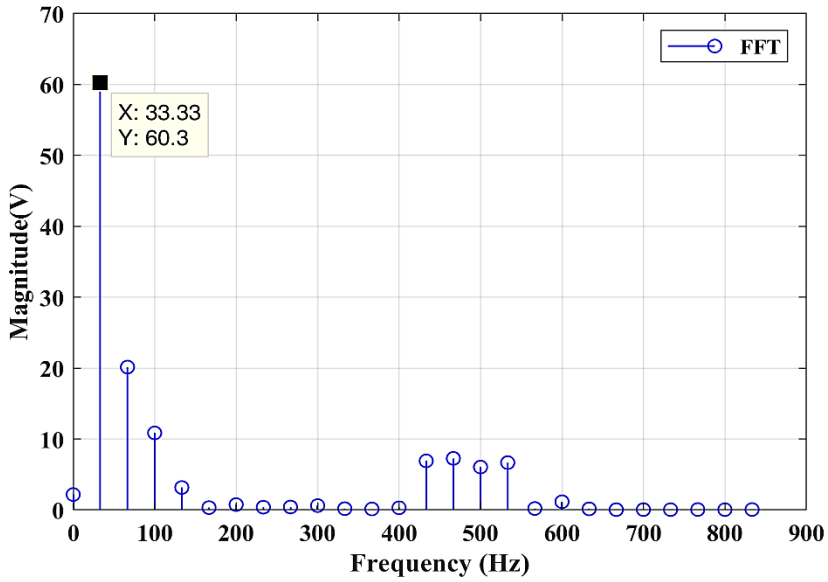

Fig. 5-8. FFT plot of measured back emf at 1000 rpm.

Table 5-III Comparisons of the fundamental peak and magnet flux linkage

MagneForce		**Measured**	
Fundamental peak (V)	**Flux linkage (V.s)**	**Fundamental peak (V)**	**Flux linkage (V.s)**
62.46	0.29	60	0.28

5.4 Static torque-angle characterization

The prototyped interior PMSM is controlled using a vector controlled inverter (VSI). Moreover, as the magnet and reluctance torques are in phase, it extremely important to locate the point of the maximum total torque for the maximum torque per ampere (MTPA) control and also to decide on the bandwidth of the controller.

Torque-angle curves are first simulated in MagneForce design software by varying the rotor position. The machine's phase A is connected to the positive of the dc current source, whereas phases B and C are connected to the negative terminal of the dc current source. The test setup shown in Fig. 5-6 is used to perform different static tests on the prototyped machine. In order to obtain the output torque at different rotor positions, initially the rotor *d*-axis is aligned with

stator phase A-axis. The rotor shaft is then locked at the *d*-axis on the test bench. The prototyped machine is wye connected. During these static measurements, phase A of the machine is connected to the positive and phases B and C are connected to the negative terminal of the dc supply. A fixed dc current is then supplied to the interior PMSM. The value of the supplied dc current is increased in steps of 2 A from 2 A to 18 A. At each current level, the resultant torque is measured from the torque transducer. The output torque for various currents is obtained at every 5° electrical (2.5° mechanical) for one electrical cycle, i.e., from 0° to 360° electrical (0° to 180° mechanical). The schematic of the interior PMSM torque-angle characterization by varying rotor position is shown in Fig. 5-9.

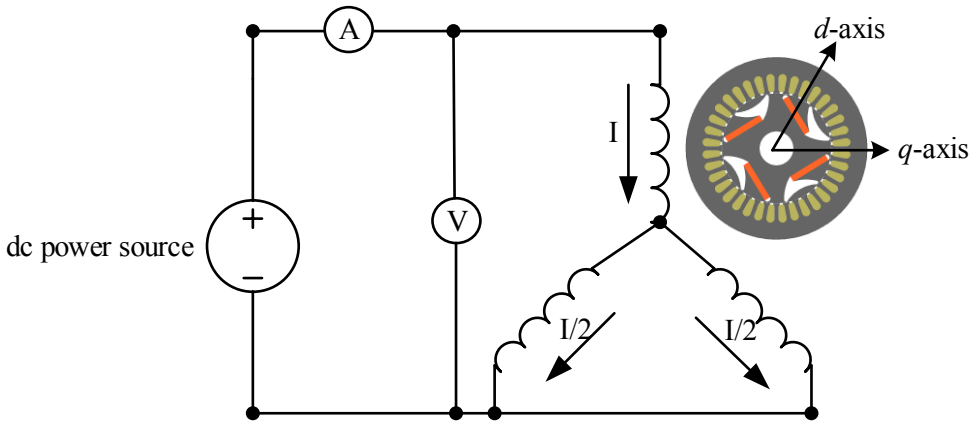

Fig. 5-9. Schematic of the interior PMSM torque-angle characterization by varying rotor position.

In Fig. 5-10, the static torque curves obtained for 18 A and 10 A are presented. Fig. 5-10(a) shows the torque curve obtained between 0° and 120° electrical. The torque curves obtained between 125° and 300° electrical are depicted in Fig. 5-10(b). It is evident from Fig. 5-10(a) that the angle at which the maximum torque occurs has shifted. The measured maximum torque for 10A occurs at 50° (25° mechanical) rotor positon. At 18 A, due to saturation, the maximum torque occurs at 70° (35° mechanical) rotor position. This proves that the magnet and reluctance torques are in phase. Moreover, in a conventional PMSM, as shown in Fig. 5-2, the torque curves are symmetrical in one electrical cycle. However, for the shifted IPMSM, it can be noticed from Fig. 5-10(b) that the torque-angle curves are not following the same trend as those in Fig. 5-10(a). This non similarity is caused as a result of the asymmetrical barrier geometry of the machine. The barriers are carved to make the magnet and reluctance torques in phase.

Hence, this interior PMSM design is most suited for applications where the rotation of the machine is unidirectional.

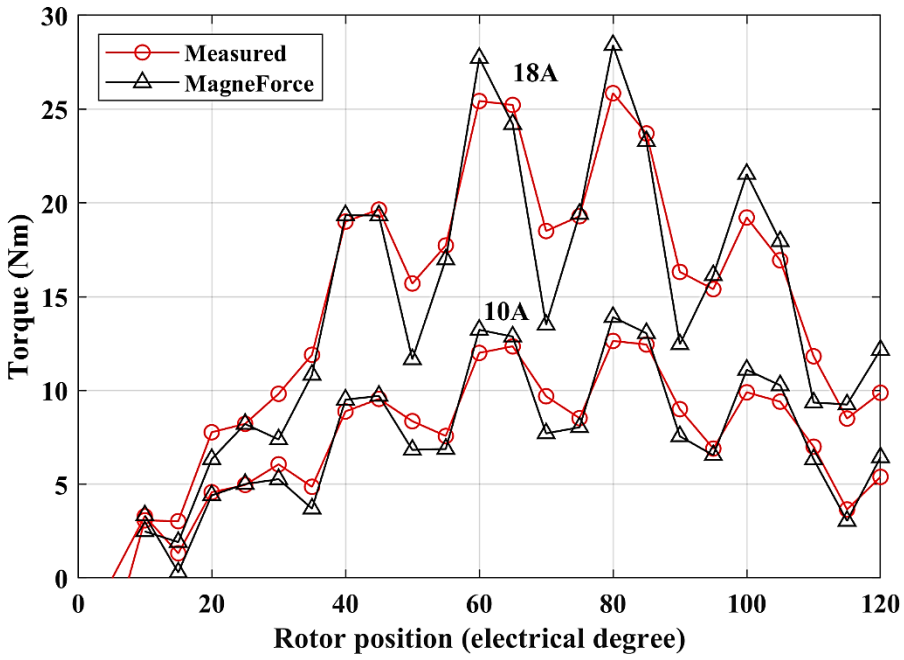

(a)

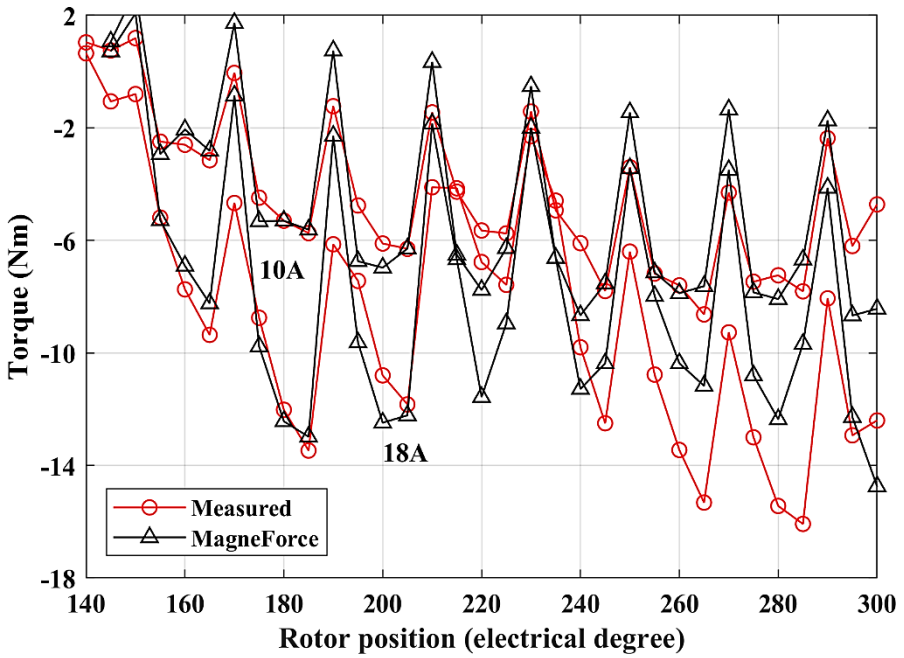

(b)

Fig. 5-10. Comparison of torque-angle curves for the shifted IPMSM. (a) Torque-angle curve for 0° to 120°. (b) Torque-angle curves for 125° to 300°.

5.5 Flux measurement by search coil

"Search coil" is the common name of a class of sensors consisting of one or more turns of conducting wire. It generates an output voltage according to Faraday's law when it is exposed to a magnetic field (B) [75]. If a coil with N turns, looped around the closed area (A), the induced voltage in the coil (V_{coil}) is given by the total rate of change of the flux ϕ as shown in (5-2). The corresponding flux density can be obtained using (5-3).

$$V_{coil} = -N\frac{d\emptyset}{dt} = -NA\frac{dB}{dt} \tag{5-2}$$

$$B = -\frac{1}{NA}\int V_{coil} \tag{5-3}$$

This method, using search coils, can be applied to the prototyped motors, in order to verify the magnetic parameters and core loss obtained by other methods such as FEA. It is also possible to integrate permanent search coils in the stator to provide real-time measurements of the machine magnetic parameters and core losses under various operating conditions. A similar method is used to analyze the magnetic parameters of the novel design of the interior PMSM. In the present work, the flux density distribution in the difference parts of the stator of an interior PMSM is investigated. In order to measure the PM flux distribution, first, the search coils are modeled and simulated in the MagNet FEA software. For the analysis of flux density variations, the search coil is placed around a stator tooth, back iron, and pole pitch. Three sets of the tooth, back iron, and pole pitch search coils are installed inside the stator. The placement of the search coils is shown in Fig. 5-11. In the MagNet software, the designed interior PMSM is simulated for different speeds and the corresponding induced voltages in the tooth, back iron, and pole pitch search coils are obtained.

For the prototyped stator, the back iron and pole pitch search coils are installed before the slot winding, as shown in Fig. 5-12(a). For the back iron search coil, a groove is created on the outer periphery of the stator stack. The tooth search coils are installed after the winding process as depicted in Fig. 5-12(b). The search coils are wound using a copper wire of 29 gauge (SWG). The wire size is selected for its suitability to be wound as a multi turn coil in a confined space

as well as for its adequate strength to avoid any breakage during the installation process. The specifications of the tooth, back iron, and pole pitch search coils are listed in Table 5-IV.

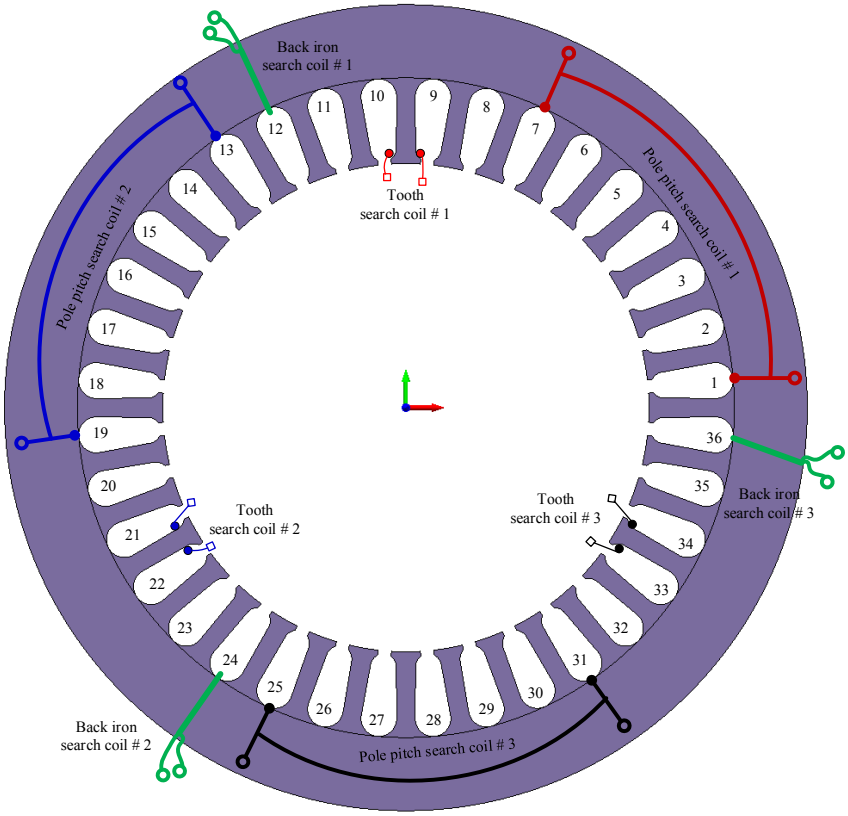

Fig. 5-11. Placement of search coils in the stator.

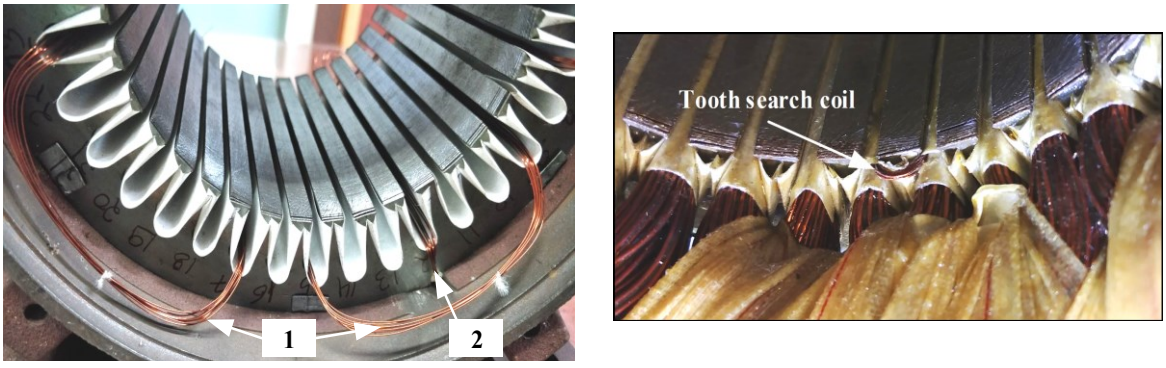

(a) (b)

Fig. 5-12. Search coil installation. (a) (1) Pole pitch search coil. (2) Back iron search coil. (b) Tooth search coil.

Table 5-IV Specifications of the "Search Coils"

Search coil wire gauge	29 SWG (0.345 mm)	
Number of turns	Tooth search coil	5
	Back iron search coil	8
	Pole pitch search coil	8
Tooth width (mm)	6.5 mm	
Back iron length (mm)	16.343 mm	
Tooth area (mm^2)	583.13	
Back iron area (mm^2)	2042.88	

In order to analyze the flux density distribution in the different parts of the stator, first the prototyped interior PMSM is run as a generator using a dc dynamotor as on the test setup as shown in Fig. 5-6. The prototyped interior PMSM is run from 200 rpm to 2200 rpm in steps of 200 rpm. At each speed, the generated voltage in the tooth, back iron, and pole pitch search coils are recorded. A YOKOGAWA SL1000 high speed data acquisition system is used for the data recording. A sampling time of $5\mu s$ is used during the measurements. The search coil voltage waveforms obtained from the simulation and measurement are then integrated into the MATLAB-Simulink to obtain the flux and flux density waveforms. A comparative analysis is then carried out between the results obtained from the simulation and measurement at 1800 rpm (60 Hz). The analysis is presented for the tooth, back iron, and pole pitch search coils. For the tooth search coil, the simulation and measurement results of the induced voltage and flux density waveforms are presented in Fig. 5-13 and Fig. 5-14, respectively. For the back iron search coil, the simulated and measured results are shown in Fig. 5-15 and Fig. 5-16, respectively. For the pole pitch search coil, the simulated and measured results are illustrated in Fig. 5-17 and Fig. 5-18, respectively. The voltage and flux density waveforms obtained from the simulation in Fig. 5-13, Fig. 5-15, and Fig. 5-17 and the corresponding voltage and flux density waveforms obtained from the measurement in Fig. 5-14, Fig. 5-16, and Fig. 5-18, present an acceptable match.

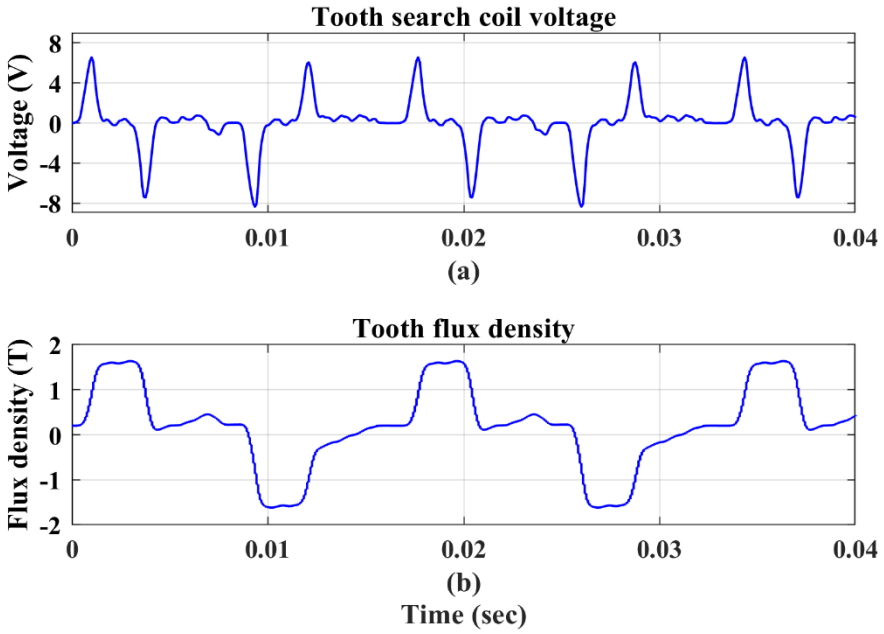

Fig. 5-13. Tooth search coil simulation. (a) Coil voltage at 1800 rpm. (b) Flux density.

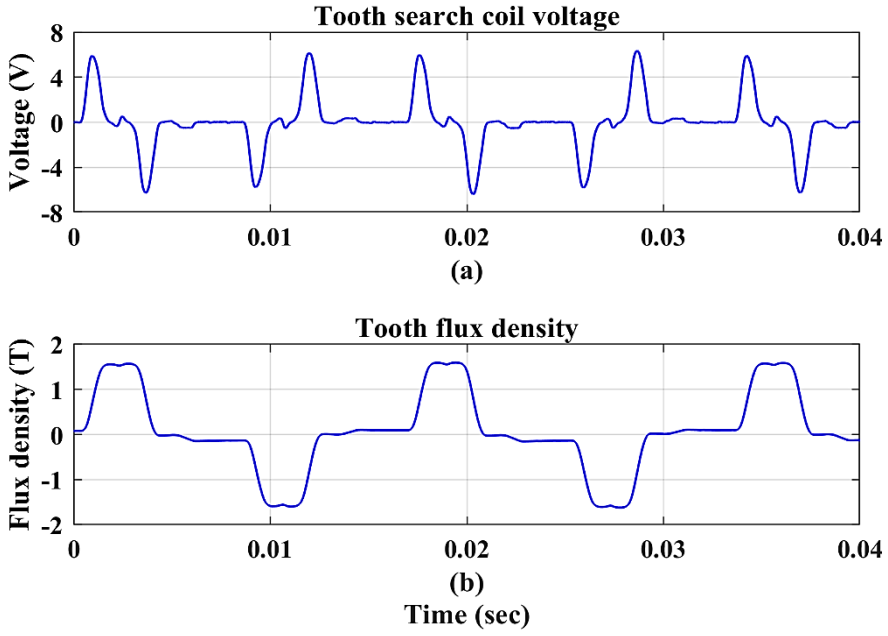

Fig. 5-14. Tooth search coil measurement. (a) Coil voltage at 1800 rpm. (b) Flux density.

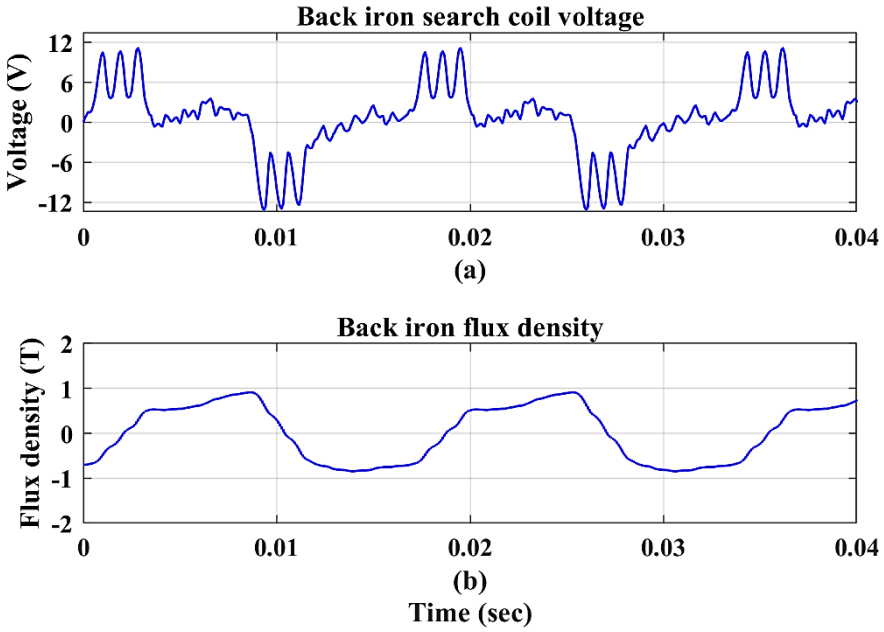

Fig. 5-15. Back iron search coil simulation. (a) Coil voltage at 1800 rpm. (b) Flux density.

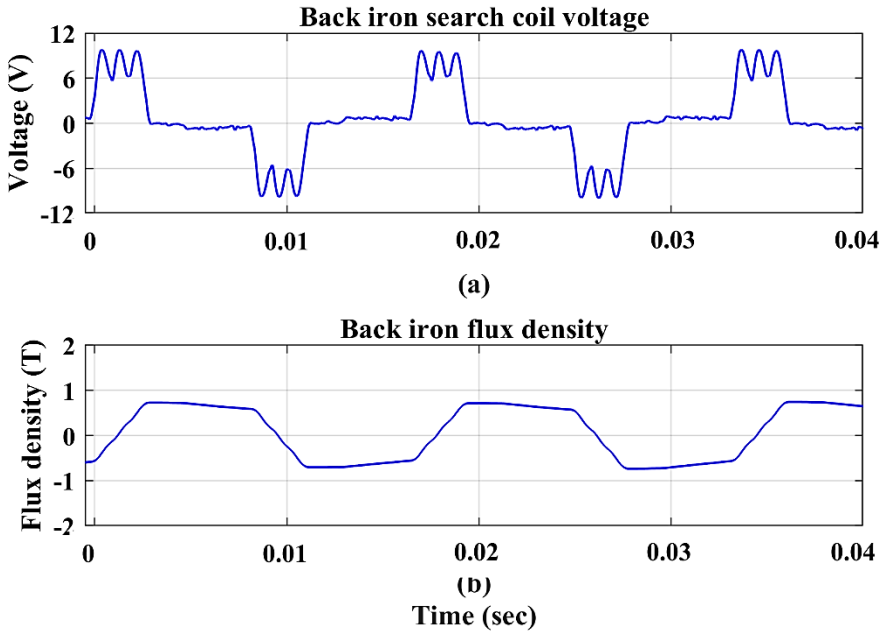

Fig. 5-16. Back iron search coil measurement. (a) Coil voltage at 1800 rpm. (b) Flux density.

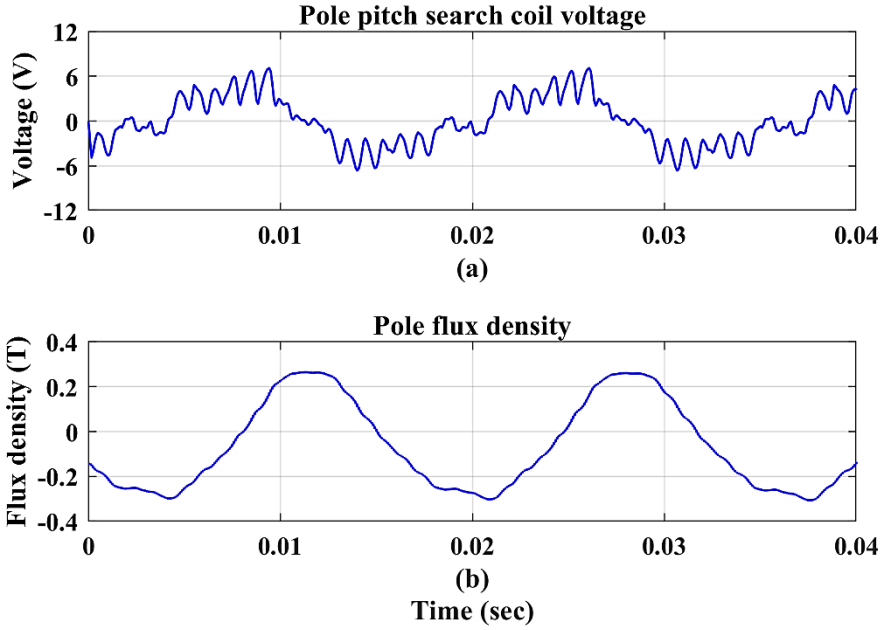

Fig. 5-17. Pole pitch search coil simulation. (a) Coil voltage at 1800 rpm. (b) Flux density.

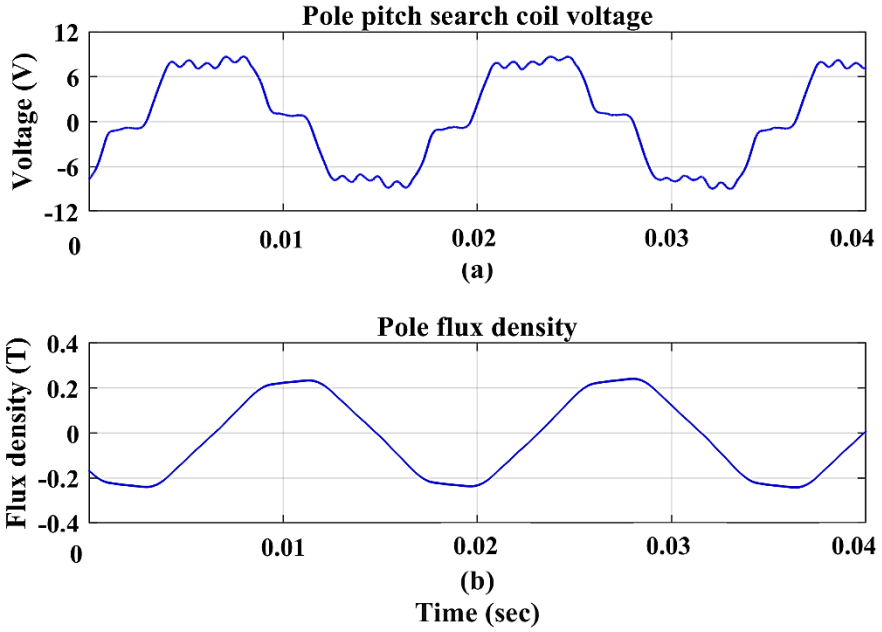

Fig. 5-18. Pole pitch search coil measurement. (a) Coil voltage at 1800 rpm. (b) Flux density.

5.6 Summary

In this chapter, the characterization of a new interior PMSM topology proposed in [74] was performed. The machine was designed in such a way that the magnet and reluctance torques are aligned. A flux barrier was carved on the rotor lamination to guide the magnet flux away from the maximum reluctance axis. By varying the barrier angle (θ_b) and pole arc angle (θ_p), the angle shift of 45° was achieved between the magnet and maximum reluctance axes. In order to validate the proposed design, a comparative analysis was performed between the proposed interior PMSM and three different types of PMSMs. The analysis confirmed that the proposed interior PMSM design is capable of producing the same total torque as that of a traditional IPMSM with almost 19.5% lower magnet volume. This also proved that the utilization of the machine's torque components has enhanced. A 5 hp prototyped was manufactured to validate the design. The PCM process and the rotor assembly method described in Chapter 3 was used to produce laminations and assemble the rotor.

The no-load back emf and torque-angle characterizations were carried out for the prototyped machine. The machine was not skewed during the fabrication. Hence, to estimate the magnitude of the magnet flux linkage, the peak value of the fundamental component was obtained from the FFT and rms value of the back emf waveform. The peak value of the fundamental component was divided by the electrical speed of the machine to obtain the value of the magnet flux linkage. In Fig. 5-7 and Table 5-III, the comparison of the back emf and magnet flux linkage was presented. The comparison illustrated an acceptable correlation between simulation and measurement.

The torque curves were obtained by the rotor position. The measurements were carried out on the test setup shown in Fig. 5-6 and the simulated torque curves were obtained in MagneForce software. The torque-angle comparison presented an acceptable correlation between the measured and simulated results. Moreover, it was also confirmed that the angle of the maximum torque has shifted, which proved that the magnet and reluctance torques were in phase. It is important to note here that the torque-angles curves were not symmetrical. This non similarity was caused as a result of the asymmetrical barrier geometry of the machine. Hence, the new interior PMSM design is most suited for applications where the rotation of the machine is mostly unidirectional. This could be considered as a limitation of the proposed machine.

The flux density measurement using the search coil was discussed. The design, fabrication, and installation of the search coil in the stator of the novel interior PMSM were presented. The search coil was first modeled in the MagNet software. Three sets of tooth, back iron, and pole pitch search coils were installed in the stator of the prototyped interior PMSM. The flux density waveform in the different parts of the prototyped stator was obtained by integrating the voltage induced in the search coil. The simulations results were further supported by the measurements.

Chapter 6 Conclusion and Recommendations for Future Work

6.1 Conclusion

In this thesis, characterization of a variable-flux PM machine, three SynRMs, and a novel interior PMSM with improved torque utilization was carried out. In order to validate the design methodologies, the accuracy of FEA software, machine models, as well as the manufacturing and assembly processes, a comparative analysis was performed between the data obtained from the measurements and simulations.

The conclusion of this thesis is summarized as follows:

6.1.1 Chapter 2

In this chapter, the no-load back emf, magnet flux linkage, static torque-angle curves, and no-load core losses were characterized for a 7.5 hp a variable-flux PM machine with AlNiCo magnets, for three different magnetization levels. The designed variable-flux machine was simulated in three different machine design softwares. A comparative analysis of the results obtained from FEA software and experimental characterizations was performed to validate the accuracy of the design, modeling, FEA software, and testing.

The no-load back emf measurement and the magnet flux linkage estimation is necessary for the magnetization state control and braking of the variable-flux PM machine. The static torque-angle characterization gives the magnitude of peak torque, torque variations over the rotor position, and the current angles for maximum torque per ampere (MTPA) control. Moreover, it also provides information about the safe operating regions of the machine where the AlNiCo magnets do not demagnetize or magnetize by the stator currents. This information is very helpful for drives engineers during the development of the control algorithms. Core loss estimation at various operating conditions gives a better efficiency estimate. Moreover, the analytical model serves as an additional tool along with the FEA for core loss estimation; through which, the machine designers can enhance their design for better performance of the machine.

6.1.2 Chapter 3

In this chapter, the fabrication and assembly processes of three different SynRM machines were presented. To validate the sizing methodology and the method to reduce torque ripple in TLA SynRM rotors, one stator and two designs of TLA CRNGO rotors with different rotor slot pitch (α) were manufactured. Moreover, in order to improve SynRM performance in terms of higher saliency, efficiency, and torque density; a novel TLA segmented CRGO rotor geometry was investigated and prototyped. Benefits and challenges of four different lamination cutting methods were presented. The application of nontraditional PCM process to develop SynRM motor laminations was described. In addition, stator and rotor assembly processes, rotor balancing procedure, as well as specific components utilized in fabrication were presented. The tolerance of ±0.015 mm (15μ) was maintained during the entire manufacturing and assembly of various components of the machine. This work presented a cost-effective way of machine fabrication. This process is an alternative way of a rapid machine prototyping with a potential for mass production.

6.1.3 Chapter 4

In this chapter, the static torque-angle, inductance, and dynamic characterization of the three SynRM designs discussed in Chapter 3 were presented. For the two CRNGO rotors, the characterizations were also carried out in three different machine design softwares. However, due to the limitation of the design software, for the SynRM CRGO rotor, only experimental characterization results were presented. A special regenerative dynamometer test setup was developed in order to perform dynamic tests. For the prototyped SynRMs, the torque-speed envelope, power factor, efficiency, and steady state torque were measured using the developed test setup.

The static torque-angle characterization provides the magnitude of peak torque, torque pulsation, and current angles for MTPA control. The inductance characterization provides the variation of inductances at different load conditions. This information benefits a drive's designer to decide on the drive controller parameters to perform an accurate dynamic characterization. The PF information is very useful to decide on the VA rating of the operating inverter. The application of the CRGO steel in the rotor lamination of SynRM can significantly improve the machine's performance. Moreover, the developed test setup equipped with a real-

time supervisory controller, measurement, and monitoring apparatus, which facilitates static and dynamic testing of different types of electric machines, real-time parameter measurement, and control.

6.1.4 Chapter 5

In this chapter, the characterization of a new interior PMSM design was performed. Moreover, the flux density in the different parts of the machine was obtained by using search coils. In the novel design of the machine, the magnet and reluctance torque components were shifted for their better utilization. A reduced amount of magnet was required to generate the rated torque as compared to the conventional PMSMs. The no-load back emf and torque-angle characterizations were performed, and the results showed a good agreement between the measurement and simulation. It was confirmed from the torque-angle curves that the peak of the total torque was shifted due to the alignment of the magnet and reluctance torques. Such a machine is of high interest due to its high torque density. The tooth, back iron, and pole pitch search coils were integrated into the stator to analyze the flux density variations. The flux density waveforms obtained from the simulation and measurements present a good match.

6.2 Future work

- For the variable-flux PM, the simulations were carried out with the static magnetization curves, which do not reflect the actual dynamic operation of the magnets. Hence, at reduced magnetization levels, it was not possible to predict the possibility of magnet magnetization at different loading conditions. It would be beneficial if the commercial FEA software could incorporate the dynamic nonlinear hysteresis loops of the AlNiCo magnets. Moreover, the dynamic characterization such as the operating envelopes, torque-speed curves, and efficiency maps of the prototyped variable-flux PM machine can be carried out on the regenerative dynamometer set up at full power.
- The static torque-angle characterization requires frequent locking of the motor shaft at different rotor positions. At present, a mechanical clamp is being used to lock the shaft during static measurements. Hence, the static measurements take a prolonged time to complete. It is also difficult to maintain the accuracy of the rotor position at a high torque level; as a result, the accuracy of the measurements is affected. In order to maintain a

precise rotor position during static measurements, a position encoder can be installed on the developed regenerative dynamometer setup. A position control algorithm and an automated process can then be developed to perform various static tests. This can lead to a reduced error as compared to using a mechanical clamp.

- The comparative analysis of the SynRMs' experimental results showed that the segmented pole SynRM CRGO rotor has a better performance compared to other rotors. However, due to the limitation of the FEA design software, it was not possible to solve the segmented pole SynRM rotor geometry with CRGO material. If FEA software can solve the SynRM or any other rotor geometries with the CRGO isotropic material, it can lead to a new direction for the design and development of high performance machines.
- In the novel design of the interior PMSM, the machine does not have a symmetrical geometry with respect to the *q*- axis. This will lead to a torque ripple in the machine. Thus, the parameters and torque ripple of the machine should be examined. Moreover, due to asymmetrical torque curves, a further investigation is required on the performance of the machine in both forward and reverse directions in order to check the accelerating and braking torque capability of the machine.
- The search coil measurement results can be further used for the core loss estimation of the prototyped interior PMSM. Moreover, real-time core loss estimation can be performed using search coils, which can improve the efficiency of the machine and control inverter.

REFERENCES

[1] C. Chen, "The State of the Art of Electric,Hybrid, and Fuel Cell Vehicles," *Proceedings of the IEEE,* vol. 95, no. 4, pp. 704-718, April 2007.

[2] I. Husain, Electric and Hybrid Vehicles: Design Fundamentals, 2nd Edition, Boca Raton: CRC Press, Aug. 2010.

[3] G. Pellegrino, T. Jahns, N. Bianchi, W. Soong, and F. Cupertino, The Rediscovery of Synchronous Reluctance and Ferrite Permanent Magnet Motors, Springer, 2006.

[4] A. Vagati, B. Boazzo, P. Guglielmi, and G. Pellegrino, "Design of ferrite-assisted synchronous reluctance machines robust toward demagnetization," *IEEE Transactions on Industry Applications,* vol. 50, no. 3, pp. 1768-1779, May-June 2014.

[5] M. Barcaro and N. Bianchi, "Interior PM machines using ferrite to substitute rare-earth surface PM machines," *International Conference on Electrical Machines,* pp. 1339-1345, Sept. 2012.

[6] M. Ibrahim, "Application of Magnetic Hysteresis Modelling to the Design and Analysis of Electrical Machines," Ph.D. dissertation, Dept. of Elec. & Comp. Eng., Concordia University, Montreal, 2014.

[7] V. Ostovic, "Memory motors," *IEEE Industry Applications Magazine,* vol. 9, no. 1, pp. 52-62, Jan./Feb. 2003.

[8] H. Liu, H. Lin, F. Shuhua, and X. Huang, "Investigation of influence of permanent magnet shape on field-control parameters of variable flux memory motor with FEM," in *Automation Congress Conference*, Sept. 2008.

[9] C. Yiguang, P. Wei, W. Ying, T. Renyuan, and W. Jing, "Interior composite-rotor controllable-flux PMSM - memory motor," *International Conference on Electrical Machines and Systems,* pp. 446-449, Sept. 2005.

[10] T. Kato, N. Limsuwan, C.-Y. Yu, K. Akatsu, and R. Lorenz, "Rare earth reduction using a novel variable magnetomotive force flux-intensified IPM machine," *IEEE Transactions on Industry Applications,* vol. 50, no. 3, pp. 1748-1756, May 2014.

[11] M. Ibrahim, L. Masisi, and P. Pillay, "Design of high torque density variable flux permanent magnet machine using alnico magnets," *IEEE Transactions on Industry Applications,* vol. 51, no. 6, pp. 4482-4491, Nov./Dec. 2015.

[12] A. Takbash, M. Ibrahim, and P. Pillay, "Design Optimization of a Spoke-Type Variable Flux Motor Using AlNiCo for Electrified Transportation," *IEEE Transactions on Transportation Electrification,* vol. 4, no. 2, pp. 536-547, June 2018.

[13] A. Aljehaimi and P. Pillay, "Operating envelopes of the variable-flux machine with positive reluctance torque," *IEEE Transactions on Transportation Electrification,* vol. 4, no. 3, pp. 707-719, Sept. 2018.

[14] A. Rabiei, T. Thiringer, M. Alatalo, and A. Grunditz, "Improved Maximum-Torque-Per-Ampere Algorithm Accounting for Core Saturation, Cross-Coupling Effect, and Temperature for a PMSM Intended for Vehicular Applications," *IEEE Transactions on Transportation Electrification,* vol. 2, no. 2, pp. 150-159, June 2016.

[15] G. McCoy, T. Litman, and J. D. Douglass, Energy-Efficient Electric Motor Selection Handbook, Portland, OR: Bonneville Power Administration, Jan. 1993, Rev.3.

[16] C. Shin, C. Choi, and W. Lee, "Advance Angle Calculation for Improvement of the Torque-to-Current Ratio of Brushless DC Motor Drives," *Elsevier 2nd International Conference on Advances in Energy Engineering,* vol. 14, pp. 1410-1414, 2012.

[17] Inolytica Corp., "Infolytica 2-D tutorial Brushless DC Motor: Calculating Torque vs. Advanced Angle," 2005.

[18] A. Tzune and T. Takeuchi, "Improvement of torque speed characteristic of brushless motor by automatic lead angle adjustment," *in Proc. Power Electronics and Motion Control Conference,* vol. 2, pp. 583-587, 2004.

[19] J. Hendershot and T. J. E. Miller, Design of brushless permanent magnet machines, Venice,FL,USA: Motor Design Books, Jan. 2010.

[20] R. Thike and P. Pillay, "Characterization of a Variable Flux Machine for Transportation Using a Vector-Controlled Drive," *IEEE Transactions on Transportation Electrification,* vol. 4, no. 2, pp. 494-505, June 2018.

[21] C. P. Steinmetz, "On the law of hysteresis," *Proc. IEEE,* vol. 72, no. 2, pp. 196-221, Feb. 1984.

[22] G. Bertotti, "General properties of power losses in soft ferromagnetic materials," *IEEE Transactions on Magnetics,* vol. 24, pp. 621-630, Jan. 1988.

[23] Y. Chen and P. Pillay, "An improved formula for lamination core loss calculations in machines operating with high frequency and high flu density excitation," *IEEE Industry Applications Society Annual Meeting,* pp. 759-766, Oct. 2002.

[24] D. M. Ionel, M. Popescu, M. I. McGilp, T. J. E. Miller, S. J. Dellinger, and R. J. Heideman, "Computation of Core losses in electrical machines using improved models for laminated steel," *IEEE Transactions on Industry Applications,* vol. 43, no. 6, pp. 1554-1564, Nov./Dec. 2007.

[25] D. M. Ionel, M. Popescu, S. J. Dellinger, T. J. E. Miller, R. J. Heideman, and M. I. McGilp, "Factors affecting the accurate prediction of iron losses in electrical machines," in *IEEE International Conference on Electric Machines and Drives*, San Antonio, May 2005.

[26] T. Mthombeni and P. Pillay, "Physical basis for the variation of lamination core loss coefficients as a function of frequency and flux density," *IEEE IECON,* pp. 1381-1387, Nov. 2006.

[27] A. Boglietti and A. Cavagnino, "Iron loss prediction with PWM supply: An overview of proposed methods from an engineering application point of view," *IEEE Ind. Appl. Soc. Annu. Meeting,* pp. 81-88, 2007.

[28] Y. Zhang, M.-C. Cheng, P. Pillay, and B. Helenbrook, "High order finite element model for core loss assessment in a hysteresis magnetic lamination," *Journal of Applied Physics,* vol. 106, no. 4, pp. 043911-1 - 043911-7, Aug. 2009.

[29] M. Ibrahim and P. Pillay, "Advanced testing and modeling of magnetic materials including a new method of core loss," *IEEE Trans.on Industry Applications,* vol. 48, no. 5, pp. 1507-1515, 2012.

[30] B. Cullity and C. Grahan, Introduction to Magnetic Materials, Wiley-IEEE Press, 2008.

[31] Y. Zhang, R. Guan, and P. Pillay, "General core loss models on a magnetic lamination," *IEEE Int. Elect. Mach. Drives Conf.,* pp. 1529-1534, 3-6 May 2009.

[32] R. Pry and C. Bean, "Calculation of the energy loss in magnetic sheet materials using a domain model," *Journal of Applied Physics,* vol. 29, no. 3, pp. 532-533, March 1958.

[33] "Laminations Steels: Types, properties, and specifications, CD-ROM," Electric Motor Education & Research Foundation, 2000.

[34] M. Ehsani, Y. Gao, and A. Emadi, Modern Electric, Hybrid Electric, and Fuel Cell Vehicles: Fundamentals, Theory, and Design, CRC Press , 2005.

[35] G. Pellegrino, A. Vagati, B. Boazzo, and P. Guglielmi, "Comparison of Induction and PM Synchronous Motor Drives for EV Application Including Design Examples," *IEEE Transactions on Industry Applications,* vol. 48, no. 6, pp. 2322-2332, Nov./Dec. 2012.

[36] J. K. Kostko, "Polyphase reaction synchronous motors," *Journal of American Institute of Electrical Engineers,* vol. 42, no. 11, pp. 1162-1168, Nov. 1923.

[37] M. Kamper, F. Van der Merwe, and S. Williamson, "Direct finite element design optimisation of the cageless reluctance synchronous machine," *IEEE Transactions on Energy Conversion,* vol. 11, no. 3, pp. 547-555, 1996.

[38] S. Morteza Taghavi and P. Pillay, "A Sizing Methodology of the Synchronous Reluctance Motor for Traction Applications," *IEEE Journal of Emerging and Selected Topics in Power Electronics,* vol. 2, no. 2, pp. 329-340, June 2014.

[39] A. Vagati, "The synchronous reluctance solution: a new alternative in AC drives," *IEEE Industrial Electronics, Control and Instrumentation,* pp. 1-13, 1994.

[40] ABB, "Technical Journal of ABB, ABB Review 1/11," ABB, Switzerland, 2011.

[41] A. Vagati, M. Pastorelli, G. Francheschini, and S. Petrache, "Design of Low-Torque-Ripple Synchronous Reluctance Motors," *IEEE Transactions on Industry Applications,* vol. 34, no. 4, pp. 758-765, July/Aug. 1998.

[42] N. Bianchi, S. Bolognani, D. Bon, and M. Dai Pré, "Rotor Flux-Barrier Design for Torque Ripple Reduction in Synchronous Reluctance and PM-Assisted Synchronous Reluctance Motors," *IEEE Transactions on Industry Applications,* vol. 45, no. 3, pp. 921-928, May/June 2009.

[43] N. Bianchi, S. Bolognani, D. Bon, and M. Dai Pré, "Torque Harmonic Compensation in a Synchronous Reluctance Motor," *IEEE Transactions on Energy Conversion,* vol. 4, no. 2, pp. 466-473, June 2008.

[44] X. Bomela and M. Kamper, "Effect of machine design on performance of reluctance synchronous machine," *IEEE Industry Application Conference,* pp. 515-522, 2000.

[45] S. Morteza Taghavi and P. Pillay, "Novel Grain-Oriented Lamination Rotor Core Assembly for a Synchronous Reluctance Traction Motor With a Reduced Torque Ripple Algorithm," *IEEE Transactions on Industry Applications,* vol. 52, no. 5, pp. 3729-3738, Sept./Oct. 2016.

[46] B. Radivoj, "Magnetic core of electric rotational machines made of grain-oriented sheets". Patent WO 2001005015 A2, 18 Jan. 2001.

[47] D. A. Staton, T. J. E. Miller, and S. Wood, "Maximising the Saliency Ratio of the Synchronous Reluctance Motor," *IEE Proceedings-B,* vol. 140, no. 4, pp. 249-259, July 1993.

[48] S. Lopes, B. Cassoret, J. Brundy, L. Lefebvre, and J. Vincent, "Grain Oriented Steel Assembly Characterization for the Development of High Efficiency AC Rotating Electrical Machines," *IEEE Transactions on Magnetics,* vol. 45, no. 10, pp. 4161-4164, Oct. 2009.

[49] S. Morteza Taghavi and P. Pillay, "A Mechanically Robust Rotor With Transverse Laminations for a Wide-Speed-Range Synchronous Reluctance Traction Motor," *IEEE Transactions on Industry Applications,* vol. 51, no. 6, pp. 4404-4414, Nov. /Dec. 2015.

[50] S. Morteza Taghavi, "Design of Synchronous Reluctance Machines for Automotive Applications," Ph.D. dissertation, Dept. of Elec. & Comp. Eng., Concordia University, Montreal, 2015.

[51] W. Tong, Mechanical Design of Electric Motors, CRC Press, April 2014.

[52] P. G. Gogue and J. J. Stupak, "Theory & Practice of Electromagnetic Design of DC Motors & Actuators," G2 Consulting, Bearverton, OR.

[53] A. Kedous-Lebouc, B. Cornut, J. Perrier, P. Manfe, and T. Chevalier, "Punching influence on magnetic properties of the stator teeth of an induction motor," *Elsevier Journal of Magnetism and Magnetic Materials,* Vols. 254-255, pp. 124-126, Jan. 2003.

[54] M. Emura, F. Landgraf, W. Ross, and J. Barreta, "The influence of cutting technique on the magnetic properties," *Elsevier Journal of Magnetism and Magnetic Materials,* vol. 254–255, pp. 358-360, Jan. 2003.

[55] Tech-etch, "Engineering Thin Medical Parts Through Photo Etching," Tech-etch.

[56] "http://enginuitysystems.com/," http://enginuitysystems.com/, [Online]. Available: http://enginuitysystems.com/files/assembly101.pdf.

[57] M. Arshad, T. Ryckebush, F. Magnussen, H. Lendenmann, J. Soulard, B. Eriksson, and B. Malmros, "Incorporating lamination processing and component manufacturing in electrical machine design tools," in *IEEE Industrial Society Annual Meeting Conference*, New Orleans, Sept. 2007.

[58] "what-when-how In Depth Tutorials and Information," The-Crankshaft Publishing, [Online]. Available: http://what-when-how.com/.

[59] "www.baldor.com," Baldor/ABB, [Online]. Available: https://www.baldor.com/~/media/files/brands/baldor-reliance/resources%20and%20support/backcover.ashx.

[60] "MakeItFrom.com," MakeItFrom.com, [Online]. Available: http://www.makeitfrom.com/material-properties/Polyetheretherketone-PEEK.

[61] "https://bis.gov.in/," Bureau of Indian Standards, [Online]. Available: https://archive.org/details/gov.in.is.2036.1995/page/n3.

[62] T. Lipo, T. Miller, A. Vagati, I. Boldea, L. Malesani, and T. Fukao, "Synchronous reluctance drives," *IEEE Industry Application Society Annual Meeting,* Oct. 1994.

[63] "IEEE Trial-Use Guide for Testing Permanent Magnet Machines,IEEE std 1812-2014," IEEE Power and Energy Society and IEEE Industry Application Society, New York, Jan. 2013.

[64] N. Limsuwan, T. Kato, K. Akatsu, and R. Lorenz, "Design and evaluation of a variable-flux flux-intensifying interior permanent magnet machine," *IEEE Transactions on Industry Applications,* vol. 50, no. 2, pp. 1015-1024, March-April 2014.

[65] A. Aljehaimi and P. Pillay, "Online rotor flux linkage estimation for a variable flux interior permanent magnet synchronous machine operating at different flux density levels," in *IEEE International Conference on Power Electronics, Drives and Energy Systems*, Trivandrum, India, Dec. 2017.

[66] A. Athavale, K. Sasaki, T. Kato, and R. Lorenz, "Magnetization state estimation in variable-flux PMSMs," in *IEEE International Electric Machines and Drives Conference* , Aug. 2017, May 2017.

[67] B. Gagas, K. Sasaki, T. Fukushige, A. Athavale, T. Kato, and R. Lorenz, "Analysis of magnetizing trajectories for variable flux PM synchronous machines considering voltage, high-speed capability, torque ripple, and time duration," *IEEE Transactions on Industry Applications,* vol. 52, no. 5, pp. 4029-4038, Sept.-Oct. 2016.

[68] L. Masisi, M. Ibrahim, and P. Pillay, "Control strategy of a variable flux machine using AlNiCo permanent magnets," in *IEEE Energy Conversion Congress and Exposition* , Montreal, Canada, Sept. 2015.

[69] F. Cupertino, G. Pellegrino, and C. Gerada, "Design of synchronous reluctance motors with multiobjective optimization algorithms," *IEEE Transactions on Industry Applications,* vol. 50, no. 6, pp. 3617-3627, March 2014.

[70] G. Sizov, D. Ionel, and N. Demerdash, "Modeling and parametric design of permanent-magnet AC machines using computationally efficient finite-element analysis," *IEEE Transactions on Industrial Electronics,* vol. 59, no. 6, pp. 2403-2413, June 2012.

[71] Y. Wang, D. Ionel, V. Rallabandi, M. Jiang, and S. Stretz, "Large-scale optimization of synchronous reluctance machines using CE-FEA and differential evolution," *IEEE Transactions on Industry Applications,* vol. 52, no. 6, pp. 4699-4709, Nov.-Dec. 2016.

[72] W. Zhao, T. Lipo, and B. Kwon, "Optimal design of a novel asymmetrical rotor structure to obtain torque and efficiency improvement in surface inset pm motors," *IEEE Transactions on Magnetics,* vol. 51, no. 3, pp. 1-4, March 2015.

[73] W. Zhao, F. Zhao, T. Lipo, and B. Kwon, "Optimal design of a novel V-type interior permanent magnet motor with assisted barriers for the improvement of torque characteristics," *IEEE Transactions on Magnetics,* vol. 50, no. 11, pp. 1-4, Nov. 2014.

[74] M. Ibrahim and P. Pillay, "Aligning the Reluctance and Magnet Torque in Permanent Magnet Synchronous Motors for Improved Performance," in *IEEE Energy Conversion Congress and Exposition*, Portland,USA, Sept. 2018.

[75] S. Tumansaki, "Induction coil sensors—a review," *Measurement Science and Technology,* vol. 18, pp. R31-R46, Jan. 2007.